ISSN 2587-1366

TUJE

TURKISH JOURNAL OF ENGINEERING

VOLUME 2 ISSUE 2 MAY 2018

TURKISH JOURNAL OF ENGINEERING (TUJE)

Turkish Journal of Engineering (TUJE) is a multi-disciplinary journal. The Turkish Journal of Engineering (TUJE) publishes the articles in English and is being published 3 times (January, May, September) a year. The Journal is a multidisciplinary journal and covers all fields of basic science and engineering. It is the main purpose of the Journal that to convey the latest development on the science and technology towards the related scientists and to the readers. The Journal is also involved in both experimental and theoretical studies on the subject area of basic science and engineering. Submission of an article implies that the work described has not been published previously and it is not under consideration for publication elsewhere. The copyright release form must be signed by the corresponding author on behalf of all authors. All the responsibilities for the article belongs to the authors. The publications of papers are selected through double peer reviewed to ensure originality, relevance and readability.

AIM AND SCOPE

The Journal publishes both experimental and theoretical studies which are reviewed by at least two scientists and researchers for the subject area of basic science and engineering in the fields listed below:

Aerospace Engineering
Environmental Engineering
Civil Engineering
Geomatic Engineering
Mechanical Engineering
Geology Science and Engineering
Mining Engineering
Chemical Engineering
Metallurgical and Materials Engineering
Electrical and Electronics Engineering
Mathematical Applications in Engineering
Computer Engineering
Food Engineering

PEER REVIEW PROCESS

All submissions will be scanned by iThenticate® to prevent plagiarism. Author(s) of the present study and the article about the ethical responsibilities that fit PUBLICATION ETHICS agree. Each author is responsible for the content of the article. Articles submitted for publication are priorly controlled via iThenticate ® (Professional Plagiarism Prevention) program. If articles that are controlled by iThenticate® program identified as plagiarism or self-plagiarism with more than 25% manuscript will return to the author for appropriate citation and correction. All submitted manuscripts are read by the editorial staff. To save time for authors and peer-reviewers, only those papers that seem most likely to meet our editorial criteria are sent for formal review. Reviewer selection is critical to the publication process, and we base our choice on many factors, including expertise, reputation, specific recommendations and our own previous experience of a reviewer's characteristics. For instance, we avoid using people who are slow, careless or do not provide reasoning for their views, whether harsh or lenient. All submissions will be double blind peer reviewed. All papers are expected to have original content. They should not have been previously published and it should not be under review. Prior to the sending out to referees, editors check that the paper aim and scope of the journal. The journal seeks minimum three independent referees. All submissions are subject to a double blind peer review; if two of referees gives a negative feedback on a paper, the paper is being rejected. If two of referees gives a positive feedback on a paper and one referee negative, the editor can decide whether accept or reject. All submitted papers and referee reports are archived by journal Submissions whether they are published or not are not returned. Authors who want to give up publishing their paper in TUJE after the submission have to apply to the editorial board in written. Authors are responsible from the writing quality of their papers. TUJE journal will not pay any copyright fee to authors. A signed Copyright Assignment Form has to be submitted together with the paper.

PUBLICATION ETHICS

Our publication ethics and publication malpractice statement is mainly based on the Code of Conduct and Best-Practice Guidelines for Journal Editors. Committee on Publication Ethics (COPE). (2011, March 7). Code of Conduct and Best-Practice Guidelines for Journal Editors. Retrieved from http://publicationethics.org/files/Code%20of%20Conduct_2.pdf

PUBLICATION FREQUENCY

The TUJE accepts the articles in English and is being published 3 times. January, May, September a year.

CORRESPONDENCE ADDRESS

Journal Contact: tuje@mersin.edu.tr

CONTENTS

Volume 2 – Issue 2

ARTICLES

Turkish Journal of Engineering

Turkish Journal of Engineering (TUJE)
Vol. 2, Issue 2, pp. 38-48, May 2018
ISSN 2587-1366, Turkey
DOI: 10.31127/tuje.340334
Research Article

AQUIFER THERMAL ENERGY STORAGE SYSTEMS: BASIC CONCEPTS AND GENERAL DESIGN METHODS

Nihan Aydın Ertuğrul *[1], Zübeyde Hatipoğlu Bağcı [2] and Özgür Lütfi Ertuğrul [3]

[1] Mersin University, Directorate of Construction and Technical Works, Mersin, Turkey
ORCID ID 0000 – 0002 – 2850 – 1275
(nihanertugrul@mersin.edu.tr)

[2] Mersin University, Engineering Faculty, Department of Geological Engineering, Mersin, Turkey
ORCID ID 0000 – 0002 – 7935 – 5028
(zubeyde@mersin.edu.tr)

[3] Mersin University, Engineering Faculty, Department of Civil Engineering, Mersin, Turkey
ORCID ID 0000 – 0002 – 1270 – 3649
(ozgurertugrul@hotmail.com)

* Corresponding Author
Received: 28/09/2017 Accepted: 13/10/2017

ABSTRACT
Renewable energy plays an important role in meeting the ever increasing energy demand of the modern world. At this point, underground thermal energy storage has been suggested as a clean and efficient alternative of energy extraction for the sustainable future as one of the renewable energy varieties. Thermal energy storage systems in the aquifers have preluded the energy market with great success in many countries. Hot and cold natural energy sources are stored in the aquifer by using underground water to store the heat in this system. Efficiency of the system depends on several factors including groundwater temperatures and flow characteristics. Among the different underground thermal energy storage options, one of the most promising and commercial option is known as aquifer thermal energy storage (ATES). Based on the recent developments reported in the literature, general design procedures and construction techniques as well as relationships related with the efficiency of ATES systems are reviewed within the scope of this paper. The applications from the world and Turkey were discussed in a comparative approach.

Keywords: *Aquifer Thermal Energy Storage, Groundwater Flow, Heat Transfer, Underground Thermal Energy Storage*

1. INTRODUCTION

The concept of energy and the sustainability of energy resources have been one of the most important issues coming from the past. Energy plays an important role in the economic prosperity and the technological competitiveness of a nation. In conjunction with the rapidly increasing world population and industrial production rates, overall energy demand is reaching to record high values in the current decade. One of the main problems of ever increasing energy demand is related with heavy consumption of fossil fuels which is leading to significant environmental impact. Fossil fuels, at the forefront of energy reserves consumed today, have tended to run out on one hand, and become one of the most important factors of environmental pollution on the other. Several energy conservation strategies become more feasible as fossil fuel resources such as oil, natural gas, and coal are reaching to their limits. Since global warming is also becoming one of the most critical problems in the world, more efficient and economical ways to utilize clean and renewable energies are heavily needed. The demand for the utilization is not only in the field of energy production and consumption, but also in the area of energy storage.

The search for alternative energy sources, such as solar, wind and thermal energy has been initiated and problems of climate change and global warming caused by the harmful gases released to the atmosphere due to the use of fossil fuels will seriously be reduced. Increasing attention has been paid to thermal energy storage (TES) system applications since they offer environmentally friendly solutions to afore mentioned energy problems and make it possible to more effectively utilize waste heat/cold recovery for space heating and cooling. With a storage medium of various types and sizes, TES systems contribute to improving energy efficiency to contribute for building self-sustainable cities.

Thermal energy storage at shallow soils and rocks has recently been developed as an innovative approach for keeping excess energy and use it when needed. Thermal energy storage systems in the aquifers, one of the underground storage alternatives for thermal energy applications, have penetrated the energy market with a great success in many countries including Europe, United States and Canada. Aquifer thermal energy storage (ATES) is a cost-effective technology that enables the reduction of energy use and CO_2 emissions associated with the heating and cooling of buildings by storage and recovery of large quantities of thermal energy in the subsurface. In these systems, thermal energy is stored in the aquifers by injecting heat energy into groundwater by means of injection wells. Energy storage capacity depends on several factors including, groundwater temperatures, flow characteristics and volume of the aquifer. Stored energy is extracted as a reversible process to meet heating or cooling demands of buildings when required.

ATES systems provide significant energy saving rates which ensures efficient use of other energy sources. Even more important issue is the use of local and natural resources to increase energy security while reducing environmental hazards. There is a significant reduction in the emission of greenhouse gases by means of the energy savings provided by thermal energy storage methods. This technique provides serious reductions in CO_2 emissions. Thirteen OECD countries have been conducting research and development activities of thermal energy storage techniques within the framework of the Energy Saving Implementation Agreement (IEA ECES-IA) since 1970.

There are several hundreds of aquifer thermal energy storage systems in operation, with the Netherlands and Sweden as dominating countries of implementation. Particularly the Netherlands is the world leader in terms of utilization of this method. Thermal energy storage systems using groundwater have become a standard technique in public buildings and facilities in the Netherlands. The number of ATES system in the Netherlands in the utility sector is depicted in Figure 1 (Sommer *et al.*, 2014).

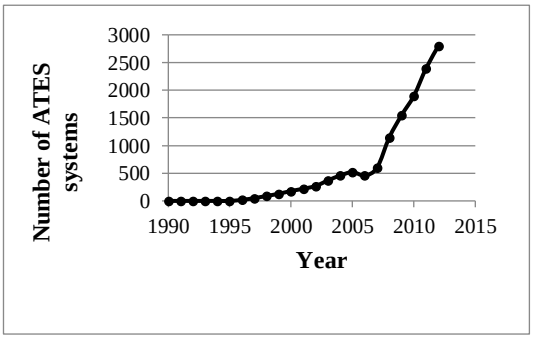

Fig. 1. The number of ATES systems in the utility sector of the Netherlands (Sommer *et al.*, 2014)

As one of the leading countries utilizing ATES systems, Germany's long-term goal is to reduce the use of fossil fuels by 50% by the year of 2050. There are currently eight large-scale, residential buildings built using solar energy supported TES systems in Germany. The German Federal Parliament Building Reichstag is heated and cooled by the storage of waste heat energy from the building within the aquifer. In addition, Canada has the world's largest underground heat pump application. The system located at the University of Ontario Institute of Technology contains 370 wells reaching at a depth of 200 meters.

Based on the field applications and design techniques reported in the current literature, this study presents an up-to-date review of underground thermal energy storage methods while aiming to introduce general design procedures and construction techniques related with aquifer thermal energy storage applications.

2. THERMAL ENERGY STORAGE CONCEPT

Thermal energy is a form of energy that is the sum of the potential and kinetic energies of a substance in the environment or in a specific system. Thermal energy storage (TES) refers to the technology that allows the storage and transfer of energy in terms of heat. The basic idea behind thermal storage is to provide a buffer to balance fluctuations in supply and demand of energy (Nielsen, 2003) and to compensate the time difference between periods of energy input and those of power demand. Thermal energy storage systems generally involve a temporary buffer storage of high- or low-

temperature thermal energy for later use. According to Rosen *et al.* (2003), utilization of thermal energy storage systems often provides significant benefits as the following which is outlined as follows:

• reduced energy costs and consumption;
• improved indoor air quality;
• increased flexibility of operation;
• decreased initial and maintenance costs;
• reduced equipment size;
• more efficient and effective utilization of equipment;
• conservation of fossil fuels (by facilitating more efficient energy use);
• reduced pollutant gas emissions.

There are various thermal energy storage systems, storing the energy as sensible heat. These systems include designed containers, underground aquifers, shallow soils and rocks as well as surface waters such as ponds and lakes. Alternatively, thermal energy can be stored in the latent heat of melting in such materials as salts or paraffin based chemicals. TES technologies can be categorized according to criteria based on different chemicals given in Table 1 (Cao, 2010). If the criterion is based on the temperature level, the thermal storage solutions can be divided into ''heat and cold storage''. If based on the time length of stored thermal heat, it can be divided into ''short and long term''. If based on the state of energy storage material, it can be divided into ''sensible, latent and thermochemical heat storage''.

Table 1. Classification of thermal energy storage solutions (Cao, 2010).

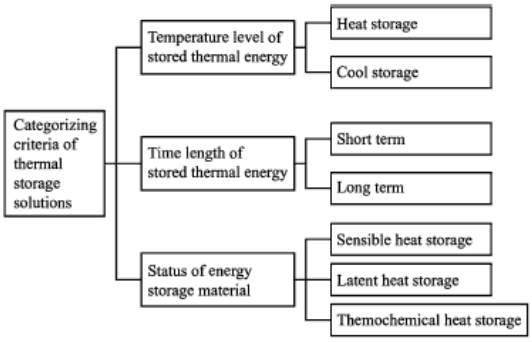

2.1. Underground Thermal Energy Storage (UTES)

The shallow subsurface is increasingly being used as a storage medium for thermal energy, generally referred to as underground thermal energy storage. Shallow soil and rock provides buffer storage systems between the seasons since thermal energy is passively stored into the soil and groundwater by the seasonal climate changes. Average temperature of the ground is higher than that of surface air temperature during the winter and lower during the summer. As a result, the ground and groundwater are suitable media or source for heat extraction during the winter and cold extraction during the summer. The low thermal diffusivity of the Earth's subsurface relative to river and air at Elverum, Norway is shown in Figure 2 (Banks., 2012). Measurement results indicate that the groundwater temperature remains relatively constant throughout the year starting from 10 meters below ground surface while increasing very slowly due to the geothermal gradient coming from earth core (Sanner *et al.*, 2003). Temperature profile of the geological units within a certain depth indicating the seasonal zone of fluctuation in temperature and the nearly constant temperature zone is given in Figure 3 (Florides and Kalogirou, 2007). This figure illustrates the actual ground temperatures as measured in a borehole drilled in Nicosia, Cyprus. The temperature rises from 1°C to 3°C as the depth increases due to the heat flux (Banks, 2012) which is shown in Figure 4.

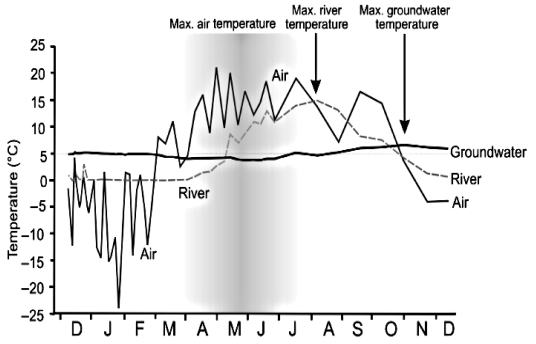

Fig. 2. Fluctuation of temperature of the air, the river and shallow groundwater, at Elverum, Norway (Banks, 2012).

Since the ambient climatic conditions affect the temperature profile below the ground surface, it needs to be considered when designing a thermal energy storage system. The Earth's average annual surface temperature is determined by the balance between solar radiation energy since the Earth's surface acts as a huge solar collector, geothermal heat flux derived from the Earth's interior and the variables of these factors which is illustrated in Figure 5 (Florides and Kalogirou, 2007) and accepted to be approximately 14°C. The temperature of the shallow subsurface is affected by the physical properties of the ground, as well as the climate interaction determined by air temperature, wind, solar radiation, air humidity and rainfall.

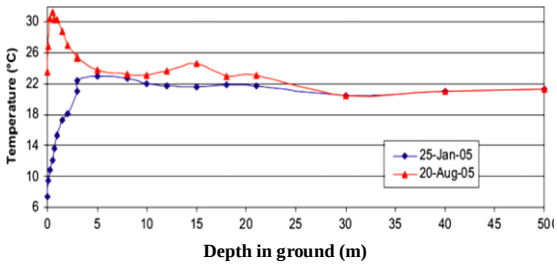

Fig. 3. Zone of fluctuation in temperature due to the seasonal changes (Florides and Kalogirou, 2007).

2.1.1. Basic concepts and applications

Underground storage for thermal energy is mostly used for heat storage on a seasonal basis. In winter period, while heating demand is high, heat can be extracted from underground energy storage, whereas in summer term,

while cooling is needed, a reverse process can be facilitated which can also mean storage of additional heat in the subsurface storage. There is not any standard design procedure for conventional UTES installations. Each facility is unique even though the basic principles are similar and components like fluid circulation pumps, pipes and heat exchangers etc. are industrial products. To choose the right system for a specific installation, several factors such as geological and hydrogeological conditions, area and utilization on the surface, existence of potential heat sources like mines, and the heating and cooling characteristics of the infrastructures have to be considered. In the design phase, more accurate data of the key parameters are necessary for the chosen technology so as to achieve the optimum performance with minimum cost. There are several concepts regarding the underground medium thermal energy storage alternatives (Novo *et al.*, 2010). The main concepts can be listed as;

- Aquifer thermal energy storage (ATES),
- Borehole thermal energy storage (BTES),
- Cavern thermal energy storage (CTES)
- Ducts in soil
- Pit storage

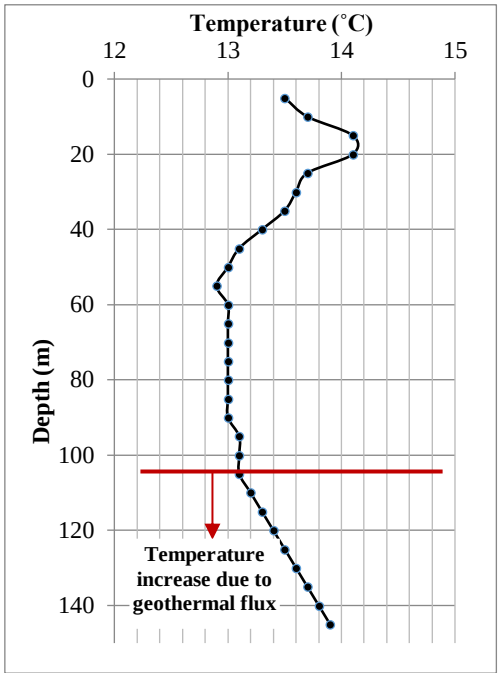

Fig. 4. Downward increase in temperature beginning approximately from 100 m depth depending upon geothermal heat flux (Banks, 2012)

Aquifer Thermal Energy Storage (ATES) uses natural ground water in a saturated and permeable subsoil layer as the storage medium. Thermal energy is transferred by extracting groundwater from the aquifer and by re-injecting it at an altered temperature to a separate well nearby.

Borehole thermal energy storage (BTES) applications are operated in closed loop heat exchanger systems in which there is no contact between the natural groundwater and the heat exchange fluid. This system includes one or more boreholes equipped with borehole heat exchangers through which waste heat or cold energy is circulated and transferred to underground for storage.

Cavern Thermal Energy Storage (CTES) utilize large groundwater reservoirs existing in the subsoil to serve as a thermal energy storage system. These storage technologies are technically feasible, but the actual application is still limited due to the relatively high initial investment cost.

The duct type storage in soils is best suited for circulating fluids with low temperature around 25-30˚C, and needs heat pump supported systems to raise the temperature of the space heating and tap water to a suitable level. This type of storage has found extensive use in connection with ground coupled heat pumps (GCHP) where the duct can be placed in horizontal relatively shallow trenches, or in vertical boreholes. (Nielsen, 2003)

Pit storage systems are artificial structures, also called man-made aquifers, built below ground like buried tanks or close to the surface to reduce high investment cost. These systems seem to be a viable option when environmental restrictions about natural ground water are involved.

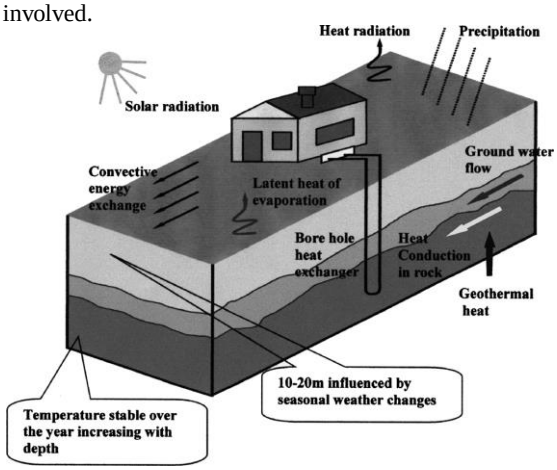

Fig. 5. Thermal energy flow diagram in the ground (Florides and Kalogirou, 2007).

Considering the well documented field applications in the world, heat storage in aquifers may be achieved by open systems such as ATES and closed loop heat exchange systems such as BTES systems (Furbo, 2014). Basic working principal scheme of aquifer and borehole thermal energy storage systems is depicted in Figure 6. These concepts have already been introduced as commercial systems on the energy market in several countries. Thermo-hydraulic and hydrogeological criteria for the optimum thermal energy storage technique choice are shown in Figure 7 by Sanner (2001).

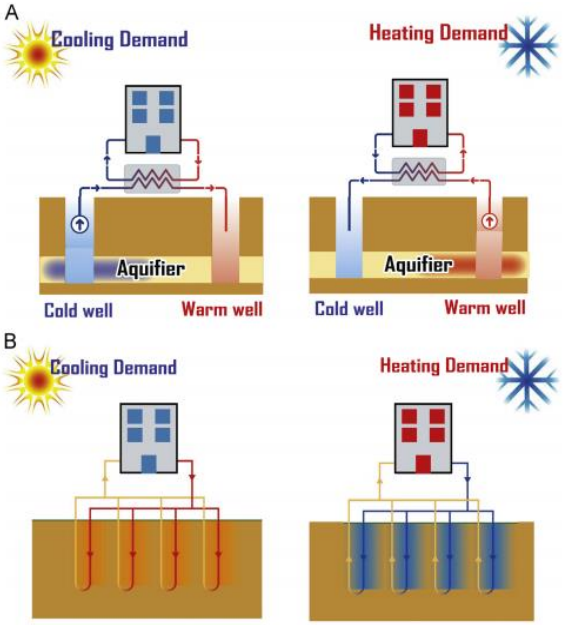

Fig. 6. Principle schemes of (a) aquifer and (b) borehole thermal energy storage systems (Bloemendal *et al*., 2014).

In aquifer thermal energy storage systems, groundwater is utilized as heat carrier whereas in closed loop borehole thermal energy storage applications, heat carrier fluid is cycled in boreholes independent from the groundwater occurrence and are operated in closed loop as explained in Figure 7. Porosity of the subsurface formation is another significant factor for the selection of the most suitable thermal energy storage system.

Aquifer thermal energy storage technique is particularly suitable among the different system types to store large amounts of thermal energy (Sommer *et al*., 2014). The system has developed into a cost-effective technology for heating and cooling of utility buildings such as offices, hospitals, universities and greenhouses, and to reduce greenhouse gas emissions by replacing fossil fuel dependent heating and cooling systems. Although ATES systems are limited to aquifers and have more geographical limitations, they have lower initial drilling and equipment expenditures with high maintenance cost whereas closed loop systems have lower manufacturing and maintenance costs (Lee, 2013) compared to aquifer thermal energy storage systems. BTES systems are generally easier to construct and operate and have proven long term durability. Yet, their payback times are relatively long compared to ATES systems, normally 6–10 years due to expensive borehole investments and the fact that BTES systems normally need some other sources to cover the peak load situations (Lanahan and Tabares-Velasco, 2017). Within the scope of this paper, Aquifer Thermal Energy Storage technique is primarily investigated and the principles of heat transfer, general design steps and some expressions related with the efficiency of the Aquifer Thermal Energy Storage technique is discussed.

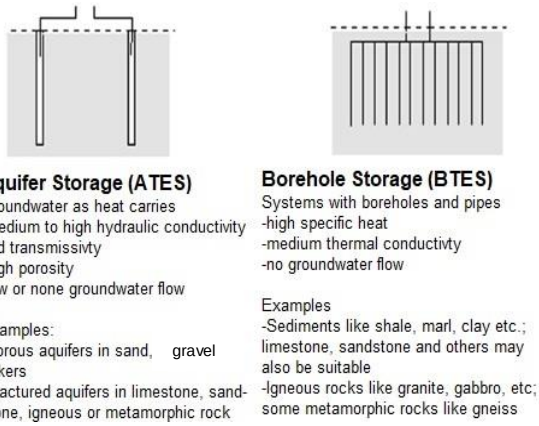

Fig. 7. Hydrogeological and thermolic parameters for ATES and BTES preferences (Sanner, 2001)

The installed ATES systems utilized in Sweden can be divided into four basic groups as to whether heat pump supported or not, as depicted in Figure 8 (Andersson *et al*., 2003). Groundwater is directly used for preheating of ventilation air during the winter by means of heat exchanger fluid at a temperature level of approximately +5 ˚C and for cooling during the summer season at a temperature level of approximately +15 ˚C in the simplest system (Figure 8a). The system (Figure 8b), having the same working principle as (Figure 8a), is more frequently implemented as the heat production in which the temperature change is somewhat greater. System (Figure 8c) stands for an early type of ATES utilization where surface water is used as a source of energy for the heat pump. The fourth system (Figure 8d) has a similar working principle with the system (Figure 8c); however, in this case already cooled reservoir during winter season is used for district cooling. In the same study, it is shown that the energy savings can reach up to 90–95% for direct heating and cooling, 80–87% for heat pump assisted heating and cooling, 60–75% for heat pump assisted heating systems and 90–97% for district cooling.

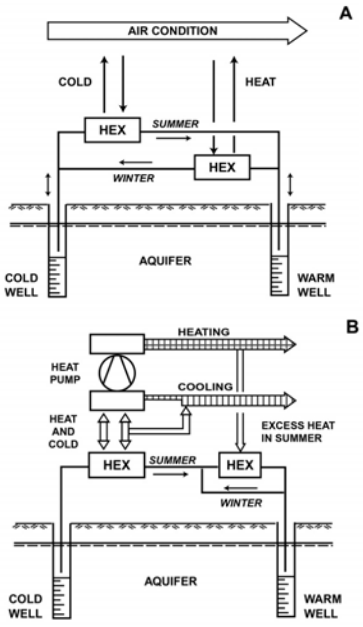

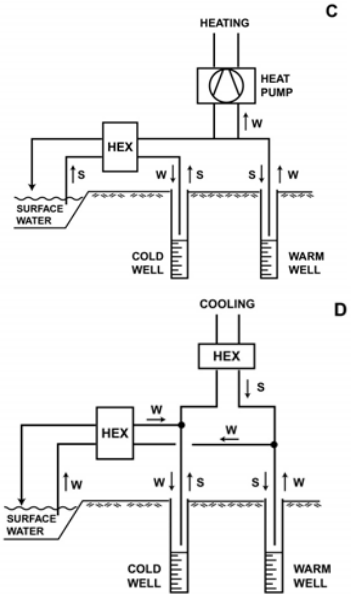

Fig. 8. Graphical representation of four basic ATES system configurations currently being used in Sweden. (a) Direct heating and cooling without heat pump (b) Heat pump supported heating and cooling (c) Heat pump supported heating only and (d) Storage of natural cold for cooling only (Andersson *et al.*, 2003).

When it comes to Turkey, although heat pump technology is well known, the number of applied underground thermal energy applications is limited. Ground source heat pump applications are summarized in a study performed by Çetin and Paksoy (2013). The first applications of shallow geothermal systems were encountered in early 2000 (Babur, 1986; Kara, 1999). The recent projects in Turkey indicate that the people's trust and awareness in these systems are increasing (Çetin and Paksoy, 2013). Moreover, Paksoy (1999) mapped the suitable areas for underground thermal energy storage applications in Turkey (Figure 9). It is observed that probable application areas for underground thermal energy storage are very broad considering the housing and industrial sectors, which share the first two orders of energy consumption in Turkey.

In addition to energy concerns, a study related to the mitigation of CO_2 emissions has been performed by utilizing different TES concepts in Turkey; one is for the heating and cooling of a supermarket utilizing aquifer thermal energy storage in Mersin and the other one for a greenhouse in Adana (Paksoy *et al.*, 2009). It is concluded that the yearly CO_2 emission has been reduced by 113 tons/year in the first project, performed in Mersin for a supermarket, and by 26 tons/year in the second project while providing energy conservation rates up to 60% and 68%, respectively.

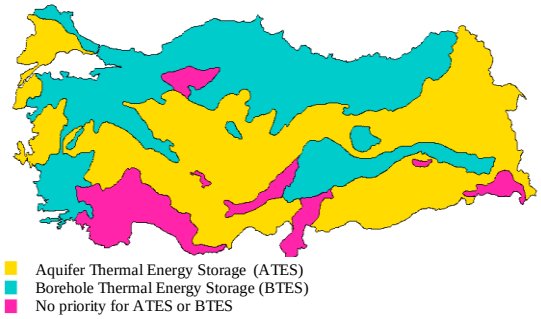

Fig. 9. Map showing potential areas of underground thermal energy storage application in Turkey (Paksoy, 1999).

2.2. The Design of Groundwater Based Open Loop Systems

Aquifer thermal energy storage (ATES) system generally consists of one or more pairs of tube wells that extract and simultaneously infiltrate groundwater to extract or store thermal energy in or from the subsurface by altering the temperature of the ground and groundwater. The thermodynamic transfer and storage is governed by advection, conduction or diffusion and dispersion as illustrated in Figure 10 (Courtois *et al.*, 2007). In the shallow subsurface environment, conduction through minerals or pore fluids and convection via groundwater are the two most important mechanisms of heat flow. In some cases, radiation may also be significant.

Diffusion or heat conduction describes the process by which heat transfers through a solid, liquid or gas by processes of molecular interaction. This process, formulized by Fourier's law, depends on the thermal conductivity and heat capacity of the aquifer. In a composite medium such as an aquifer, the thermal properties of both the fluid and the solid play essential role in heat transport. Advection describes the movement of thermal energy directly due to the linear flow of groundwater through the porous medium. The process represents the movement of the thermal stock due to the natural flow of the aquifer. Movement adds a spreading out of the thermal stock due to spatial heterogeneity of the velocity field, which is called as dispersion. This phenomenon leads to an increase of the global aquifer thermal conductivity. The physical processes of conduction (diffusion) and convection govern the transport and storage of heat in an aquifer. Thermal conductivity and volumetric heat capacity of some common TES materials are given in Table 2.

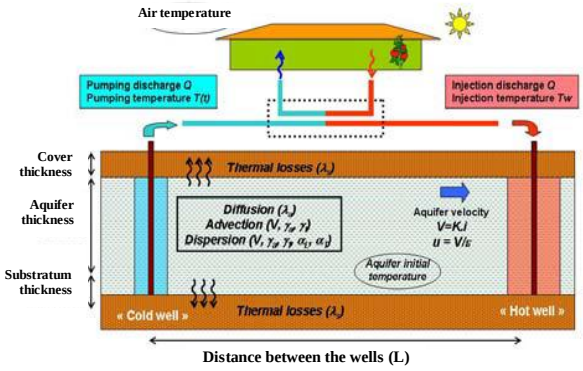

Fig. 10. Basic principle of thermal energy transfer in the subsurface (Courtois *et al.*, 2007).

Researches on analytical methods for heat transfer have been conducted by Sauty *et al.* (1982), Uffink (1983), Voigt and Haefner (1987), Krarti and Claridge (1990), Yang and Yeh (2002), and Stopa and Wojnarowski (2006). It is pointed out that analytical solution is only applicable to the qualitative estimations or to the simple cases (Kangas and Lund, 1994). For this reason, it would be more realistic to simulate the heat transfer by performing the numerical modeling of complex geological and hydrological characteristics (Tsang, 1983). Nowadays numerical modeling studies are carried out to predict recovery temperature by heat loss (Lee, 2008; Molson *et al.*, 1992), injection depth (Lee, 2008; Tenma *et al.*, 2003), injection time (Tenma *et al.*, 2003) and regional groundwater flow (Kangas and Lund, 1994).

As it can be seen in Figure 10, the wells are separated by a critical distance to ensure that the warm and cold storage remain separate. This interval, called critical distance (L), prevents the occurrence of thermal breakthrough within one season. The critical distance is primarily a function of operational and thermo-hydraulic parameters involving the well production rates, the aquifer thickness, and the hydraulic and thermal properties that control the storage volume. Clyde and Madabhushi (1983) have proven that the critical distance (L) preventing hydraulic breakthrough is explained by the following equation;

$$L < 2Z/\pi Ti \qquad (1)$$

where Z is the groundwater discharge, i is the natural hydraulic gradient and T is the aquifer transmissivity, multiplication of the depth of the aquifer with hydraulic conductivity K, which is a measure of the rate at which water moves through a unit width of the aquifer under a unit hydraulic gradient. The diagrams of the hydraulic breakthrough and the location of the extraction and injection well doublet system placed greater and less than the critical distance are illustrated in Figs. 11(a) and 11(b).

Table 2. Thermal properties of selected rocks and minerals (Banks, 2012).

	Thermal conductivity ($W m^{-1} K^{-1}$)	Volumetric heat capacity ($MJ m^{-3} K^{-1}$)
Rocks		
Coal	*0.3*	*1.8*
Limestone	1.5–3.0 (*2.8, massive limestone*)	1.9–2.4 (*2.3*)
Shale	1.5–3.5 (*2.1*)	*2.3*
Basalt	1.3–2.3 (*1.7*)	*2.4*–2.6
Diorite	1.7–3.0 (*2.6*)	*2.9*–3.3
Sandstone	2.0–6.5 (*2.3*)	*2.0*–2.1
Gneiss	2.5–4.5 (*2.9*)	2.1–2.6 (*2.1*)
Arkose	2.3–3.7 (*2.9*)	*2.0*
Granite	3.0–4.0 (*3.4*)	1.6–3.1 (*2.4*)
Quartzite	5.5–7.5 (*6.0*)	1.9–2.7 (*2.1*)
Minerals		
Plagioclase	1.5–2.3	1.64–2.21
Mica	2.0–2.3	2.2–2.3
K-feldspar	2.3–2.5	1.6–1.8
Olivine	3.1–5.1	2.0–3.6
Quartz	7.7-7.8	1.9–2.0
Calcite	3.4-3.6	2.24
Pyrite	19.2–23.2	2.58
Galena	2.3–2.8	1.59
Haematite	11.3–12.4	3.19
Diamond	545	–
Halite	5.9–6.5	1.98
Other		
Air	0.024	1.29×10^{-3} at 1 atm
Glass	0.8–1.3	1.6–1.9
Concrete	0.8–1.7 (*1.6*)	*1.8*
Ice	1.7–2.0 (*2.2*)	*1.9*
Water	*0.6*	4.18
Copper	390	3.5
Freon-12[a] at 7°C (liquid)	0.073	1.3
Oak	0.1–0.4	1.4
Polypropene	0.17–0.20	1.7
Expanded polystyrene	0.035	–

In order to determine the optimum well distance, besides thermal breakthrough, thermal interference for open loop doublet systems should be taken into consideration in terms of thermal radius which is described as the maximum distance of the thermal front from the injection well in a homogeneous medium, neglecting vertical flow, advection by regional flow, thermal conduction and dispersion (Bloemendal *et al.*, 2014). Previous studies have shown that the thermal radius (R_{th}) of an ATES can be calculated by setting the injected energy ($c_w.V.\Delta T$) equal to the energy stored in a cylinder, centered around the injecting well ($c_a.H.\pi.R_{th}^2$), yielding the Eq. (2). This serves as a first order approximation of the thermally affected area around an ATES well, where c_w and c_a are the volumetric heat capacity of water and the aquifer, respectively, V is the volume of water that is injected in one storage cycle and H is the length of the well screen (Sommer *et al.*, 2013). It should be noted that the actual affected area may be different from this approximation caused by thermal conduction, dispersion, heterogeneities and the presence of flow components other than radial type flow.

$$R_{ty} = (c_w V/c_a \pi H)^{0.5} \qquad (2)$$

In a numerical modeling study performed by Kim *et al.* (2010), it is reported that the thermal interference, influencing the performance of an aquifer thermal energy system, depends primarily on the hydraulic conductivity of an aquifer, the distance between two boreholes and the production/injection rate of the wells. They suggest that the thermal interference increases as the hydraulic conductivity increases, as the distance between two boreholes decreases and as the pumping/injection rate increases.

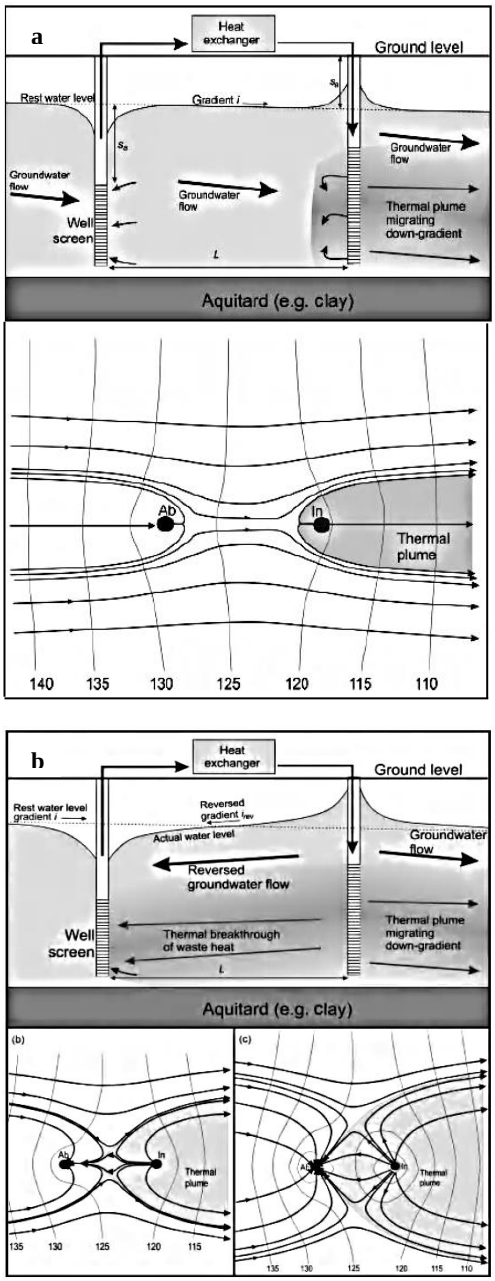

Fig. 11. An open well doublet system having a well to well distance of a) greater than the critical distance (L), b) significantly less than the critical distance, and the lower diagrams show the plan view. Black arrows show groundwater flow lines for both systems where there is a hydraulic feedback in system "b" (Banks, 2012).

The amount of energy that is recovered from the aquifer is generally lower than the amount that is stored because part of the energy is lost due to dissipation of heat to the surroundings of the storage and advection with regional groundwater flow. This energy loss is expressed as thermal recovery (η_{rec}) of a well (Bakr *et al.*, 2013; McDaniel and Kosanovic, 2016),

$$\eta_{rec}=E_{extracted}/E_{injected} \quad (3)$$

Additionally, Kim *et al.* (2010) report that the recovery of thermal energy is not considerably affected when the wells are located by more than one thermal radius, while Kowalczyk and Havinga (1991) report that there should be a well-to-well distance between one and two thermal radii. Sommer *et al.* (2013) explain that there should be a well distance of at least two thermal radii to avoid thermal interference in both homogeneous and heterogeneous aquifers. The Dutch Society for Subsurface Heat Storage (NVOE, 2006) advises that the thermal recovery decreases for well distances less than three thermal radii. Moreover, a detailed numerical simulation study was performed by Lee (2010) showing the effect of interwell distance on the normalized thermal storage. Although there are uncertainties related to the available aquifer thickness, aquifer heterogeneity, and uncertainty and variability in future energy demands, above mentioned interwell distance assumptions might be a preliminary design step.

Selection of a suitable aquifer in terms of the groundwater flow velocity is another significant criterion in the design of an ATES system. Numerical modeling study of a doublet open loop thermal energy storage system pointed out that thermal recovery in a stagnant aquifer can be higher than 75% and drop to 40% with a regional groundwater flow velocity of 150 m/year (Sommer *et al.*, 2013) whilst field studies report thermal recovery values range between 65% and 82% (Molz *et al.*, 1981). To reduce the dissipative heat loss due to the groundwater flow as depicted in Figure 12 (Groot, 2014), the aquifer should have a low hydraulic gradient. In general, suitable aquifers should readily yield water and have a low hydraulic gradient to prevent the stored energy to be transported outside the capture zone of the well (Hamada *et al.*, 2002). Care should also be taken to select appropriate materials according the chemical composition of the soil and groundwater to prevent well clogging. According to Andersson (2007), three main clogging processes are reported as clogging by fines, hydrochemical clogging and biochemical clogging. Injection wells require specialist design and construction since they are more susceptible to clogging and degradation of performance than abstraction wells. The re-injected water must be particle free to prevent clogging of the well screen or aquifer. The maximum allowed velocity limiting the well-clogging on the walls of borehole is given by the equation below (NVOE, 2006),

$$v_{inject} = 1000(K_s/150)^{0.6}\left[(v_{cl}/2MFI_{mem}u_{eq})^{0.5}\right] \quad (4)$$

Where v_{inject} is the design injection Darcy velocity on the walls of the borehole (m/h), v_{cl} is the specific clogging speed (m/year), MFI_{mem} is the measured membrane filter index (s/l^2) (Olsthoorn, 1982) and u_{eq} is the number of equivalent full load hours the well pumps per year (Buik and Snijders, 2006).

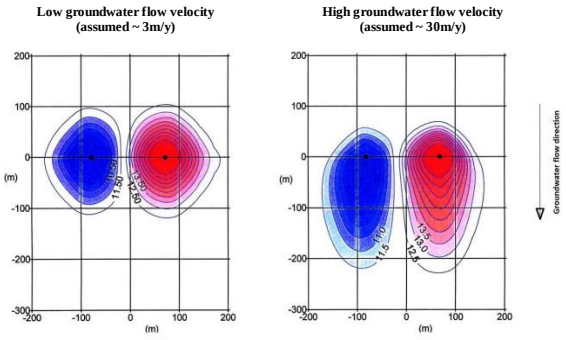

Fig. 12. Influence of groundwater flow velocity and direction on the stored heat of ATES systems (Groot, 2014).

3. CONCLUSION

Thermal energy storage in aquifers has a long history while achieving broad acceptance for heating and cooling in the energy market in many countries, with the Netherlands and Sweden as dominating countries of implementation. A brief summary related to the history of the thermal energy storage applications have been presented in this study. In addition, general design procedures and construction techniques as well as relationships related with the efficiency of ATES systems present in the most up-to-date literature are reviewed within the scope of this paper. The applications from the world and Turkey were discussed in a comparative approach.

The temperatures below ground surface at shallow depths are always higher than outside air temperatures in winter and are lower in summer. The temperature differences make shallow-depth soils and aquifers an efficient media for heat storage. Energy storage can be achieved by pre-heating operation in winter and pre-cooling operation in summer by means of ground heat exchangers. Aquifer thermal energy storage (ATES) systems take advantage of natural groundwater in a saturated and permeable layer as the storage medium. The transfer of thermal energy is carried out by extracting groundwater from the aquifer and by reinjecting it at a modified temperature into a separate well nearby. In the present work, a brief review is presented on the concepts and applications of ATES systems.

Any ATES project involves a complex procedure depending on many parameters and has to follow a standardized approach for design and field application. The heat transfer and storage in an aquifer can be modeled with analytical or numerical approaches. As the analytical solutions are limited with the simple cases, numerical modeling studies to simulate complex heat transfer processes within the aquifer thermal energy storage involving multiple injection/extraction systems should be performed. When it comes to the general design procedure of an ATES system, to avoid occurrence of thermal breakthrough within a season, the wells should be separated by a critical distance to ensure that the warm and cold storage remain separate. This distance is a function of operational and thermo-hydraulic parameters. Some of the previous studies show that there should be a well distance of at least one thermal radius to avoid thermal interference while other studies suggest at least two thermal radii whereas the Dutch Society for Subsurface Heat Storage advises at least three thermal radii for this purpose.

Selection of a suitable aquifer in terms of the groundwater flow velocity is another significant criterion in the design of an ATES system. The aquifer should have a low hydraulic gradient so as to reduce the dissipative heat loss due to the groundwater flow. Moreover, care should also be taken to select appropriate materials in terms of the chemical composition of the soil and groundwater to prevent well clogging. Injection wells require specialist design and construction since they are more susceptible to clogging and degradation of performance than abstraction wells. The re-injected water must be particle free to prevent clogging of the well screen or aquifer**.**

ATES applications in Turkey are still emerging. Hence, more effort should be performed to carry research to put forth the aquifer energy storage potential of Turkey. These studies should basically concentrate on the proper determination of aquifer parameters such as volume, seepage velocity and temperatures as well as the thermal conductivity and specific heat values of shallow soils and rocks around Turkey.

REFERENCES

Andersson, O., Hellström, G., and Nordell, B. (2003). Heating and cooling with UTES in Sweden-current situation and potential market development. FUTURESTOCK'2003, pp. 209-215.

Andersson, O. (2007). "Aquifer thermal energy storage (ATES)." *Thermal Energy Storage for Sustainable Energy Consumption*, Paksoy, H.O., Edit., Springer, Dordrecht, The Netherlands, pp. 155-176.

Babur, N. (1986). Design and Construction of an Earth Source Heat Pump, M.Sc. Thesis in Mechanical Engineering, Middle East Technical University, Ankara, Turkey.

Bakr, M., Oostrom, N.V. and Sommer, W. (2013). "Efficiency of and interference among multiple aquifer thermal energy storage systems, a Dutch case study." *Renewable Energy*, Vol. 60, pp. 53–62.

Banks, D. (2012). *An Introduction to Thermogeology: Ground Source Heating and Cooling*. Wiley-Blackwell Publication, UK.

Bloemendal, M., Olsthoorn, T., and Boons, F. (2014). "How to achieve optimal and sustainable use of the subsurface for Aquifer Thermal Energy Storage." *Energy Policy* Vol. 66, pp. 104-114.

Buik, N., and Snijders, A.L. (2006). "Clogging rate of recharge wells in porous media." *Proceedings Megastock*, Pomona, NJ, USA.

Cao, S. (2010). State of the art thermal energy storage solutions for high performance buildings. Master's Thesis, University of Jyväskylä, Finland.

Çetin, A. and Paksoy, H. (2013). "Shallow geothermal applications in Turkey." *EGC2013*, Pisa, Italy.

Clyde, C. G. and Madabhushi, G. V. (1983). "Spacing of wells for heat pumps." *Journal of Water Resources Planning and Management*, Vol. 109, No.3, pp. 203-212.

Courtois, N., Grisey, A., Grasselly, D., Menjoz, A., Noel, Y., Petit, V., and Thiery, D. (2007). "Application of Aquifer Thermal Energy Storage for heating and cooling of greenhouses in France: a pre-feasibility study." *European Geothermal Congress 2007*, Unterhaching, Germany.

Dincer, I. and Rosen, M. (2002). *Thermal energy storage: systems and applications*. John Wiley & Sons, United Kingdom.

Florides, G. and Kalogirou, S. (2007). "Ground heat exchangers-a review of systems, models and applications." *Renewable Energy*, Vol. 32, No. 15, pp. 2461–2478.

Furbo, S. (2014). *Using water for heat storage in thermal energy storage (TES) systems. Advances in Thermal Energy Storage Systems: Methods and Applications*, 1st ed., Woodhead Publishing.

Groot, J. H. (2014). Optimizing energy storage and reproduction for Aquifer Thermal Energy Storage. A scientific approach in enhancing ATES system performance at Achmea Apeldoorn through application of smart extraction and infiltration strategies. MSc Thesis, University Utrecht, The Netherlands.

Hamada, Y., Marutani, K., Nakamura, M., Nagasaka, S., Ochifuji, K. and Fuchigami, S. (2002). "Study on underground thermal characteristics by using digital national land information, and its application for energy utilization." *Applied Energy*, Vol. 72 No. 3– 4, pp.659–675.

Kangas, M. T. and Lund P. D. (1994). "Modeling and simulation of aquifer storage energy systems." *Solar Energy*, Vol. 53, No. 3, pp.237-247.

Kara, Y. A. (1999). Utilization of low temperature geothermal resources for space heating by using GHPs (in Turkish), Ph.D. Thesis, Ataturk University, Erzurum, Turkey.

Kim, J., Lee, Y., Yoon, W. S., Jeon, J. S., Koo, M. H. and Keehm, Y. (2010). "Numerical modeling of aquifer thermal energy storage system." *Energy* Vol. 35, No.12, pp.4955–4965.

Kowalczyk, W. and Havinga, J. (1991). "A case study on the influence of the distance between wells on a doublet well aquifer thermal performance." *Termastock 91, 5th International Conference on Thermal Energy Storage*, Utrecht, Netherlands.

Krarti M. and Claridge D. E. (1990). "Two-dimensional heat transfer from earth-sheltered buildings." *Journal of Solar Energy Engineering*, Vol. 112, No. 1, pp. 43-50.

Lanahan, M. and Tabares-Velasco, P. C. (2017). "Seasonal thermal-energy storage: a critical review on BTES systems, modeling, and system design for higher system efficiency." *Energies*, Vol. 10, No. 6, pp.743.

Lee, K. S. (2008). "Performance of open borehole thermal energy storage system under cyclic flow regime." *Geosciences Journal*, Vol. 12, No. 2, pp.169-175.

Lee, K. S. (2010). *Numerical Simulation on the Continuous Operation of Aquifer Thermal Energy Storage System*. Energy Storage, InTech.

Lee, K. S. (2013). *Underground Thermal Energy Storage*, Springer, London.

McDaniel, B. and Kosanovic, D. (2016). "Modeling of combined heat and power plant performance with seasonal thermal energy storage." *Journal of Energy Storage*, Vol. 7, pp.13-23.

Molson, J. W., Frind, E. O. and Palmer, C. D. (1992). "Thermal energy storage in an unconfined aquifer 2. Model development, validation, and application." *Water Resources Research*, Vol. 28, No. 10, pp. 2857-2867.

Molz, F. J., Parr, A. D. and Andersen, P. F. (1981). "Thermal energy storage in a confined aquifer: second cycle." *Water Resources Research* Vol. 17, No.3, pp. 641-645.

Nielsen, K. (2003). *Thermal energy storage, a state-of-the-art*. NTNU, Trondheim.

Novo, A. V., Bayon, J. R., Castro-Fresno, D. and Rodriguez-Hernandez, J. (2010). "Review of seasonal heat storage in large basins: Water tanks and gravel-water pits." *Applied Energy*, Vol. 87, pp. 390-397.

NVOE, (2006). *Werkwijzen en richtlijnen ondergrondse energieopslag (Methods and guidelines underground energy storage)*. Nederlandse vereniging voor ondergrondse energieopslag (Dutch society for subsurface energy storage).

Olsthoorn, T. N. (1982), *The Clogging of Recharge Wells, Main Subjects*, Kiwa communication No. 72, Rijswijk, Netherlands, pp.136.

Paksoy, H. O. (1999). "Underground thermal energy storage potential in Turkey." *IEA ECES* Annex 8 report, Berlin, Germany.

Paksoy, H., Evliya, H., Bozdag, Ş., Mazman, M., Konuklu, Y., Turgut, B., Gök, Ö., Yılmaz, M., Yılmaz, S, and Beyhan, B. (2009). "CO_2 mitigation with thermal energy storage." *International Journal of Global Warming*, Vol. 1, No.1-3, pp.253-269.

Rosen, M. A., Dincer, I. and Pedinelli, N. (2000). "Thermodynamic performance of ice thermal energy storage systems," *ASME-Journal of Energy Resources Technology* Vol. 122, No. 4, pp. 205–211.

Sanner, B. (2001). "Shallow geothermal energy." *GHC Bulletin*, 22, pp. 19-25.

Sanner, B., Constantine, K., Mendrinos, D. and Rybach, L. (2003). "Current status of ground source heat pumps and underground thermal energy storage in Europe." *Geothermics*, Vol. 32, pp.579-588.

Sauty, J. P., Gringarten A. C., Menjoz, A. and Landel, P.A. (1982). "Sensible energy storage in aquifers: 1. Theoretical study." *Water Resources Research*. Vol.18, No. 2, pp. 245-252.

Sommer, W. T., Valstar, J., Gaans, P. V., Grotenhuis T. and Rijnaarts, H. (2013). "The impact of aquifer heterogeneity on the performance of aquifer thermal energy storage." *Water Resources Research*, Vol. 49, No. 12, pp. 8128-8138.

Sommer, W., Valstar, J., Grotenhuis, T. and Rijnaarts,H. (2014). "Optimization and spatial pattern of large-scale aquifer thermal energy storage." *Applied Energy*, Vol. 137, pp. 322-337.

Stopa, J. and Wojnarowski, P. (2006). "Analytical model of cold water front movement in a geothermal reservoir." *Geothermics*, Vol. 35, No. 1, pp. 59-69.

Tenma, N., Yasukawa, K. and Zyvoloski, G. (2003). "Model study of the thermal storage system by FEHM code." *Geothermics*, Vol. 32, No. 4-6, pp. 603-607.

Tsang, C. F. (1983). "Aquifer simulation-in theory and in practice." *Proceedings of the international conference on subsurface heat storage in theory and practice*, Stockholm, Sweden, 116-125.

Uffink, G. J. M. (1983). "Dampening of fluctuations in groundwater temperature by heat exchange between the aquifer and the adjacent layers." *Journal of Hydrology*, Vol. 60, No. 1-4, pp.311-328.

Voigt, H. D. and Haefner, F. (1987). "Heat transfer in aquifers with finite caprock thickness during a thermal injection process." *Water Resource Research*, Vol. 23, No. 12, pp. 2286-2292.

Yang, S. Y. and Yeh, H.D. (2002). "Solution for flow rates across the wellbore in a two-zone confined aquifer." *Journal of Hydraulic Engineering*, Vol. 128, No. 2, pp. 175-183.

Turkish Journal of Engineering

Turkish Journal of Engineering (TUJE)
Vol. 2, Issue 2, pp. 49-53, May 2018
ISSN 2587-1366, Turkey
DOI: 10.31127/tuje.339946
Research Article

AUTOMATIC SLIDING DOOR ROPE MECHANISM DESIGN FOR VEHICLES

Hüseyin Mutlu *[1], Burak Emre Yapanmış [2] and Alper Günöz [3]

[1] Mersin University, Engineering Faculty, Mechanical Engineering Department, Mersin, Turkey
ORCID ID 0000-0002-4770-2873
huseyinmutlu@yahoo.com

[2] Mersin University, Engineering Faculty, Mechanical Engineering Department, Mersin, Turkey
ORCID ID 0000-0003-0499-6581
burakemreyapanmis@gmail.com

[3] Mersin University, Engineering Faculty, Mechanical Engineering Department, Mersin, Turkey
ORCID ID 0000-0001-7978-6306
alper.gunoz@gmail.com

* Corresponding Author
Received: 26/09/2017 Accepted: 19/11/2017

ABSTRACT
In the automotive sector, doors have an important issue in terms of vehicle and passenger safety. Therefore, different kinds of materials and mechanisms have been being designed and parameters have been being investigated and analyzed in order to increase the functional efficiency of the vehicle doors. In this study, an automatic open/close mechanism is designed which can be used in all types of vehicles with sliding doors. Sliding door mechanism with rope system was analyzed and information about the parts of the mechanism was explained. Door weight, rope diameter, torque, opening time of the door parameters were examined. Finally, the designed mechanism has mounted to a vehicle and it has been observed to work successfully.

Keywords: *Vehicle Gate, Sliding Door, Rope Systems, Mechanism Design*

1. INTRODUCTION

Vehicle doors are an important part that allows people to get on and off the automobile. A lot of different type of door are used in vehicles according to user requirements, vehicle body designs, and vehicle types. However, sliding doors are preferred on commercial vehicles frequently because of the ease of getting on and off. Additionally, due to the ease of use, the sliding doors are becoming increasingly widespread in passenger cars nowadays. Consequently, the number of commercial works on sliding doors increases day by day.

The doors are not only used getting on and off the car. At the same time, in any unfavorable situation that may occur in traffic, it should be in a structure that protects passengers in dangerous situations. Further, the weight of the door has become a very important issue because of emission restrictions and fuel consuming in the automotive industry (Balaban, 2011).

Works about sliding door are performed at the beginning of 20th century by W Ellis who is the first person applies to patent. Its work appears the today's track system (Ellis, 1913). In spite of the fact that there are a lot of scientific work about sliding door (Ömür *et al*., 2014; Uzundere *et al*., 2014; Güven *et al*., 2015; Kurutluş *et al*., 2015), there is no enough work about sliding door mechanism. However, it can be found a lot of patent work about sliding door (Ellis, 1913; Övgü 2017; Ungetheim 2017).

In this study, a designed sliding door system for a commercial vehicle is considered and an automatic door opening mechanism with a rope system is designed instead of a brake system. The parameters such as door weight, opening and acceleration time, pulley diameter was examined and the necessary motor power and torque analysis were performed for each situation.

2. MATERIAL AND METHODS

This work is mainly to design a new rope-type mechanism that provides possibilities for automatic opening and closing of sliding doors. The designed mechanism consists mainly of pulley, rope and spring tension control unit. The pulley should be placed so that it can rotate in a fixed body and it should be a helical tooth with suitable step to wrap the rope in sufficient quantity on the cylindrical surface. One of the end of the rope should contact the sliding door and another end should contact with the cylindrical pulley's two plane faces.

In this design, the drum and tension control unit is housed in a closed box called the body so that the drive unit of the mechanism is isolated against external influences such as dust and dirt. One end of the rope is settled to the plane surface of the pulley, the other is mounted at the appropriate position of the sliding door by passing through two deflecting rollers placed on the guide rail. This flexibility allows easy assembling. The part of the rope, which is from the deflection roller to the drive pulley, is passed through a flexible protective pipe. In addition, thanks to the insertion of the sliding door mechanism's pulley and the tension control unit in a box, the area that covered by the drive motor are reduced as much as possible.

The constituent parts of the automatic sliding door opening-closing rope mechanism and the mechanism for the vehicle are shown in Figs. 1-3. Opening the sliding doors are provided by the movement of the sliding door on the guide rail as shown in Fig. 2.

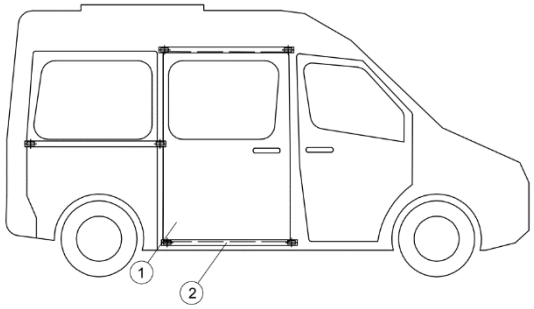

Fig. 1. General view of the vehicle where the system is used

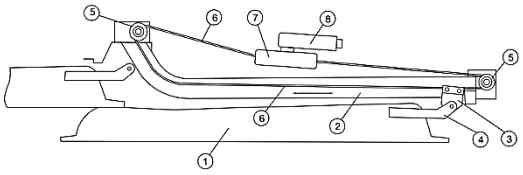

Fig. 2. The assembly view of the mechanism to sliding door

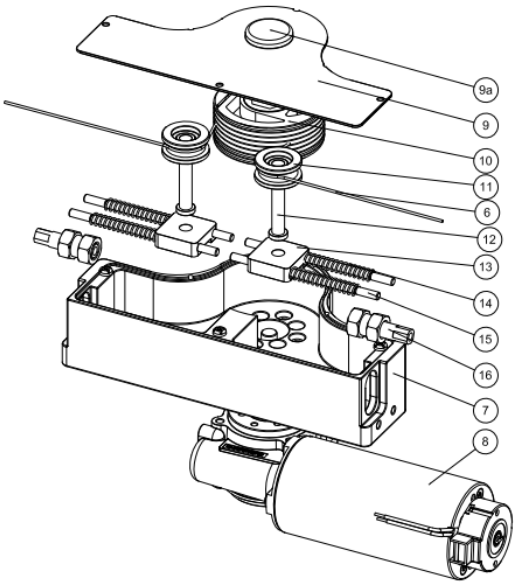

Fig. 3. Exploded view of the mechanism

In Fig. 1, number 1 represents car with sliding door, number 2 is sliding door's guide rail. In Fig. 2, number 3 is sliding door rope fixing plate, number 4 is sliding door rope fixing support plate, number 5 is sliding door rope deflecting pulley, number 6 is drive rope, number 7 is rope drive mechanism's body and number 8 is drive motor. Number 9 is rope drive mechanism body cover, number 9 (a) rope drive mechanism body cover support projection, number 10 is rope driving's pulley, number 11 is tensioner roller, number 12 is tensioner roller's pin,

number 13 is tensioner pin bearing, number 14 is tension spring, number 15 is tension pin, number 16 is driving rope body entrance in Fig. 3.

The operating principle of the mechanism can be summarized as follows to Fig. 3 and Fig. 4. One of the drive ropes, which is shown number 6, is wrapping around the rope drive pulley which is shown in number 10. At the same time, the other drive rope exits from the drive pulley. The sliding door is pulled by the driving rope and moves on the sliding door's guide rail. Similarly, while the other drive rope is wrapping on the rope drive pulley by the rotation of the drive motor in the opposite direction, the other drive rope exits from the rope drive pulley and the sliding door is moved in the opposite direction. Owing to this two-way motion, the sliding door is opened and closed.

In design, different parameters such as door opening time, door weight and opened door interval are determined. Numerical values of these parameters; opening times of the door are selected as 6 seconds, door weights are 50 kg and 80 kg and open door intervals are selected as 0.8 m and 1.3 m. In addition, according to the market survey and literature about the design of the door opening/closing mechanisms is based on an assumption that on a 17-degree incline road (Güven *et al.*, 2015).

The speed time graph of the sliding door opening and closing motion in the vehicles used in the current market conditions is determined as in Fig. 4.

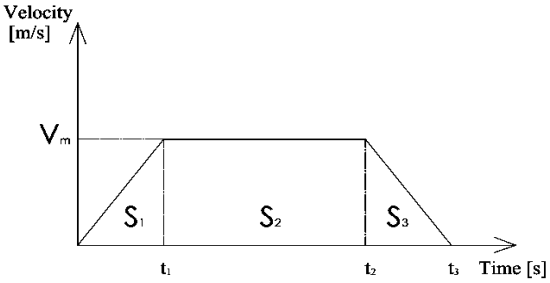

Fig. 4. Speed-time graph

The door is positive accelerating until V_m from 0 to t_1 intervals, is motion without acceleration at V_m from t1 until t_2 and it is negative accelerating until the speed reaches to zero from t_2 to t_3. The S_1, S_2, and S_3, which are domain under the velocity-time curve during the movement, represent distance. The dynamic movement and force characteristics of the door can be calculated by selecting the time periods t_1, t_2, and t_3.

It should be the operated to the drive mechanism in the critical position to calculate the maximum force values that occur in the ropes by the movement of the door. The free-body diagram of the vehicle operating at a slope of 17 ° is shown in Fig. 5.

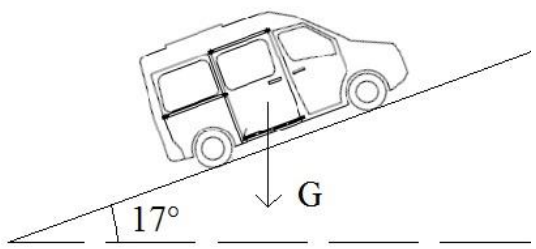

Fig. 5. Critical operation position

Thanks to the written equilibrium equations according to Newtonian motion law, the rope tension force (F1, F2, F3) in each range is calculated as follows;

$$F_1 = ma_1 + mg\sin\alpha + \mu mg\cos\alpha \quad (1)$$
$$F_2 = ma_2 + mg\sin\alpha + \mu mg\cos\alpha \quad (2)$$
$$F_3 = ma_3 + mg\sin\alpha + \mu mg\cos\alpha \quad (3)$$

Time dependent power (P) with the help of speed and force values; the time-dependent variation of the motor torque with the force and the radius of the pulley is obtained as follows;

$$P_1 = V_1F_1; \quad \tau_1 = F_1t_r \quad (4)$$
$$P_2 = V_2F_2; \quad \tau_2 = F_2t_r \quad (5)$$
$$P_3 = V_3F_3; \quad \tau_3 = F_3t_r \quad (6)$$

The speed time graph also informs the kinematic motion control characteristic of the drive motor. In order to calculate the dynamic force characteristic of the drive motor and the power values of the motor, the maximum distance was utilized from the speed-time graph in Fig. 5 and it is given in Eq. (7).

$$Smax = \frac{(t_1 - t_0)}{2} \cdot Vm + (t_2 - t_1)Vm + \frac{(t_3 - t_2) \cdot Vm}{2} \quad (7)$$

V_m with the required settings is as follows;

$$Vm = -\frac{2Smax}{t_1 - t_2 - t_3} \quad (8)$$

The velocities V_1, V_2 and V_3 depending on time (t) can be calculated using Equation 8 as follows;

$$V_1 = \frac{V_m(t - t_0)}{(t_1 - t_0)} \quad (9)$$
$$\boldsymbol{V_2 = V_m} \quad (10)$$
$$V_3 = \frac{V_m(t_3 - t)}{(t_3 - t_2)} \quad (11)$$

3. RESULTS

The torque and power values are numerically calculated according to the operating conditions. Door weights haven't got same values in existing cars with sliding door on the market. When these conditions are considered, the most common weights 50 kg and 80 kg are used. The opening time of the sliding door is defined as 6 seconds, and the deceleration times (t1 and (t3-t2)) are selected equal as 0.3 and 0.5 seconds are used. The engine torque was calculated taking into account the three-different selected radius 0.05, 0.07 and 0.09 meters. In the calculations, the gravitational acceleration (g) was assumed to be 9.81 m/s^2, and the friction coefficient (μ) was assumed to be 0.3.

Firstly, the engine torque-time graphs according to the

variation of the pulley radius are shown in Fig. 6. Power changing according to time for 50 and 80 kg door weights is shown in Fig. 7 and the changing of motor torque with time is shown in Fig. 8.

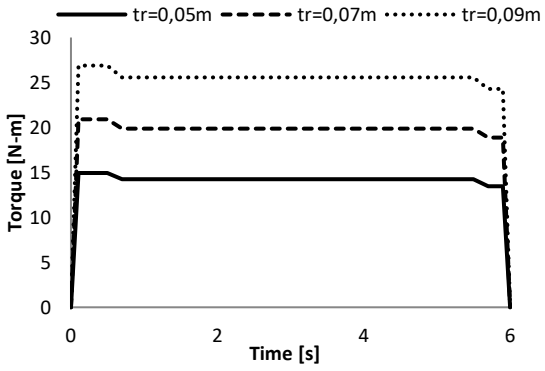

Fig. 6. Torque-time graph according to changing of the radius of the pulley

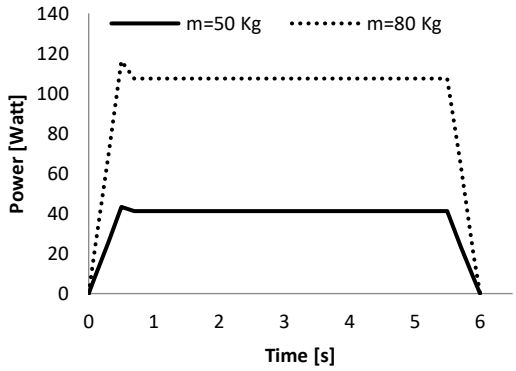

Fig. 7. Power-time graph according to changing door weight

As it is shown in Fig. 6 that the increase in the pulley radius caused the motor torque to increase. As a result of Fig 6, the best radius is chosen as 0.05 m.

Fig. 7 and 8 graphs show the variability in acceleration. There is a sudden rise in the beginning of each chart. The reason is that it is reached to a_1 acceleration from the speedless position. There is a small decreasing in curves due to $a_2 = 0$ and then it is going to stable until t_2 moment. Acceleration a_3 effects to system from time t_2 to time t_3. All graphics tend to decrease until reset because of a_3 which is being in the negative direction.

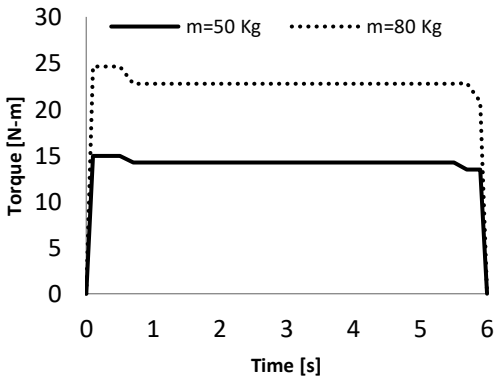

Fig. 8. Torque-time graph according to changing door weight

The changing of power and torque values taking into account two different starting and stopping times respectively 0.3 seconds and 0.5 seconds is shown in Fig. 9 and Fig. 10.

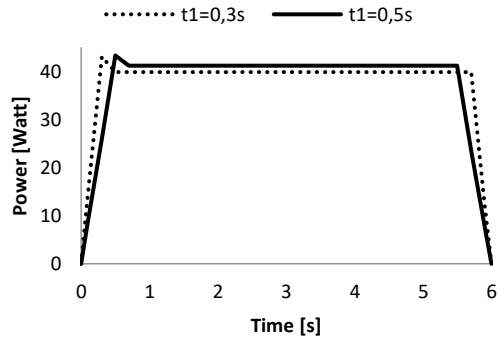

Fig. 9. Power-time graph according to changing door weight

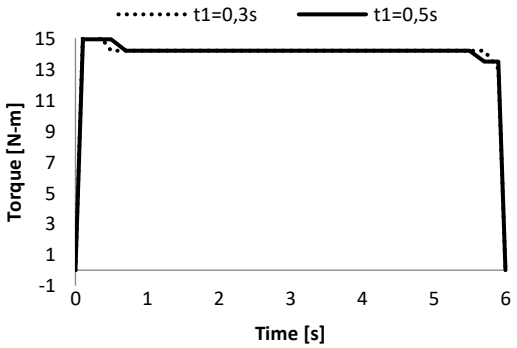

Fig. 10. Power-time graph according to changing door weight

In Fig. 9, it is shown that curves are a rapid increased until t_1. From t_2 to t_3, the acceleration is equal to zero, therefore, the curves a bit decreases then they tend to linear motion. After t_3, the curves have a rapid decrease owing to the fact that the acceleration acts in the negative direction and it is going on until power is equal to zero.

It is shown that increase of curve because of acceleration in Fig. 10. Acceleration of opening/closing time 0.3 second is bigger than the acceleration of opening/closing time 0.5 second. The curves show linear behavior because of non-acceleration after t_2. The curves show linear behavior because of non-acceleration from t_2 to t_3. After t_3, it is seen that the curves have decreased due to acceleration in the negative direction.

3.1. Experimental work

With the help of the numerical design algorithm, a prototype was designed and manufactured for a door weighing 50 kg, an acceleration time of 0.5 seconds and total time of opening 3 seconds, opened door interval 1.3 meters and a pulley diameter of 0.05 meters. The

experimental setup which is set up to test of the mechanism is shown in Fig. 11 and Fig. 12. The mechanism is mounted on a belt pulley kit which passes the driving rope through the deflection pulleys. The experimental works have been performed 120.000 rpm without any problem in this system.

Fig. 11. Experimental setup

Fig. 12. Application of the mechanism in the vehicle

4. CONCLUSION

Automatically opening and closing door mechanisms, which are frequently used in commercial and passenger vehicles, have an important place in the automotive sector. For this reason, different kinds of materials and mechanisms are designed and parameters are investigated and analyzed in order to increase the functional efficiency of the vehicle doors. In this work, information about the parts which is consist of the mechanism is given and different weight, duration and pulley diameter parameters have been determined to increase the efficiency of the mechanism, minimize the mounting difficulties and to supply flexible assembly possibility. In addition, it is desirable to have the structural and potential flexibility to versatile usage possibilities in consideration of market needs, as well as cost-effective. The necessary analysis is carried out to provide these situations and an automatic sliding door mechanism is designed. It has been seen that a sliding door mechanism, which is automatically opened-closed, has been tried and installed on a real car and worked successfully. This system can also be alternative solutions applying as an elevator door and sliding doors of the building.

REFERENCES

Balaban G. B., (2011). Otomotiv Kayar Kapı Mekanizmalarında Ağırlık Optimizasyonu, Master Thesis, University of Uludağ, Bursa, Turkey.

Guven C., Tufekci M., Bayik E., Gedik O., Tas M., (2015). "Experimental Verification and Finite Element Analysis of a Sliding Door System Used in Automotive Industry", *International Journal of Mechanical, Aerospace, Industrial, Mechatronic and Manufacturing Engineering*, Vol:9, No:10.

Uzundere C. M., Karakoç Ö. (2014). "Bir Taşıt Kayar Kapı Mekanizmasında Ayarlanabilir Kapı Durdurucu", *7th Automotive Technologies Congress*, Bursa, Turkey.

Kurtulus O., Yavuz C. (2015). "Examining the Modular End of Line Control Unit Design Criteria for Vehicle Sliding Door System Track Profile", *International Journal of Mechanical, Aerospace, Industrial, Mechatronic and Manufacturing Engineering*, Vol:9, No:10.

Ömür Ö.S., Rakipsiz C., Şengünalp H. (2014). "Sliding Door Design Without B-Pillar for Passenger Cars" *7th Automotive Technologies Congress*, Bursa, Turkey.

2017/06937, (2017). Sayan Ö., Gündoğdu Ö., Topçu L., Ölmez H., *Taşıtlara Yönelik Kayar Kapı*, Turkish Patent and Trademark Office, İstanbul, Turkey.

WO/2017/142909, (2017). *Method and Apparatus of Extending Opening Ranges of Vehicle Sliding Doors*, World Intellectual Property Organization, Arizona, US.

1055969, (1913). W. Ellis, *Sliding Vehicle Door*, United States Patent Office.

Turkish Journal of Engineering

Turkish Journal of Engineering (TUJE)
Vol. 2, Issue 2, pp. 54-59, May 2018
ISSN 2587-1366, Turkey
DOI: 10.31127/tuje.349532
Research Article

EXPERIMENTAL INVESTIGATION OF FLOW STRUCTURE DOWNSTREAM OF PERMEABLE CYLINDERS

Bengi Gözmen Şanlı *[1] and Hüseyin Akıllı [2]

[1] Mersin University, Faculty of Engineering, Department of Mechanical Engineering, Mersin, Turkey
ORCID ID 0000 – 0001 – 6805 – 2454
bengigozmen@mersin.edu.tr

[2] Cukurova University, Faculty of Engineering & Architecture, Department of Mechanical Engineering, Adana, Turkey
ORCID ID 0000 – 0002 – 5342 –7046
hakilli@cu.edu.tr

* Corresponding Author
Received: 06/11/2017 Accepted: 07/12/2017

ABSTRACT
Flow structure downstream of permeable cylinders was investigated using high-image density Particle Image Velocimetry technique in deep water. The free stream velocity is U_∞= 156 mm/s, which corresponds to the Reynolds number of Re=6250 based on the cylinder diameter D=37.5 mm. To reveal the effect of the porosity, four different porosities (β= 0.4, 0.5, 0.6 and 0.7) were used. This study showed that the usage of permeable cylinder decreases the occurrence of large-scale vortical structures downstream of the bluff body. As the porosity increases, turbulent kinetic energy, Reynolds shear stress and intensity of turbulences decrease as a sign of attenuated fluctuations in the wake region. For the permeable cylinders having the porosity higher than 0.6, the flow behaves as there is no object in flow.

Keywords: *PIV, Vortex Shedding, Permeable Cylinder, Deep Water*

1. INTRODUCTION

Circular cylinder is one of the most commonly used structures in many engineering applications because of its geometrical simplicity. In despite of the simple geometry, the flow around the cylinder is enough to explain complex phenomenon in the wake region. Therefore, many researchers have focused on the circular cylinder at the last century. Control of vortex shedding downstream of circular cylinders has a great importance and several control methods are used to suppress the pattern effect of vortex shedding. These methods are active and passive controls. At active control methods, there is an energy input into the flow region while passive control methods are based on the geometrical adjustments. Plasma actuators (Corke *et al*., 2010), synthetic jets (Feng and Wang, 2012; Akansu and Fırat, 2010), feedback controls (Muddada and patnaik, 2010; Hiejima *et al*., 2005) and suction and blowing (Li et al., 2003) are some of the active control methods. On the other hand, many passive control methods are used at the studies since applying passive control methods are easier than that of the active control methods. Gim *et al.* (2011) used control rods to control the flow. They attached the rod to the rearward stagnation point of a circular cylinder. They investigated the effect of sizes of control rods and Reynolds number. Lim and Lee (2003) researched the flow structure around a circular cylinder with U-grooved surfaces. They presented that the U-shaped grooves reduce the drag coefficient by18.6%, compared with that of plain cylinder. The Longitudinal grooves shifted the vortices position and shortened the vortex formation region in comparison to the plain cylinder. Nakamura and Igarshi (2008) controlled the vortex shedding by attaching cylindrical rings around the cylinder. They reduced drag and fluctuating forces. The drag force decreased by 15% for $Re_d \geq 20\ 000$. Ekmekci and Rockwell (2010) investigated experimentally the effect of a single wire attached on the outer surface and parallel to span of a stationary circular cylinder and they defined two critical angles effective on near-wake structure. At one critical angle, substantial extension occurred and at the other critical angle, significant contraction of the time-averaged near-wake bubble was obtained. Sahin and Smith (1987) used two perforated plates in order to control the velocity distribution emerging from a wide-angle, three-dimensional diffuser of area ratio 6.8. They showed that the most uniform velocity distributions in the collection chamber downstream of the diffuser were provided using two perforated plates of porosity $\beta = 0.5$. The best results were obtained with one of the plates positioned a short distance downstream of the diffuser entry plane ($L/W = 0.14$) with the second plate just upstream of the exit plane ($L/W=0.79$). Farhadi *et al.* (2010) studied on two-dimensional unsteady laminar flow over a semi-circular cylinder near a splitter plate numerically. They carried out numerical simulations for different Reynolds numbers ranging from 100 to 500 in three different gaps ($g = 0.0D$ to $4.5D$) and two different splitter lengths ($LSP = 1$ and $2D$). Their results of study signified that the vortex shedding formed in the wake and the oscillating amplitude of the lift coefficient was decreased by increasing the gap ratio. Sudhakar and Vengadesan (2012) researched the vortex shedding characteristics of a circular cylinder attached with an oscillating splitter plate, numerically. They forced the splitter plate to exhibit the simple harmonic motion. Gozmen *et al.* (2013) investigated the effect of splitter plates having different heights and lengths located in the wake region of the circular cylinder in shallow water. The results of their study pointed out that flow structures changed significantly with height and length ratios of the splitter plates in shallow water. The wake region downstream of the cylinder lengthened along the streamwise direction with increasing the plate length and depth. Al-Hajeri *et al.* (2009) investigated two-dimensional laminar flow past three circular porous cylinders arranged in an in-line array numerically. For the same range of Reynolds number (312-520), they indicated that flow behavior around the solid cylinder differed from the flow around the porous cylinders. The flow characteristics around solid cylinders were determined by the Reynolds number, whereas the flow characteristics around the porous cylinders were determined by the V (i)/V (f) ratio. Ozkan *et al.* (2012) carried out a study on the flow control around a circular cylinder surrounded by a permeable cylinder in shallow water. They revealed that both the porosity value and the diameter ratios were significant parameters on the suppression of vortex shedding downstream of the circular cylinder. Pinar *et al.* (2015) performed a study on the control of flow around the perforated cylinders having the porosities in the range of $0.1 \leq \beta \leq 0.8$ with an increment of 0.1. They presented that the fluctuations were reduced dramatically in the wake region by the use of perforated cylinders having the porosities in the interval of $0.4 \leq \beta \leq 0.8$. To reveal the effects of porosity on the suppression of vortex shedding, Gozmen and Akilli (2014) used permeable cylinders having various porosities and diameters to control the flow downstream of a solid cylinder. They indicated that the outer permeable cylinder decreased the wake instabilities and vortex shedding downstream of the cylinder arrangement depending on the porosity and the diameter ratio in deep water.

The main aim of this study is to investigate the flow structure downstream of the permeable cylinders having different porosities in deep water. In order to use permeable cylinders instead of solid cylinders, the vortex shedding in the wake region of only permeable cylinder was investigated inclusively. The experiments were conducted using permeable cylinders having four different porosities β with the diameter of cylinder $D=37.5$ mm.

2. EXPERIMENTAL SETUP

Experiments were carried out in a circulating rectangular open channel located at Fluid mechanics laboratory of mechanical engineering department of Çukurova University. The test section has a length of 8000 mm, a width of 1000 mm and a height of 750 mm. The PIV technique was applied to calculate the instantaneous and time-averaged velocity vector fields downstream of permeable cylinders. The free stream velocity, U was fixed at 156 mm/s as the Reynolds number was about 6250 depending on the diameter of permeable cylinder. The side view of experimental system is presented in Figure 1. Four different porosity values (β= 0.4, 0.5, 0.6, and 0.7) were selected to pointed out the effect of permeable cylinder having

different porosity on the flow structure. Meanwhile, porosity is defined as the ratio of gap area on the body to the whole body surface area. All permeable cylinders are made of a chrome-nickel wire mesh. During the experiments, the total depth of the water in the channel was adjusted 560 mm while the water height was maintained at 340 mm which corresponded to the distance from free surface to the base of the platform. The measurement of flow field was made at the mid-depth (h_L) of water above the platform. The permeable cylinder was placed to the location which was 1750 mm far away from the leading edge of the platform to assure the fully-developed boundary layer. The geometric blockage ratio was 4.5 %.

The experimental measurements were performed by using a PIV system. The PIV system is consisting of a pair of doubled-pulsed Nd:YAG laser, a CCD camera, a synchronizer and a grabber. A pair of double-pulsed Nd:YAG laser light sheet lightened the flow. The thickness of laser sheet was about 2 mm and the laser sheet was parallel to the surface of the platform during all experiments. As seeding particles, silver-coated hollow glass spheres with a mean diameter of 12 µm and a density of 1100 kg/m^3 were chosen which were assumed to follow the flow dynamics accurately. In addition, the non-dimensional Stokes number was calculated as 1.83×10^{-4} (Raffel *et al.*, 1998) for these particles. During the experiments, the images were recorded using a 8-bit charged-coupled device (CCD) camera with a resolution of 1600x1200 pixels, equipped with a Nixon AF micro 60 f/2.8D lens and furthermore, the camera and laser pulses were synchronized by a synchronizer.

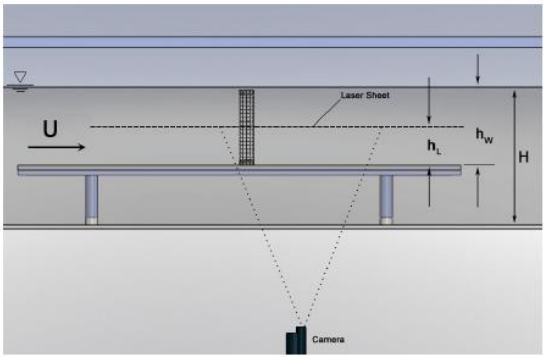

Fig. 1. Side view of experimental system

Quantative flow images were processed by Flow Manager Software. The cross-correlation method based on the Fast-Fourier-Transform (FFT) was used to calculate particle displacement. The interrogation area was selected as a grid size of 32x32 pixels overlapping by 50 %, which resulted in a set of 3844 vectors (62x62) for the flow field. In each experiment, 350 instantaneous images were captured and stored to calculate averaged-velocity vectors and other statistical properties of the flow field. During the experiments, two views one after the other were taken and every field of view was taken as 200x200 mm^2. The total uncertainty in velocity relative to depth-averaged velocity was estimated to be about 2 % for this arrangement.

3. RESULTS AND DISCUSSION

Fig. 2 displayed the Reynolds shear stress contours of permeable cylinders having the diameters of D=37.5 mm. To illustrate the effect of porosity, the Reynolds shear stress contours of bare cylinder and permeable cylinders having four different porosity values (β = 0.4, 0.5, 0.6 and 0.7) are shown in this figure. At this figure, the minimum and incremental values of $< u'v' >$ were taken as 0.0015 and 0.0015, respectively. The solid lines demonstrate positive (counter-clockwise) contours of Reynolds shear stress while the dashed lines demonstrate the negative (clockwise) contours. The normalized Reynolds shear stress contours determine significant information about the fluctuations in the wake region. It is clearly understood that the peak magnitude of Reynolds shear stress of the bare cylinder is about 0.048 and both large-scale clusters caused by the unsteady vortex shedding and small-scale clusters due to the small-magnitudes of the oscillations in the near wake of the cylinder are seen downstream of the bare cylinder. For the porosities of β = 0.4, 0.5, 0.6 and 0.7, in contrast to the bare cylinder case, there is no a distinct concentration in the Reynolds shear stress contours. The peak values o

f $< u'v' >$ are several times smaller than that of the bare cylinder case. As the porosity values increase, the concentration of Reynolds shear stress decreases significantly and the location of peak concentration of Reynolds shear stress moves further away from the base of the cylinder as a result of the increase in the open area on the surface of the permeable cylinder. For the porosities of β = 0.4, the peak magnitude of Reynolds shear stress is determined to be 0.0209. With increasing the porosity values from 0.6 to 0.7, the concentration of Reynolds shear stress significantly weakens at the centerline of the permeable cylinder. This decrease in the Reynolds shear stress may be directly related to the drag force reduction at the flow region as obtained by Fujisawa and Takeda (2003).

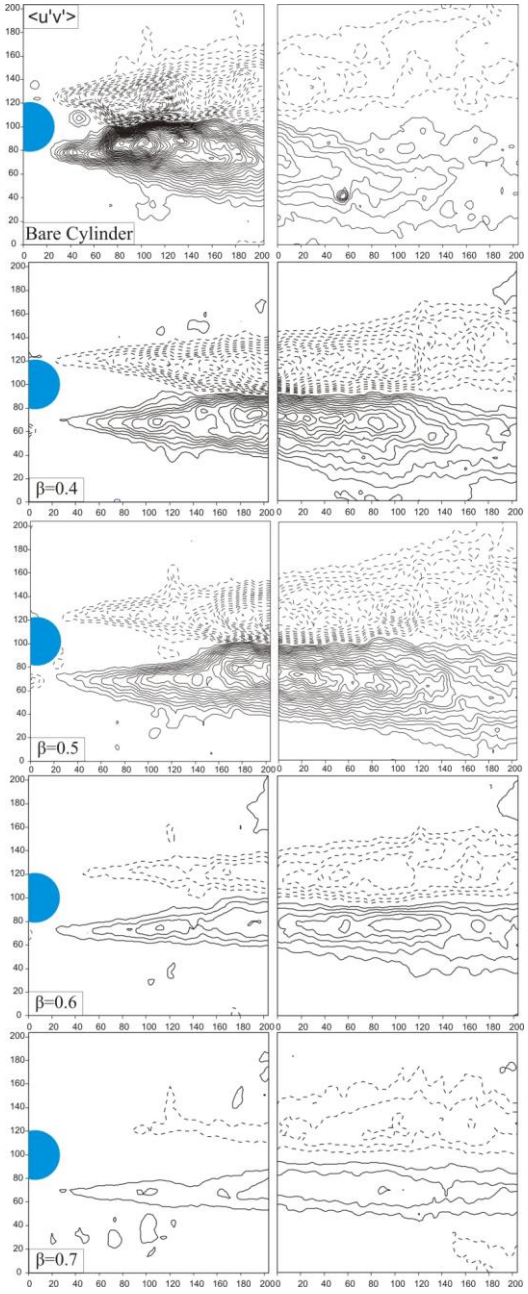

Fig. 2. Contours of Reynolds shear stress for the diameter of 37.5 mm

The time-averaged streamline topologies for various porosities at the cylinder diameters of D=37.5 mm are illustrated in Fig. 3. For bare cylinder case, two focus points (F1, F2) emerge in the close region of cylinder and a saddle point S occurs at the location which is considered at the end of vortex formation. Two-well defined foci, F1, F2 are nearly symmetrical with regard to the centerline and the shear layers occur in the first field of view. When all permeable cylinder cases are examined, the streamline topologies represent that neither foci nor saddle point appear downstream of the cylinder due to reduction in transverse velocity in the wake region. The streamlines lengthen in the streamwise direction without any circulation. Due to the non-appearance of the focal flow structure downstream of the permeable cylinder, the wake region length cannot be designated.

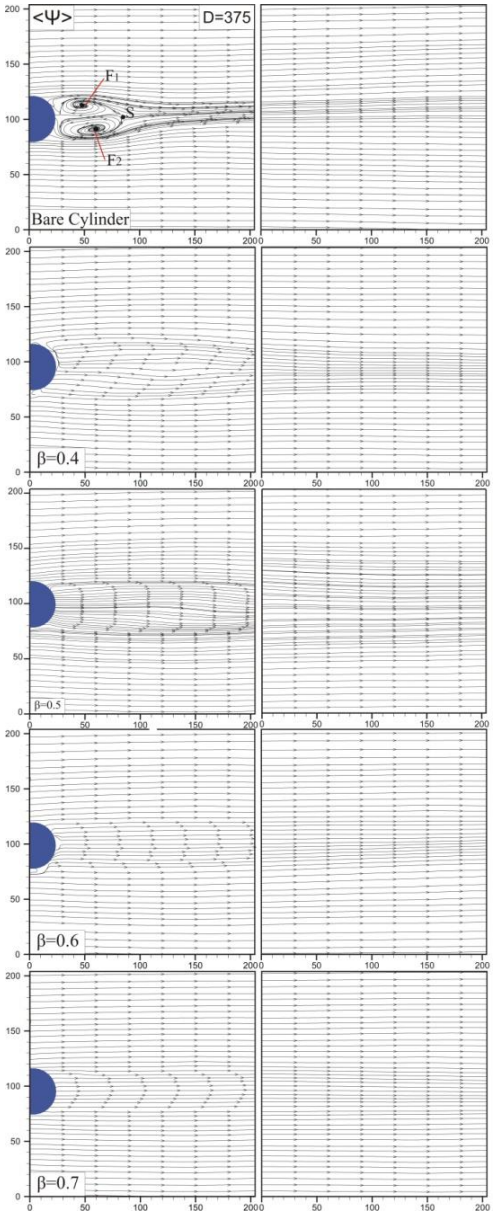

Fig. 3. Patterns of time-averaged streamline topologies for permeable cylinder having the diameter of 37.5 mm

The relationship between the peak value of turbulent kinetic energy and the porosity for the permeable cylinder and the peak value of turbulent kinetic energy of bare cylinder are indicated in Fig. 4 to reveal the effect of the porosity on the flow characteristics. The peak value of TKE of bare cylinder is greater than those of all permeable cylinders as a sign of large scale vortices which transfer momentum from the free-stream flow into the wake region. For permeable cylinders, the peak value of TKE decreases progressively with increasing of the porosity. For the porosity of $\beta = 0.7$, the peak value of TKE decreases to 0.019 several times smaller than that of the bare cylinder. This is an expected result since the open area on the surface of the permeable cylinder enlarges with the enhancement of

the porosity value. This implies that the permeable cylinders having the porosity higher than 0.6 do not pose an obstacle for the flow. This outcome is in accord with the results of Reynolds shear stress and the time-averaged streamline topologies.

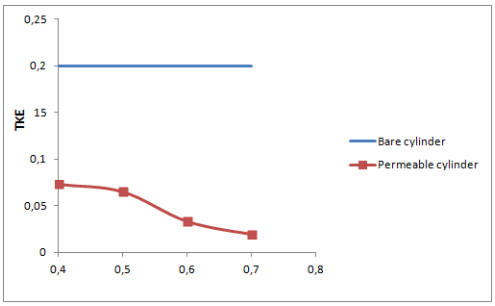

Fig. 4. The variation of peak value of TKE as a function of porosity for the permeable cylinder and peak value of TKE for bare cylinder

Fig. 5 presents contours of the time-averaged streamwise velocity <u>/U for the bare cylinder case and the permeable cylinder cases. The dashed lines present negative values of <u>/U, whereas the solid lines indicate positive values. The minimum and incremental values of the streamwise velocity contours were selected as ± 5 and 5, respectively. The substantial region of reverse flow is seen at the downstream of the bare cylinder as a consequence of the momentum transfer from the free-stream region into the wake region. The peak value of negative streamwise velocity is nearly 0,160. When the effects of permeable cylinders are examined, it is observed that the reverse flow does not form in the fields of view for all porosity values and the minimum value of streamwise velocity component increases and the location of the minimum value of streamwise velocity moves further downstream of the permeable cylinder with increasing the porosity.

The spectra of streamwise velocity fluctuations depicted in Fig. 6 (A) are evaluated at a certain location (A) which is 1D far away from the base of the cylinder for the bare cylinder and permeable cylinders having four different porosity values. For the bare cylinder case, natural frequency of vortex shedding is found to be f=0.73 Hz as a sign of occurrence of vortical structure in the wake region of the bare cylinder. For permeable cylinder cases, any clear and distinct peak of frequency cannot be observed. This denotes that the vortex shedding in the wake region is prevented. This result justifies the other evidences obtained from other figures in this study.

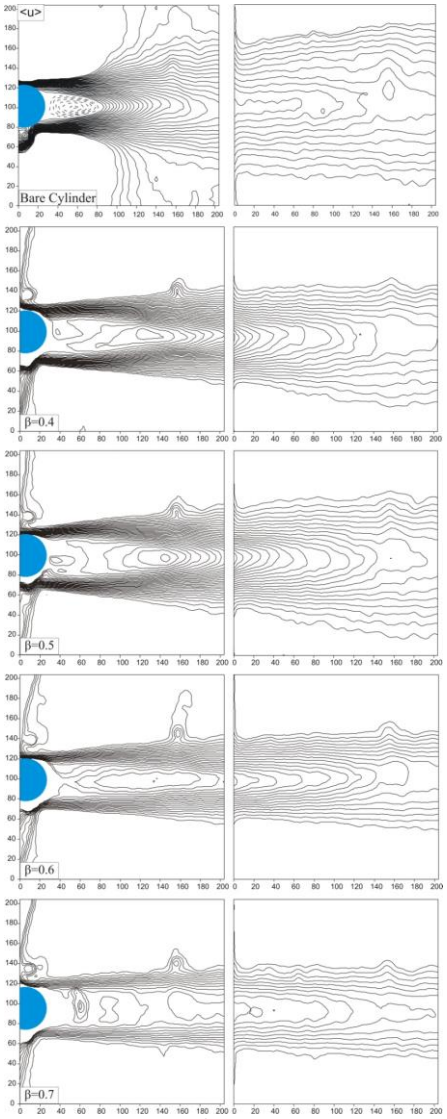

Fig. 5. Contour patterns of time-averaged streamwise velocity <u>/U for bare cylinder and the permeable cylinders having four different porosity values.

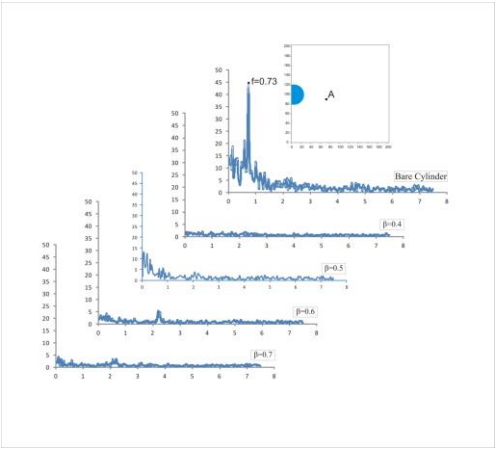

Fig.6. Spectral analysis of bare cylinder and permeable cylinders having the diameter of D=37.5 mm

4. CONCLUSION

In present study, the influence of permeable cylinder on the wake flow is experimentally investigated by the PIV technique in deep water. Four different porosity values for the permeable cylinders having D=37.5mm were used to find out the effects of permeable cylinder. During the experiments, the Reynolds number was about 6250 depending on the diameter of permeable cylinder. In order to explain the effect of the permeable cylinder, the time-averaged streamwise velocity, the time averaged patterns of streamlines and Reynolds shear stress contours are illustrated at this study. A result taken into consideration is that the occurrence of large-scale vortical structures is suppressed by permeable cylinders. The peak values of TKE and Reynolds shear stress decrease gradually with increasing of the porosity. When the results are evaluated in terms of the frequency of vortex shedding, any clear and distinct peak of frequency cannot be obtained at the downstream of the permeable cylinders as the natural frequency of vortex shedding is found to be f=0.73 for the bare cylinder case. The flow structures at the wake region of permeable cylinders having porosity values $\beta \geq 0.6$ are like a flow without an obstacle in the flow field. This means that occurrence of vortex shedding and energy transfer from the free stream region into the wake region are considerably prevented. Thus, the permeable cylinders having the porosities $\beta \geq 0.6$ would be used instead of the solid cylinders at the many engineering applications.

REFERENCES

Akansu, Y. E. and Fırat, E. (2010). "Control of flow around a square prism by slot jet injection from the rear surface." *Experimental Thermal and Fluid Science*, Vol. 34, No. 7, pp. 906-914.

Al-hajerı, M. H., Aroussi, A. and Witry, A. (2009). Numerical Simulation of Flow Past Multiple Porous Cylinders. *Journal of fluids engineering-transactions of the ASME*, Vol. 131, No. 7, 071101.

Corke, T. C., Enloe, C. L. and Wilkinson, S. P. (2010). Dielectric barrier discharge plasma actuators for flow control. Annual Review of Fluid Mechanics, Vol. 42, pp. 505-529.

Ekmekci, A and Rockwell, D. (2010). Effects of a geometrical surface disturbance on flow past a circular cylinder: a large-scale spanwise wire. *Journal of Fluid Mechanics*, Vol. 665, pp. 120-157.

Farhadi, M, Sedighi, K and Fattahi, E. (2010). Effect of a splitter plate on flow over a semi-circular cylinder. Proc. IMechE Part G: *J. Aerospace Engineering*, Vol. 224, pp. 321-330.

Feng, L-H and Wang, J. J. (2012). Synthetic jet control of separation in the flow over a circular cylinder. *Experiments in Fluids*, Vol. 53, pp. 467–480.

Fujısawa, N. and Takeda G. (2003). Flow Control Around a Circular Cylinder by Internal Acoustic Excitation. *Journal of Fluids and Structures*, Vol. 17, pp. 903– 913.

Gim, O. S., Kim, S. H. and Lee, G. W. (2011). Flow control behind a circular cylinder by control rods in uniform stream. *Ocean Engineering*, Vol. 38, No. 17-18, pp. 2171–2184.

Gozmen, B., Akilli, H. and Sahin, B. (2013). Passive control of circular cylinder wake in shallow flow. *Measurement*, Vol. 46, pp. 1125-1136.

Gozmen, B. and Akilli, H. (2014). Flow control downstream of a circular cylinder by a permeable cylinder in deep water. *Wind and Structures*, Vol. 19, No.4, pp. 389-404.

Hiejima, S., Kumao, T. and Taniguchi, T. (2005). Feedback control of vortex shedding around a bluff body by velocity excitation. *International Journal of Computational Fluid Dynamics*, Vol. 19, No. 1, pp. 87-92.

Li, Z., Navon, I. M., Hussaini, M. Y. and Le Dimet, F-X. (2003). Optimal control of cylinder wakes via suction and blowing. *Computers & Fluids*, Vol. 32, pp. 149–171.

Lim, H. C and Lee, S. J. (2003). PIV Measurements of near wake behind a U-grooved cylinder. *Journal of Fluids and Structures*, Vol. 18, No. 1, pp. 119-130.

Muddada, S. and Patnaik, B. S. V. (2010). An assessment of turbulence models for the prediction of flow past a circular cylinder with momentum injection. *Journal of Wind Engineering and Industrial Aerodynamics*, Vol. 98, pp. 575-591.

Nakamura, H and Igarshi, T. (2008). Omnidirectional reductions in drag and fluctuating forces for a circular cylinder by attaching rings. *Journal of Wind Engineering and Industrial Aerodynamics*, Vol. 96, pp. 887–899.

Ozkan, G. M., Oruc, V., Akilli, H. and Sahin, B. (2012). Flow around a cylinder surrounded by a permeable cylinder in shallow water. *Experiments in Fluids*, Vol. 53, No. 6, pp. 1751-1763.

Pinar, E., Ozkan, G. M., Durhasan, T., Aksoy, M. M., Akilli, H. and Sahin, B. (2015). Flow structure around perforated cylinders in shallow water. *Journal of Fluids and Structures*, Vol. 5, pp. 52–63.

Raffel, M., Willert, C. E. and Kompenhans, J. (1998) Particle Image Velocimetry a Practical Guide, Springer, Göttingen.

Sahın, B. and Ward-Smith A. J. (1987) The use of perforated plates to control the flow emerging from a wide-angle diffuser. *Heat and Fluid Flow*, Vol. 8, No. 2, pp. 124-131.

Sudhakar, Y. and Vengadesan, S. (2012). Vortex shedding characteristics of a circular cylinder with an oscillating wake splitter plate. *Computers & Fluids*, Vol. 53, pp. 40–52.

Turkish Journal of Engineering

Turkish Journal of Engineering (TUJE)
Vol. 2, Issue 2, pp. 60-72, May 2018
ISSN 2587-1366, Turkey
DOI: 10.31127/tuje.345153
Research Article

MODULAR APPROACH TO THE DESIGN OF PATH GENERATING PLANAR MECHANISMS

İskender Özkul [1] and Hüseyin Mutlu *[2]

[1] Mersin University, Engineering Faculty, Mechanical engineering Department, Mersin, Turkey
ORCID ID 0000-0003-4255-0564
iskender@mersin.edu.tr

[2] Mersin University, Engineering Faculty, Mechanical engineering Department, Mersin, Turkey
ORCID ID 0000-0002-4770-2873
hmutlu@mersin.edu.tr

* Corresponding Author
Received: 19/10/2017 Accepted: 14/12/2017

ABSTRACT
A novel approach, called modular approach, is presented in this paper making possible the closed-form solutions of the planar path-generating multi-link mechanisms with lower pairs. In this approach, the mechanism is viewed as a suitable combination of some simpler components called "modules". The design of the modules is realized by applying the so-called Precision-Point, Subdomain and Galerkin methods. The approach is illustrated on 4-bar, slider-crank, double-slider, 5-bar and 6-link mechanisms. Numerical results prove the effectiveness of the approach.

Keywords: *Mechanism, Path Generating, Multi-link*

1. INTRODUCTION

Analytical methods for synthesizing mechanisms can be classified mainly into two categories. One of them is the numerical iterative approach and the other is the closed form solution approach. Out of a desire to use high speed computing abilities of the computers, the tendency towards utilizing numerical iterative approach has usually been strong. For instance, Roth and Freudenstein (Roth *et al*. 1963) have applied the so called Newton Raphson method to solve the synthesis of geared five bar mechanism to pass through nine path points. Kramer and Sandor (Kramer *et al*. 1975) have referred to direct search techniques for minimizing a penalty function against violation of what they call "accuracy neighborhoods" around selected path points. A similar approach has been shown by Bakthavachalam and Kimbrell (Bakthavachalam *et al*. 1975) in path generation involving clearances and manufacturing tolerances. There are well-known limitations of the numerical iterative approaches. First of all, these methods are crippled by serious convergence difficulties. No assurance regarding the convergence of an arbitrary starting design to a final one exists. Thus, they highly depend upon the suitable selection of an initial solution. Although they require a large computation time, they finally provide one single solution. On the other hand, the closed form solution does not possess the aforementioned undesirable features associated with the numerical iterative techniques. However, one important drawback of the closed form solution is the fact that the number of parameters, which can be taken into account in the synthesis procedure, is generally very limited. This indicates that most mechanisms, especially those which are of multi-link structure, display a situation where closed-form approach is not directly applicable due to the abundant number of parameters. Nevertheless, if multi-link mechanisms can be decomposed into simpler components whereby closed form solution is possible, then the whole mechanism can be synthesized by bringing together in a suitable manner the design of simpler structural units called modules. This is the underlying idea behind this work. From this angle, the mechanisms are viewed as an appropriate combination of "modules". Thus, this approach is conveniently termed as a "modular approach".

This paper presents the application of this approach on the design of path generating planar mechanisms with lower pairs. Illustrations of the approach have been shown on four bars, slider crank, double slider, 5-bar and six link mechanisms. The applications have been put in the form of computer programs. The numerical results indicate that the approach is an effective and efficient one.

2. MODULES

Planar mechanisms with lower pairs can be thought of as being made up of simpler components, referred to as "modules" hereafter in this paper, whose motion relationships exhibit compact forms for handling the design equations within the framework of the closed form solution. Modules which compose most planar constrained mechanisms can be considered as three basic types; namely, a dyad, a crank rocker, and a slider. Dyad and crank rocker have the similar property involving two links connected by only revolute pairs in the plane. They basically differ from one another in that dyad can perform only partial rotation whereas a crank rocker module involves a full revolution. Thus, where a crank drive is needed, this module is supplemented to another assemblage of links supposed to generate a given path. Slider module consists of a prismatic pair connected to a link through a revolute pair. Now formulation and solution of the design equations governing each module have been developed as follows:

2.1. Dyad Module

Dyad, as shown in Fig.1, is a two-member assembly with two degrees of freedom. Its end point C is supposed to move on the given path y=f(x), x0≤x≤xn.. From the geometry of Fig.1, The following is written for the coordinate of point C within the reference frame xoy:

$$x = x_7 + x_1 \operatorname{Cos}\psi + d_{45} \operatorname{Cos}\delta \quad (1)$$

$$y = x_8 + x_1 \operatorname{Sin}\psi + d_{45} \operatorname{Sin}\delta \quad (2)$$

By eliminating angle δ from equations (1) and (2), the displacement function (G) governing the motion in the dyad is obtained as follows:

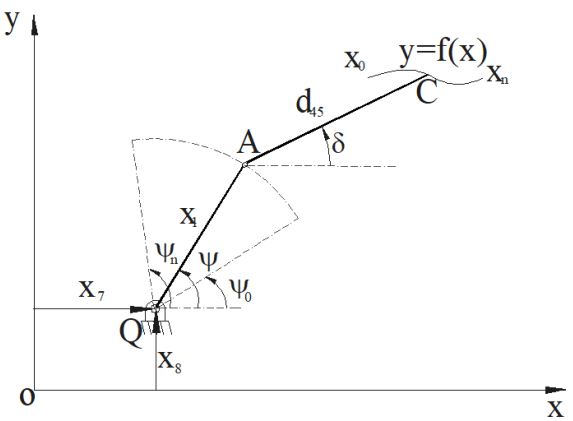

Fig. 1. Dyad Module

$$G(x_1, d_{45}, x_7, x_8, \psi_0, x, y) = x^2 + y^2 - 2xx_7 - 2yx_8 - x_1(x\cos\psi + y\sin\psi - x_7\cos\psi - x_8\sin\psi) + t_1 = 0 \quad (3)$$

$$t_1 = x_1^2 + x_7^2 + x_8^2 - d_{45}^2 \quad (4)$$

where $\psi = \psi_0 + h(x)$ and ψ'=h(x) represents the well-defined the motion of the arm QA against the independent variable x. As can be seen from equation (3), the number of available system parameters is five. Therefore, the number of design equations that can be written is limited by five.

The problem of formulating the design can be approached from three different points of view. In one of them, the displacement function is set equal to zero at a number of collocation points called precision or accuracy points. This approach referred to in the literature as Collocation, Precision or Accuracy point approach (F 1955; SH 1956; Kao *et al.* 2006), yields the following:

$$G(x_1, d_{45}, x_7, x_8, \psi_0, x_i, y_i) = 0; \quad i = 1,2,3,4,5 \quad (5)$$

where (xi,yi) defines the coordinates of the precision points.
Another point of view in formulating the design is to make the average of the displacement equation (G) zero over selected subintervals of the function interval (x_0,xn). The number of subintervals will be equal to the number of available system parameters. This constitutes the so called Subdomain method (F 1955; SH 1956; Hartenberg *et al.* 1964; Akcali *et al.* 1979; Akcali 1983; Akcali 1987; Akcali *et al.* 1989), which, in the case under consideration, leads to the following equation set:

$$\int_{x_{i-1}}^{x_i} G(x_1, d_{45}, x_7, x_8, \psi_0, x_i, y_i)dx = 0 \quad i = 1,2,3,4,5 \quad (6)$$

where (x_{i-1},x_i) are subintervals belonging to the interval (x0,xn).
The design of the dyad to generate the given path can also be formulated by making the displacement equation orthogonal to a set of weighting functions $W_i(x)$ defined on the same interval (x_0,x_n) as the given path y(x). The number of weighting functions will be equal to that of the parameters, thus leading to the following design equations; in accordance with the so-called Galerkin method (SH 1956; Akcali 1987):

$$\int_{x_0}^{x_n} G(x_1, d_{45}, x_7, x_8, \psi_0, x, y)W_i dx = 0; \quad i = 1,2,3,4,5 \quad (7)$$

Now all the design equations resulting from Precision point, Subdomain and Galerkin methods can be represented by the following set:

$$A_i - B_i x_7 - C_i x_8 - D_i x_1 + F_i t_1 = 0; \; i = 1,2,3,4,5 \quad (8)$$

where:

$$D_i = V_{ci}\cos\psi_0 + V_{si}\sin\psi_0 - D_{ci}x_7\cos\psi_0 + D_{si}x_7\sin\psi_0 - D_{ci}x_8\sin\psi_0 - D_{si}x_8\cos\psi_0; \; i = 1,2,3,4,5 \quad (9)$$

The coefficients A_i,B_i,C_i,F_i,V_{ci},V_{si},D_{ci},D_{si} are calculated according to each method as follows:
In Precision-Point approach:

$$A_i = x_i^2 + y_i^2; B_i = 2x_i; C_i = 2y_i; F_i = 1; V_{ci} = 2(x_i\cos\psi' + y_i\sin\psi'); \; i = 1,2,3,4,5$$
$$V_{si} = 2(-x_i\sin\psi' + y_i\cos\psi'); D_{ci} = 2\cos\psi'; D_{si} = 2\sin\psi'; \quad (10)$$

In Subdomain method:

$$A_i = \int_{x_{i-1}}^{x_i}(x^2 + y^2)dx; \; B_i = 2\int_{x_{i-1}}^{x_i} xdx; \; C_i = 2\int_{x_{i-1}}^{x_i} ydx; \; F_i = \int_{x_{i-1}}^{x_i} dx; \; V_{ci} = 2\int_{x_{i-1}}^{x_i}(x\cos\psi' + y\sin\psi')dx;$$
$$V_{si} = 2\int_{x_{i-1}}^{x_i}(-x\sin\psi' + y\cos\psi')dx; \; D_{ci} = 2\int_{x_{i-1}}^{x_i}\cos\psi' dx; \; D_{si} = 2\int_{x_{i-1}}^{x_i}\sin\psi' dx; \; i = 1,2,3,4,5 \quad (11)$$

In Galerkin methods:

$$A_i = \int_{x_0}^{x_n}(x^2 + y^2)W_i dx; B_i = 2\int_{x_0}^{x_n} xW_i\, dx; C_i = 2\int_{x_0}^{x_n} yW_i\, dx; F_i = \int_{x_0}^{x_n} W_i dx; V_{ci} = 2\int_{x_0}^{x_n}(x\cos\psi' + y\sin\psi')W_i dx;$$
$$V_{si} = 2\int_{x_0}^{x_n}(-x\sin\psi' + y\cos\psi')W_i\, dx; D_{ci} = 2\int_{x_0}^{x_n}\cos\psi' W_i\, dx; D_{si} = 2\int_{x_0}^{x_n}\sin\psi' W_i\, dx; i = 1,2,3,4,5 \quad (12)$$

In order to solve equation set (8), first t1 and x1 and then ψ_0 are eliminated, thus reducing the set to the following form:

$$E_{1k}x_7^4+(E_{2k}x_8+E_{3k})x_7^3+(E_{4k}x_8^2+E_{5k}x_8+E_{6k})x_7^2+(E_{7k}x_8^3+E_{8k}x_8^2+E_{9k}x_8+E_{10k})x_7 \\ +(E_{11k}x_8^4+E_{12k}x_8^3+E_{13k}x_8^2+E_{14k}x_8+E_{15k})=0 \quad ;k=1,2 \tag{13}$$

where (E_{jk} ,j=1,..,15,k=1,2) are constants. The solution of (13) is realized for all possible sets of (x_7,x_8) by first eliminating the term x_7^4 from the set and drawing x_7 from the resultant equation to be substituted back into one of the equations. Based on the solutions of (13) for x_7,x_8 , it is now a simple matter to solve for the rest of the unknowns, namely, ψ_0 , x_1 and d_{45}.

The resulting dyad designs can be analyzed first by solving δ from eq'n (1) for a given value of x_{th} , then substituting it in eq'n (2) to determine y_{ac} with the purpose of computing structural error $e=y(x_{th})-y_{ac}$.

2.2. Slider Module

One of the lower pairs to be found in planar mechanisms is the sliding or prismatic pair. Thus, in order to accomplish the designs of planar mechanisms involving prismatic pairs, development of the design scheme of a new type of module, referred to as the slider module here, is needed.

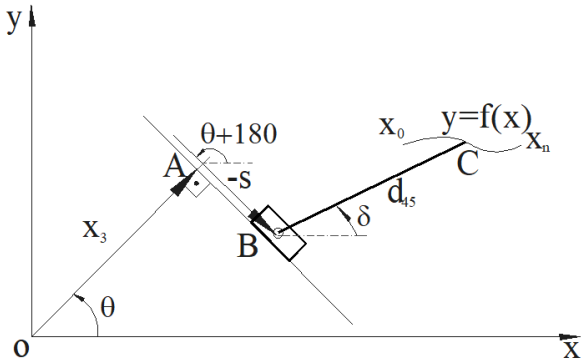

Fig. 2. Slider Module

The problem to be formulated here is to find the suitable dimensions of the slider module shown in Fig.2 such that a point (C) on the floating link BC trace the given curve y=f(x) $x_0 \le x \le x_n$ as close as possible, while the sliding link moves along a line between points characterized by s_0 and s_n

Writing out the x and y co-ordinate of the floating-point C of the module in terms of the variables and parameters shown in Fig.2 and then eliminating the angle δ from the two equations will yield the displacement function (H) of the slider module:

$$H(\theta,s_0,d_{45},x_3,x,y)=x^2+y^2+s'^2-x_3(2xC\cos\theta+2yS\sin\theta)+(s'+s_0)(2xS\sin\theta-2yC\cos\theta)+2s_0s'+P=0 \tag{14}$$

where:

$$P=x_3^2+s_0^2-d_{45}^2 \tag{15}$$

Here, it is assumed the motion ($s'=s-s_0$) of the slider is defined in the form of specified g(x) functional relationship against x. An examination of Fig.2 as well as of equation (14) will explain that there are four unknown parameters, namely, (θ,s_0,d_{45},x_3) and thus treatment of the displacement function according to the requirements of the Precision-Point, Subdomain and Galerkin methods will yield four design equations in the following form:

$$k_{ai}+2k_{ei}s_0+k_{di}P-x_3(k_{bi}\mathrm{Cos}\,\theta+k_{ci}\mathrm{Sin}\,\theta)+(s_0+k_{ei})(k_{bi}\mathrm{Sin}\,\theta-k_{ci}\mathrm{Cos}\,\theta)=0;\ i=1,2,3,4 \tag{16}$$

where coefficients in equations (16) are defined according to each method as follows:
In Precision-Point method:

$$k_{ai}=x_i^2+y_i^2+s'^2_i;\ k_{bi}=2x_i;\ k_{ci}=2y_i;\ k_{di}=1;\ k_{ei}=s'_i;\ i=1,2,3,4 \tag{17}$$

In Subdomain method:

$$k_{ai}=\int_{x_{i-1}}^{x_i}(x^2+y^2+s'^2)dx;\ k_{bi}=2\int_{x_{i-1}}^{x_i}x\,dx;\ k_{ci}=2\int_{x_{i-1}}^{x_i}y\,dx;\ k_{di}=\int_{x_{i-1}}^{x_i}dx;\ k_{ei}=\int_{x_{i-1}}^{x_i}s'dx;\ i=1,2,3,4 \tag{18}$$

In Galerkin method:

$$k_{ai}=\int_{x_0}^{x_n}(x^2+y^2+s'^2)W_i\,dx;\ k_{bi}=2\int_{x_0}^{x_n}xW_i\,dx;\ k_{ci}=2\int_{x_0}^{x_n}yW_i\,dx;\ k_{di}=\int_{x_0}^{x_n}W_i dx;\ k_{ei}=\int_{x_0}^{x_n}s'W_i\,dx;\ i=1,2,3,4 \tag{19}$$

For the solution of the set (16), first P then x_3 and s_0 are eliminated leaving the final equation in one single unknown (θ):

$$l_1\cos^3\theta+l_2\sin^3\theta+l_3\cos^2\theta+l_4\sin^2\theta+l_5\cos\theta+l_6\sin\theta+l_7\cos^2\theta\sin\theta+l_8\sin^2\theta\cos\theta+ l_9\cos\theta\sin\theta+l_{10}=0 \tag{20}$$

After solving the equation (20) for θ between 0 and 2π, it is not difficult to determine the other unknowns (s_0,d_{45},x_3) from equation set (16), thus completing the design of the slider module.
The motion analysis of the resulting module design can be performed first by computing the floating link angle (δ) from the abscissa ($x=x_{th}$) expression to be inserted into the ordinate (y_{ac}) expression for the evaluation of structural error, $e=y(x_{th})-y_{ac}$.

2.3. Crank-rocker Module

In the resulting path-generating mechanisms, usually the coupler point is required to trace only a portion of a closed curve very nearly and there is no guarantee that a member of the resulting mechanism will make a full revolution, a necessary condition for bringing the whole assembly in motion by means of a rotary actuator. In that case, there arises the need to add the crank-rocker module to the path-generating assembly in order to operate the system. Frictionless engine, grass-cutter and oil pump drivers, (Dittrich *et al.* 1978) can be cited as well-known examples in this regard.

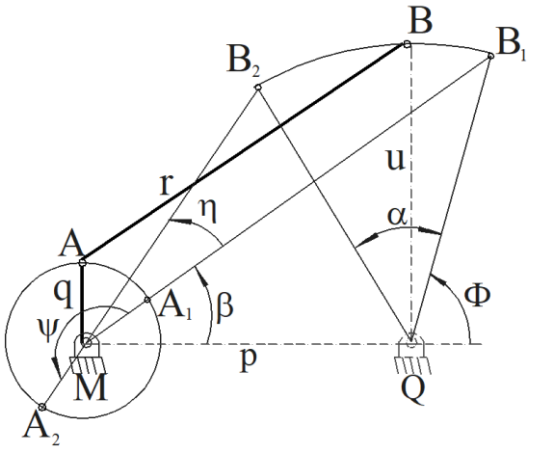

Fig. 3. Crank-rocker module

Crank-rocker module is, in fact, a dyad, Fig.3, with the difference that the crank MA rotates 360° degrees while the endpoint (B) of the floating link BA is constrained to move on a circular path with center at Q and radius BQ. In designing the crank-rocker module, it is a fundamental condition that the assembly assumes the limiting configurations shown in Fig.3. Sine Law is written for triangles ΔMB_1Q and ΔMB_2Q in Fig.3. Then supposing that rocker swing angle (α), time ratio (t_R) or angle between dead-centers (η) and initial crank angle (β) are specified, the following relations are deduced to determine the relative dimensions (p,q,r,u) of the crank-rocker module:

$$\frac{u}{p}=\frac{Sin\beta}{Sin(\Phi-\beta)};\frac{r}{p}=\frac{1}{2}\left[\frac{\sin\Phi}{\sin(\Phi-\beta)}+\frac{\sin\Phi+\alpha}{\sin(\Phi+\alpha-\beta-\eta)}\right]$$
$$\frac{q}{p}=\frac{1}{2}\left[\frac{\sin\Phi}{\sin(\Phi-\beta)}-\frac{\sin\Phi+\alpha}{\sin(\Phi+\alpha-\beta-\eta)}\right] \tag{21}$$
$$with\ \ \Phi=\tan^{-1}\left[\tan\beta\frac{\sin(\beta+\eta)+\sin(\alpha-\beta-\eta)}{\sin(\beta+\eta)-\tan\beta\cos(\alpha-\beta-\eta)}\right]$$

Depending on the design situation, several specifications from among the parameters defined on Fig.3, namely, (p,q,r,u,α,β,η,Φ), equation set (21) may be rearranged with respect to the given situation. Thus, in this way module design can be adapted to the designer's needs and conditions.

3. CIRCLE AND LINE POINTS OF A GENERAL COUPLER PLANE

In order to transform modules into mechanisms those points of the coupler plane which lie on a circle and those on a line should be searched, consistent with the modules developed previously. Firstly, the case of circle-points will be handled. Referring to Fig.4, point D of the plane is required to follow a circular path as point C of the same plane traces the given path $y=f(x)$ $x_0 \le x \le x_n$. The co-ordinates (x,y) of the point is written parametrically relative to A in terms of in the same variable (t) xoy-system of Fig.4:

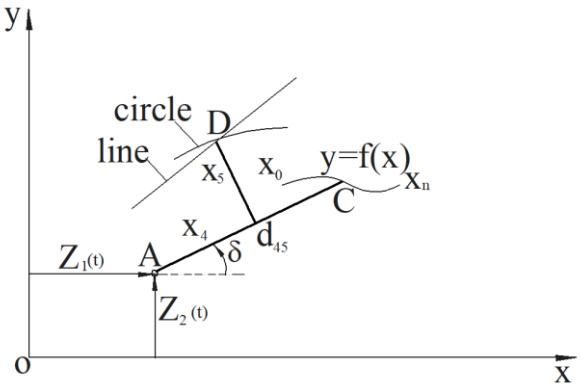

Fig. 4. General coupler motion

$$x = Z_1(t) + k_1 x_4 - k_2 x_5 \tag{22}$$

$$y = Z_2(t) + k_2 x_4 + k_1 x_5 \tag{23}$$

$$k_1 = Cos\delta(t) \quad ; \quad k_2 = Sin\delta(t) \tag{24}$$

For D to be on the circle, the following should be satisfied:

$$(x - x_m)^2 + (y - y_m)^2 = R^2 \tag{25}$$

Substituting (22), (23) in (25) and arranging yields the displacement function F as follows:

$$F(x_4, x_5, x_m, y_m, R, t) = P_1 - 2k_1 x_m x_4 + 2k_2 x_m x_5 - 2k_2 y_m x_4 - 2k_1 y_m x_5 + 2(Z_1 k_1 + Z_2 k_2)x_5 - 2(Z_1 k_2 - Z_2 k_1)x_5 - 2Z_1 x_m - 2Z_2 y_m + Z_1^2 + Z_2^2 = 0; \tag{26}$$

where $P_1 = x_4^2 + x_5^2 + x_m^2 + y_m^2 - R^2$

Applying Precision-Point, Subdomain and Galerkin methods on function F, the following equation set will result:

$$U_i P_1 - Z_{ai} x_m x_4 + Z_{bi} x_m x_5 - Z_{bi} y_m x_4 - Z_{ai} y_m x_5 + Z_{ci} x_4 - Z_{di} x_5 - Z_{ei} x_m + Z_{fi} y_m + Z_{gi} = 0; \; i = 1,2,3,4,5 \tag{27}$$

The coefficients in the set (27) are defined according to each method as follows:

In Precision-Point method:

$$Z_{ai} = 2k_{1i}; \; Z_{bi} = 2k_{2i}; \; Z_{ci} = 2(Z_{1i} + Z_{2i}k_{2i}); \; Z_{di} = 2(Z_{1i}k_{2i} - Z_{2i}k_{1i}); \; Z_{ei} = 2Z_{1i}; \; Z_{fi} = 2Z_{2i}; \; Z_{gi} = Z_{1i}^2 + Z_{2i}^2; \; U_i = 1; \; i = 1,2,3,4,5 \tag{28}$$

In Subdomain method:

$$Z_{ai} = 2\int_{t_{i-1}}^{t_i} k_1 dt; \; Z_{bi} = 2\int_{t_{i-1}}^{t_i} k_2 dt; \; Z_{ci} = 2\int_{t_{i-1}}^{t_i} (Z_1 k_1 + Z_2 k_2)dt; \; Z_{di} = 2\int_{t_{i-1}}^{t_i} (Z_1 k_2 - Z_2 k_1)dt; \; Z_{ei} = 2\int_{t_{i-1}}^{t_i} Z_1 dt; \; Z_{fi} = 2\int_{t_{i-1}}^{t_i} Z_2 dt; \; Z_{gi} = \int_{t_{i-1}}^{t_i} (Z_1^2 + Z_2^2)dt; \; U_i = \int_{t_{i-1}}^{t_i} dt; \; i = 1,2,3,4,5 \tag{29}$$

In Galerkin method:

$$Z_{ai} = 2\int_{t_0}^{t_n} k_1 W_i dt; \; Z_{bi} = 2\int_{t_0}^{t_n} k_2 W_i dt; \; Z_{ci} = 2\int_{t_0}^{t_n} (Z_1 k_1 + Z_2 k_2) W_i dt; \; Z_{di} = 2\int_{t_0}^{t_n} (Z_1 k_2 - Z_2 k_1) W_i dt; \; Z_{ei} = 2\int_{t_0}^{t_n} Z_1 W_i dt; \; Z_{fi} = 2\int_{t_0}^{t_n} Z_2 W_i dt; \; Z_{gi} = \int_{t_0}^{t_n} (Z_1^2 + Z_2^2) W_i dt; \; U_i = \int_{t_0}^{t_n} W_i dt; \quad i = 1,2,3,4,5 \tag{30}$$

After eliminating parameters P_1, x_m and y_m in (27), equations containing only unknowns x_4 and x_5 are obtained:

$$L_{mi}x_4^3 + (K_{mi}x_5 + H_{mi})x_4^2 + (G_{mi}x_5^2 + F_{mi}x_5 + E_{mi})x_4 + (D_{mi}x_5^3 + C_{mi}x_5^2 + B_{mi}x_5 + A_{mi}) = 0 \; ; i = 1,2 \tag{31}$$

Coefficients L_{mi},K_{mi},H_{mi},G_{mi},F_{mi},E_{mi},D_{mi},C_{mi},B_{mi} and A_{mi} (i=1,2) are all computable constants. In solving (31) the cubic terms of x_4 are eliminated and the resulting single quadratic equation can be used to express x_4 as a function of x_5, which is then substituted in one of (31) to yield all possible solutions.
In the case of line points of the coupler plane, point D in Fig.4 is to satisfy the equation of a line in the form:

$$y = mx + n \tag{32}$$

In (32) (m) is the slope and n is the intercept of the line. Then the following displacement function Q involving the system parameters (x_4,x_5,m,n) will result as such:

$$Q(x_4, x_5, m, n, t) = k_2x_4 + k_1x_5 - k_1mx_4 + k_2mx_5 - Z_1m + Z_2 - n = 0 \tag{33}$$

If the function Q is evaluated under the criteria of Precision-Point, Subdomain and Galerkin methods, then the following equation set is found:

$$h_{ai}x_4 + h_{bi}x_5 - h_{bi}mx_4 + h_{ai}mx_5 - h_{ci}m - h_{di}n + h_{ei} = 0 \;\; ; i = 1,2,3,4 \tag{34}$$

The coefficients in (34) are calculated according to each method in question as follows:
In Precision-point method:

$$h_{ai} = k_{2i} \; ; h_{bi} = k_{1i} \; ; h_{ci} = Z_{1i} \; ; h_{di} = 1 \; ; h_{ei} = Z_{2i} \; ; \;\; i = 1,2,3,4 \tag{35}$$

In Subdomain method:

$$h_{ai} = \int_{t_{i-1}}^{t_i} k_2 dt \; ; h_{bi} = \int_{t_{i-1}}^{t_i} k_1 dt \; ; h_{ci} = \int_{t_{i-1}}^{t_i} Z_1 dt \; ; h_{di} = \int_{t_{i-1}}^{t_i} dt \; ; h_{ei} = \int_{t_{i-1}}^{t_i} Z_2 dt; i = 1,2,3,4 \tag{36}$$

In Galerkin method:

$$h_{ai} = \int_{t_0}^{t_n} k_2 W_i dt \; ; h_{bi} = \int_{t_0}^{t_n} k_1 W_i dt \; ; h_{ci} = \int_{t_0}^{t_n} Z_1 W_i dt \; ; h_{di} = \int_{t_0}^{t_n} W_i dt \; ; h_{ei} = \int_{t_0}^{t_n} Z_2 W_i dt; \quad i = 1,2,3,4 \tag{37}$$

(34) can be reduced to a single equation in the unknown (m):

$$S_{A5}m^4 + S_{A4}m^3 + S_{A3}m^2 + S_{A2}m + S_{A1} = 0 \tag{38}$$

S_{A1} to S_{A5} are simply constants. After determining m from (38) all possible solution of the unknown set (x_4,x_5,m,n) is easily drawn from (34).

3.1. Application to Coupler Plane of Modules

Now the theory developed for a general coupler plane motion will be applied to modules. In doing so, it is sufficient to specify the co-ordinates Z_1,Z_2 and angle δ as a function of some variable t. First the dyad module will be considered. Referring to Fig.5, Z_1,Z_2 co-ordinates which will be substituted in equation sets (27) and (34) will be represented in terms of the input angle ψ, as follows:

$$Z_1 = x_7 + x_1 \operatorname{Cos}\psi$$

(39)

$$Z_2 = x_8 + x_1 \operatorname{Sin}\psi \tag{40}$$

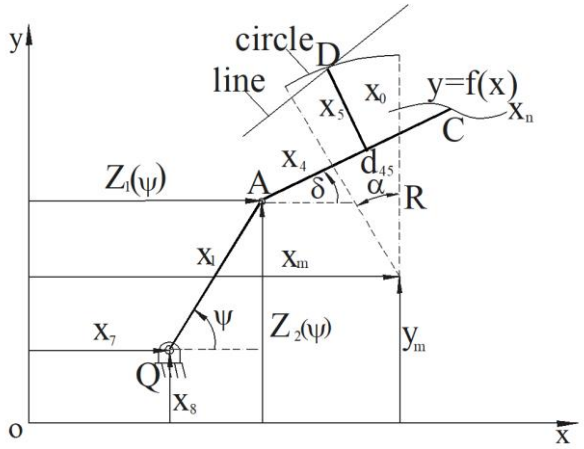

Fig. 5. Coupler motion of dyad module

Additionally, coupler angle δ will be determined as a function of ψ from relations (1),(2) after realizing the inverse transformation $x_{th}=h^{-1}(\psi-\psi_0)$. Knowing δ, k_1 and k_2 can be calculated from relation (24). Thus circle points of the dyad coupler are now found out by evaluating equation set (27) to lead to the values of the unknown parameters (x_4,x_5,R,x_m,y_m). Similarly, (x_4, x_5, m, n) parameters are obtained by solving equation set (34) for the line points of the dyad coupler.

In the case of slider module, Fig.6, Z_1, Z_2 co-ordinate functions are expressed as a function of the linear variable s, as given below:

$$Z_1 = x_3 \operatorname{Cos}\theta - s \operatorname{Sin}\theta \tag{41}$$

$$Z_2 = x_3 \operatorname{Sin}\theta + s \operatorname{Cos}\theta \tag{42}$$

Coupler angle δ is computed together with the inverse transformation $x_{th}=g^{-1}(s-s_0)$. Then the rest of the procedure is identical with that of the dyad module, thus defining the circle and line points of the slider coupler.

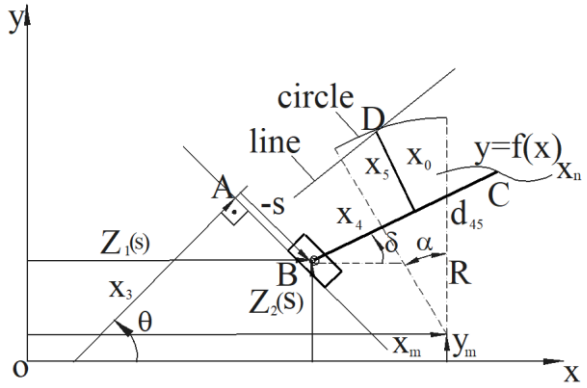

Fig. 6. Coupler motion of slider module

4. CONSTRUCTION OF MECHANISMS VIA MODULAR APPROACH

Four-bar and slider-crank mechanisms which are constructed using modular approach are shown in Fig 7(a),(b). In designing the 4-bar, first, the dyad module to generate the curve y=f(x) $x_0 \le x \le x_n$ at point C is synthesized as explained earlier, indicating that (x_7,x_8,x_1,ψ_0,d_{45}) are found out.

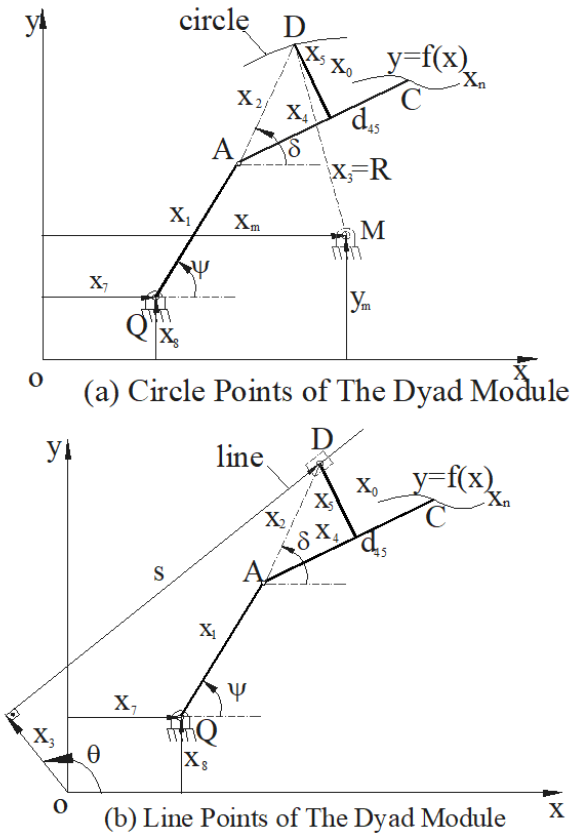

Fig. 7. Module coupler points

Then, circle points of the dyad coupler are determined, which are characterized by the parameter set (x_4,x_5,x_m,y_m,R), Fig.7(a). Now the circle point D is joined physically by the center point M, the relative location of which is defined by x_6 and x_9, by a link of length x_3=R, completing the construction of the four-bar QADM generating the given path at point C, where the connecting link length (x_2) is defined by AD=$(x_4^2+x_5^2)^{1/2}$. In order to estimate the quality of the designed 4-bar, the structural error (e) has to be calculated. To that end, the coupler angle (δ) in the resulting 4-bar is computed in accordance with the following relation:

$$\delta_{\mp} = 2\tan^{-1}\left[\frac{M_c \mp \sqrt{M_c^2 + L_c^2 - N_c^2}}{L_c + N_c}\right] \tag{43}$$

where

$$L_c = 2(x_1\cos\psi - x_6)x_2\ ;\ M_c = 2(x_1\sin\psi - x_9)x_2\ ;$$
$$N_c = x_3^2 - [x_1^2 + x_6^2 + x_9^2 + x_2^2 - 2x_1(x_6\cos\psi + x_9\sin\psi)] \tag{44}$$

Of the same dyad module (QAC) utilized in 4-bar design, line points (D) are determined to signify the estimation of the parameter set (x_4,x_5,m,n), Fig. 7(b). A slider is inserted at point D, which is then joined to point A of the dyad module, thus forming the slider-crank mechanism (QAD), Fig.7(b). For the structural error (e) analysis in the resulting slider-crank mechanism, connecting link angle (δ) is to be found by the following relation:

$$\delta_{\mp} = 2\tan^{-1}\left[\frac{M_s \mp \sqrt{M_s^2 + L_s^2 - N_s^2}}{L_s + N_s}\right] \tag{45}$$

where

$$L_s = x_2\cos\theta\ ;\ M_s = x_2\sin\theta\ ;\ N_s = x_3 - x_1(\cos\theta\cos\psi + \sin\theta\sin\psi) \tag{46}$$

Now the modular approach will be applied to design a path-generating double-slider. First, a slider-module is synthesized by means of the parameter set (θ,s_0,d_{45},x_3) to trace a given path at point C, Fig. 8. Then line points of the slider coupler are

searched to conclude on the values of the parameter set (x_4, x_5,m,n). Now placing sliders at points D and B, and joining them together physically to obtain a length of $x_2=(x_4^2+x_5^2)^{1/2}$ will produce the double slider with determinate movement directions, to generate the given path. In the structural error analysis of the resulting mechanism, the angular position of the connecting link will be needed, which is simply as follows:

$$\delta_{\mp} = 2\tan^{-1}\left[\frac{M_d \mp \sqrt{M_d^2 + L_d^2 - N_d^2}}{L_d + N_d}\right] \tag{47}$$

where

$$L_d = \frac{x_2}{Sin\theta'}; \quad M_d = \frac{x_2}{Cos\theta'}$$

$$N_d = \frac{1}{Sin\theta' Cos\theta'}\left[x_3' - x_3(Cos\theta Cos\theta' + Sin\theta Sin\theta') + s(Sin\theta Cos\theta' - Cos\theta Sin\theta')\right] \tag{48}$$

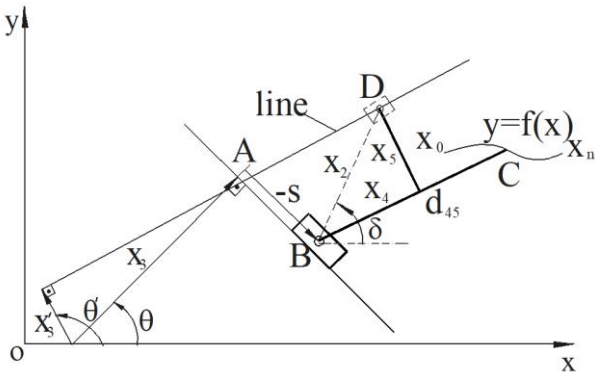

Fig. 8. Line points of the slider module

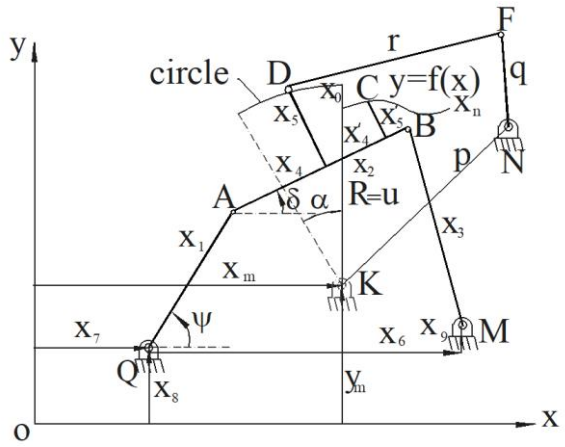

Fig. 9. Construction of a Six Bar Mechanism

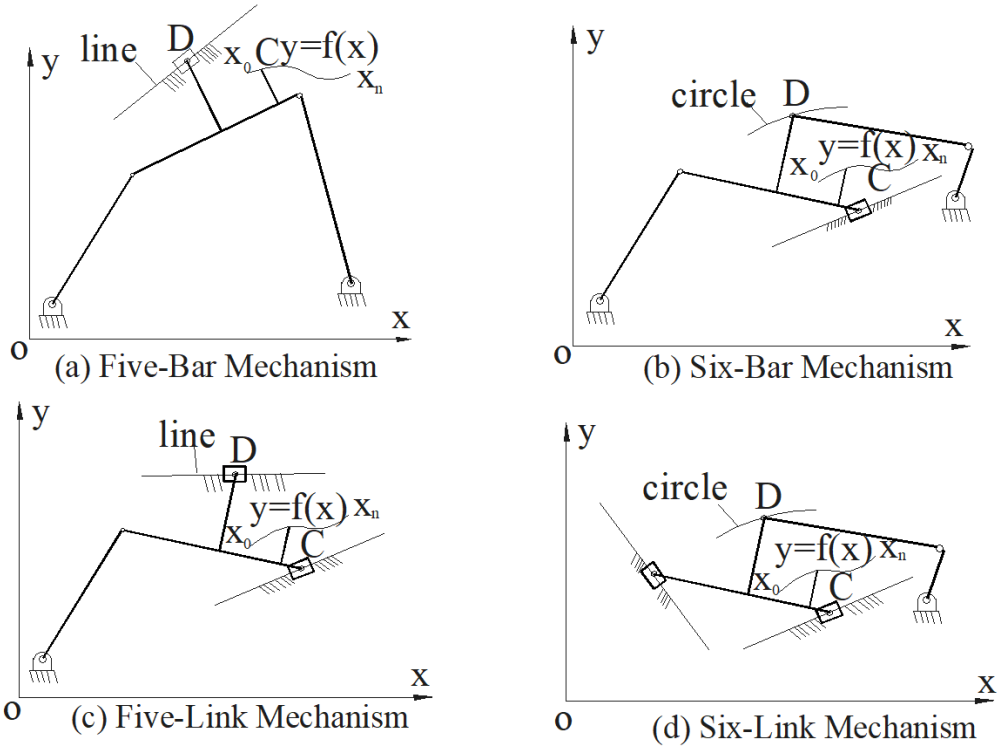

Fig. 10. Applications of the modular approach

The modular approach will be illustrated further on a six-bar mechanism, taking into account the four-bar and the crank-rocker module. To this end, the four-bar shown in Fig.9, characterized by the parameter set (x_7,x_8,ψ_0,x_2,x_3,x_6,x_9,x_4',x_5') is synthesized through the modular approach as described earlier, in the first place. Later the circle points of the coupler plane of the designed four-bar QABM generating the given path at point C, are searched. This establishes the values of the parameter set (x_4,x_5,x_m,y_m,R) associated with the circle point D, the center of which is located at point K, Fig.9. In this way, the length of the circular arc becomes known hence the angle (α) from the center K. Now using the outcome concerning the rocker swing angle (α) and rocker length (u) being equal to the radius of the circle (R), and also assuming one other criterion such as time ratio (t_R) ar angle (η) or initial crank angle (β), crank-rocker module is designed, based on the equation set (21). It should be pointed out that K is an imaginary joint and DK is an imaginary link whereas D,F and N signify physically existent revolute joints, and DF,FN physical links. This concludes the design of the whole six-bar mechanism QADBFN, in Fig. 9, such that the given path is generated as the crank FN drives the system through 360° rotations.

The modular approach explained in detail on specific examples can be easily applied to many other lower-paired mechanisms, some of which are shown in Fig.10. For instance, in Fig.10 (a), the line points of the four-bar coupler plane can be evaluated by inserting a linear slider, forming a five-bar to generate the specified path. Similarly, this technique can be utilized in designing the six-link mechanism seen on Fig.10 (b), which is constructed from circle-points of the slider-crank coupler plane together with a crank-rocker module. An extension of the line-points of the slider-crank coupler plane covers the five-link mechanism, whereby a linear slider is attached, Fig.10 (c). One final example may be given for the case, where circle-points of the double-slider can be assessed as a joint for combining it with a crank-rocker module, thus leading to a 6-bar mechanism which can be driven by a rotary power source, Fig.10(d).

5. Numerical Results and Discussion

The modular approach developed here has been put in the form of program packages on the personal computer for numerical applications. Wherever numerical integration is needed, for instance in Subdomain and Galerkin methods, the so-called Simpson's rule is used. To test the approach, the following specific examples have been taken as a basis for assessment. Although all possible solutions in each example have been obtained, only one typical solution is included here.

Example 1: A dyad module is to be designed to generate the path y=x $0 \le x \le 1$ for a 90 degree clockwise crank rotation. Some numerical results, with reference to the previous notation, are given according to each method as follows:

In Precision-point method: Precision points(x(i),i=1,..,5)=0.00,0.20,0.70,0.80,1.00;
Solution: x_1=0.4645; x_7=3.0064; x_8=-2.0064;d_{45}=4.0091;ψ_0= 0.0000°; e_{max}=0.000005;
In Subdomain method: Subdomains(x(i),i=1,..,6)=0.00,0.01,0.40,0.60,0.99,1.00;
Solution: x_1=0.4636; x_7=3.0089; x_8=-2.0089; d_{45}=4.01180;ψ_0= 0.00°;e_{max}=0.000005;
In Galerkin method: Weighting function(W_i,i=1,5)= $x, 2x^2 - 1, x^3 - 1, 8x^4 - 8x^2 + 1, 16x^5 - 20x^3 + 5x$

Solution: x_1=0.4642; x_7=3.0074; x_8=-2.0074;d_{45}=4.0101;ψ_0= 0.00°;e_{max}=0.000004;

Example 2: A slider module is to be synthesized for generating the path y=x 0≤x≤1 within one unit of slider displacement. The resulting solutions and the corresponding data are as follows:
In Precision-point method: Precision points(x(i),i=1,..,4)=0.00,0.50,0.80,1.00;
Solution: d_{45}=0.8073; x_3=-0.1105; θ=-22.92°;s_0=0.7997;e_{max}=0.003813;
In Subdomain method: Subdomains(x(i),i=1,..,5)=0,0.20,0.5,0.80,1.00;
Solution: d_{45}=0.6890; x_3=-0.1888; θ=-27.45°;s_0=0.6647;e_{max}=0.003626;
In Galerkin method : Weighting function(W_i,i=1,4) $x, 2x^2 - 1, 4x^3 - 3x, 8x^4 - 8x^2 + 1$
Solution: d_{45}=0.7108; x_3=-0.1678; θ=-26.38°;s_0=0.6931;e_{max}=0.002515;

Example 3: A four-bar design is to be obtained such that the coupler point trace the path y=x 0≤x≤1 within 90 degrees clockwise crank rotation. In the solution, the circle points of the dyad coupler of Example 1 are referred to, thus leading to the numerical results given below in accordance with each method.
In Precision-point method: Precision points(ψ_p(i),i=1,..,5)=0.00°,-0.10°,-0.20°,-0.30°,-90.00°
Solution:
x_1=0.4642;x_2=3.0468;x_3=2.8626;x_4=2.0164;x_5=3.4662;x_6=-0.7778;x_7=3.0074;
x_8=-2.0074;x_9=0.6015;ψ_0=0.00°;e_{max}=0.0002682;
In Subdomain method: Subdomains (ψ_s(i),i=1,..,6)=0.00°,-0.10°,-0.20°,-0.30°,-89.00°,-90.00°;
Solution:
x_1=0.4642;x_2=4.9697;x_3=4.8188;x_4=1.1231;x_5=3.8496;x_6=-0.6695;x_7=3.0074;
x_8=-2.0074;x_9=0.4636;ψ_0=0.00°;e_{max}=0.000268;
In Galerkin method: Weighting function(W_i,i=1,5) $1, \sin\psi, \cos\psi, \sin^2\psi, \cos^2\psi$
Solution:
x_1=0.4642;x_2=1.4668;x_3=0.6528;x_4=3.5875;x_5=1.7919;x_6=-0.6340;x_7=3.0074;
x_8=-2.0074;x_9=0.6341;ψ_0=0.00°;e_{max}=0.000863;

Example 4: A slider-crank is required to generate the path y=x 0≤x≤1 for a 90 degree clockwise input rotation. In solving this problem, the line points of the dyad coupler of Example 1 are searched, producing the following results by each method.
In Precision-point method: Precision points(ψ_p(i),i=1,..,4)=0°,-50°,-65°,-90°;
Solution:
x_1=0.4642;x_2=1.7442;x_3=1.1094;x_4=3.4259;x_5=-2.0843;x_7=3.0074;
x_8=-2.0074;θ=-148.48°;ψ_0=0°;e_{max}=0.010061;

In Subdomain method: Subdomains (ψ_s(i),i=1,..,5)= 0°,-10°,-55°,-75°,-90°;
Solution:
x_1=0.4642;x_2=1.8768;x_3=1.2711;x_4=3.3144;x_5=-2.2573;x_7=3.0074;
x_8=-2.0074;θ=-148.56°;ψ_0=0°;e_{max}=0.009973;

In Galerkin method: Weighting function(W_i,i=1,4) $e^{\psi}, \sin\psi\cos\psi, \cos\psi, \sin\psi$
Solution:
x_1=0.4642;x_2=2.7238;x_3=2.2345;x_4=3.4925;x_5=-1.9707;x_7=3.0074;
x_8=-2.0074;θ=-173.45°;ψ_0=0°;e_{max}=0.0074223;

Example 5: A double-slider is sought for the generation of the path y=x 0≤x≤1 for a unit input displacement. The line points of the slider module of Example 2 will be the answer of this problem, in the following form:
In Precision-point method: Precision points (x_p(i),i=1,..,4)=0,0.01,0.011,1;
Solution: x_2=1.3435; x_4=-0.3300; x_5=0.66243; x_3=-0.1679; x_3'=0.4767; θ=-26.38°; θ'=-43.61°; s_0=0.6932; e_{max}=0.003176;
In Subdomain method: Subdomains (x_s(i),i=1,..,5)=0,0.01,0.011,0.012,1;
Solution: x_2=1.4220; x_4=-0.4453; x_5=0.5540; x_3=-0.1679; x_3'=0.6404; θ=-26.38°; θ'=-40.99°; s_0=0.6932; e_{max}=0.042500;
In Galerkin method: Weighting function(W_i,i=1,4)= $x - e^{-x^2}, x - e^{-x^3}, x - e^{-x^4}, x - e^{-x^5}$
Solution: x_2=0.9093; x_4=-0.5209; x_5=0.4837; x_3=-0.1679; x_3'=0.3652; θ=-26.38°; θ'=177.49°; s_0=0.6932; e_{max}=0.015030;

Example 6: A slider-crank is constructed by slider module that generate the path y=x 0≤x≤1 for a unit input displacement .The circle points of the slider module of Example 2 will be the answer of this problem, in the following form:
In Precision-point method: Precision points (x_p(i),i=1,..,4)=0,0.01,0.03,0.999,1;
Solution: x_1=0.7965; x_2=1.2373; x_4=1.6724; x_5=-0.5621; x_3=0.5134; x_7=0.1476; x_8 =1.8308;
θ=-26.38°; s_0=0.6932; e_{max}=0.008103;
In Subdomain method: Subdomains (x_s(i),i=1,..,5)=0,0.01,0.05,0.994,0.996,1;
Solution: x_1=1.1690; x_2=1.2288; x_4=1.6670; x_5=-0.5597; x_3=0.2106; x_7=0.5226; x_8 =1.9056;
θ=-26.38°;s_0=0.6932; e_{max}=0.002516;
In Galerkin method: Weighting function(W_i,i=1,4)= $1, e^x, \sin x, \cos x, \sin x\cos x$
Solution: x_1=1.3348; x_2=1.2565; x_4=1.6845; x_5=-0.5675; x_3=0.1128; x_7=0.6505; x_8 =1.9431;
θ=-26.38°; s_0=0.6932; e_{max}=0.002319;

Example 7: A six-bar of Fig.9 is required to trace the given path y=x 0≤x≤1 as one input link drives the whole mechanism through a 360 degree rotation. Applying the modular approach, circle points of the four-bar coupler of Example 3 with Galerkin method are determined first, thus yielding the length and swing angle of rocker. Then, the matching crank-rocker module is designed to be supplemented to the four-bar with a revolute joint at the circle point. The process described leads to the following numerical results:
In Precision-point method: Precision points(ψ_p(i),i=1,..,5)=0°,-20°,-45°,-85°,-90°;
Solution: x_4=2.6823; x_5=1.4993;x_m=-1.6625;y_m=2.0322;R=3.5657; α=15.08°; η=0.00°; β=30.00°; ϕ=-67.54°; u/p=-0.5044; r/p=0.8660;q/p=0.0662; e_{max}=0.001027;

In Subdomain method: Subdomains ($\psi_s(i)$,i=1,..,6)=0,-20°,-45°,-80°,-85°,-90°;
Solution: x_4=2.3670;x_5=1.1354;x_m=0.5972;y_m=0.5024; R=1.3182; α=30.91°; η=0.00°; β=30.00°; ϕ=-75.46°; u/p=-0.5188; r/p=0.8660;q/p=0.1383; e_{max}=0.003378;
In Galerkin method: Weighting function(W_i,i=1,5) $e^{-\psi}, e^{-\psi^2}, e^{-\psi^3}, e^{-\psi^4}, e^{-\psi^5}$
Solution: x_4=2.4016; x_5=1.1546 ;x_m=0.4867;y_m=0.6101;R:=1.4329;α=29.23°; η=0.00°; β=30.00°; ϕ=-74.61°;u/p=-0.5167; r/p=0.8660;q/p=0.13035; e_{max}=0.003207;

Example 8: Five-link mechanism of Fig. 10(a) is to be designed to generate the path y=x $0 \le x \le 1$ with in an input clockwise rotation of 90°. In accordance with the modular approach, the solution lies in finding the line points of the four-bar coupler of Example 3 with Galerkin method. The following outcome will define the sought design:
In Precision-point method: Precision points($\psi_p(i)$,i=1,..,4)=0°,-20°,-80°,-90°;
Solution: x_4=3.4292;x_5=2.0461;m=1.2588;n=-0.1204; e_{max}=-0.0022637;
In Subdomain method: Subdomains ($\psi_s(i)$,i=1,..,5)=0°,-10°,-45°,-85°,-90°;
Solution: x_4=3.5415;x_5=1.8451;m=1.0597;n=-0.0524; e_{max}=-0.0008472;
In Galerkin method: Weighting function(W_i,i=1,4) $e^{-\psi}, e^{-\psi^2}, e^{-\psi^3}, e^{-\psi^4}$
Solution: x_4=3.5081;x_5=1.8999;m=1.1115;n=-0.07930; e_{max}=0.0006162;

Example 9: Mechanisms which have an input link driving the whole mechanism through a 360-degree rotation with circular and linear paths are widely used in practice. In this example, applying the modular approach, a crank-rocker module is designed with circle and line points on its coupler. The following results are obtained:
Selected dimensions of crank-rocker: q=0.2682; p=1; R=2.7902; u=2.2487;
Four-bar mechanisms: x_1=q; x_2=R; x_3=u; x_6=p; x_7=0; x_8=0; x_9=0;
The initial angle (ψ_0) and the crank rotation ($\Delta\psi$) of the input link are specified by designer. Here, ψ_0=30°; $\Delta\psi$=90° (counter clockwise) are selected. The numerical results of design for circle points in Galerkin method are the following:
x_4=-1.9750; x_5=-1.5291; x_m=0.5586; y_m=-0.8751; R=1.8226; e_{max}=0.001833;
The numerical results of design for line points in Galerkin method are the following:
x_4=2.2515; x_5=-1.5646;m=-1.5602; n=4.4946; e_{max}=0.035378;

In view of the numerical results displayed above, it can be said that as the number of links and joints increases the degree of precision in governing the desired path improves, as is to be expected. This justifies also the possible cost of using more elements in the preferred mechanism with respect to very fine errors.

5. CONCLUSION

A novel approach, termed as a modular approach, has been devised to design path-generating mechanisms with lower pairs. The essence of the approach lies in constructing the multi-link mechanisms out of two-link assemblies, called modules, which provide closed-form solutions for the design equations. Thus, there is always solution assurance for any physically feasible problem of path generation. Furthermore, there is the possibility of choosing the most appropriate one from among many possible solutions that may result from the process.
This approach can easily be extended to other areas of mechanism synthesis too.

REFERENCES

Akcali, I. and G. Dittrich (1989). "Path generation by subdomain method." *Mechanism and Machine Theory*, Vol. 24, No. 1, pp. 45-52.

Akcali, I. D. (1983). "Kinematic Design of Demag-type Crane." *H.U. Bulletin of Engineering and Natural Sciences*, Vol., No., pp. 139-157.

Akcali, I. D. (1987). "Design of Slider-Crank Mechanism for Function Generation." *Proc. 7th. IFTOMM World Congress on Theory of Machines and Mechanisms*, Sevilla.

Akcali, I. D. and L. C. JLindholm (1979). "A Novel Method for the 4-bar Function Generation Problem." *Proc. 5th. IFTOMM World Congress on Theory of Machines and Mechanisms*.

Bakthavachalam, N. and J. Kimbrell (1975). "Optimum synthesis of path-generating four-bar mechanisms." *Journal of engineering for industry*, Vol. 97, No. 1, pp. 314-321.

Dittrich, G. and R. Braune (1978). Getriebetechnik in Beispielen. Grundlagen und 46 Aufgaben aus der Praxis. München, Wien, R. Oldenbourg Verlag.

F, F. (1955). "Approximate synthesis of four-barlinkages." *J. Appl. Mech*, Vol. 77, No., pp. 853-861.
Hartenberg, R. S. and J. Denavit (1964). *Kinematic synthesis of linkages*, McGraw-Hill.

Kao, C.-C., C.-W. Chuang and R.-F. Fung (2006). "The self-tuning PID control in a slider–crank mechanism system by applying particle swarm optimization approach." *Mechatronics*, Vol. 16, No. 8, pp. 513-522.

Kramer, S. and G. Sandor (1975). "Selective precision synthesis—a general method of optimization for planar mechanisms." *Journal of Engineering for Industry*, Vol. 97, No. 2, pp. 689-701.

Roth, B. and F. Freudenstein (1963). "Synthesis of path-generating mechanisms by numerical methods." *Journal of Engineering for Industry*, Vol. 85, No. 3, pp. 298-304.

SH, C. (1956). *Engineering analysis*. Usa, McGraw-Hill.

Turkish Journal of Engineering

Turkish Journal of Engineering (TUJE)
Vol. 2, Issue 2, pp. 73-78, May 2018
ISSN 2587-1366, Turkey
DOI: 10.31127/tuje.350418
Research Article

APPLICATION OF HOMOTOPY PERTURBATION METHOD TO HEAT TRANSFER IN NANOFLUIDS

Jonathan Oahimire *[1] and Olusegun Adeokun [2]

[1] Department of Mathematics, Michael Okpara University of Agriculture, Umudike, Nigeria
ORCID ID 0000-0003-3685-484
imumolen@yahoo.co.uk

[2] Department of Mathematics and Statistics, University of Port Harcourt, Port Harcourt, Nigeria
ORCID ID 0000-0002-5498-1735
shegs637@gmail.com

* Corresponding Author
Received: 09/11/2017 Accepted: 15/12/2017

ABSTRACT
This paper investigates heat transfer in a nanofluid using the Homotopy Perturbation method. Similarity transformation variables and a stream function are used to transform the partial differential equations governing the fluid flow into ordinary differential equations. He's Homotopy perturbation method is then used to solve the resulting dimensionless equations. It was discovered that an increase in the fraction number, magnetic parameter or Grashof number led to a corresponding increase in the rate of heat transfer regardless of the nanoparticles in the fluid. These results are in agreement with those found in existing literature.

Keywords: *Nanofluid, Similarity Transformation, Homotopy Perturbation Method, Heat Transfer*

1. INTRODUCTION

Nanofluids are formed when nanoparticles such as oxide ceramics, nitrides, graphites etc are mixed with base fluids like water, polymer solutions and lubricants. Nanofluids possess heat transfer properties that can help address the energy demand and emission issues of the present world. They can be used for industrial cooling purposes and this could result in great energy savings and significantly reduce emission.

These properties and their potential benefits have made nanofluids an important area of research. Wang *et al*. (1999) in their research into the thermal conductivity of nanoparticle-fluid mixture provided suggestions to improve the conductivity of nanofluids. Do and Jang (2010) analyzed the effects of thermophysical properties Aluminum Oxide on the heat transfer of a flat micro heat pipe. Uddin *et al.* (2012) discovered that an increase in Newtonian heating enhanced the heat and mass transfer rate of a nanofluid. The dimensionless governing equations were solved using the Runge-Kutta-Fehlberg method coupled with shooting technique.

Hamad (2011) studied free convective flow of a nanofluid over a linearly stretching sheet in the presence of magnetic field. Oahimire *et al*. (2016) extended the work of Hamad by incorporating a thermal radiation parameter into the flow equations and solved them using the Runge-kutta Fehlberg method together with shooting technique. To the best of our knowledge, HPM has not been applied to solve the flow equations of Oahimire *et al*. (2016).

In this present study, HPM is applied to study the effects of volume fraction, magnetic field and buoyancy force on the rate of heat transfer of natural convection flow of a nanofluid over linearly stretching sheet in the presence of magnetic field. The Homotopy Perturbation method (HPM) is a technique based on the concept of the Homotopy from topology that was introduced by Dr. Ji-Huan He in 1998. It is a simple but effective method for solving non-linear partial differential equations. The basic idea is illustrated below. Consider a non-linear differential equation

$$[\boldsymbol{A}(\boldsymbol{u}) - \boldsymbol{f}(\boldsymbol{r})] = \boldsymbol{0} \qquad (1)$$

Where f(r) is a known analytic function and A(u) is a nonlinear differential operator which can be separated into 2 parts, one linear part, L and a non-linear part, N. i.e.

$$\boldsymbol{A}(\boldsymbol{u}) = \boldsymbol{L}(\boldsymbol{u}) + \boldsymbol{N}(\boldsymbol{u}) \qquad (2)$$

We construct a homotopy as follows

$$\boldsymbol{H}(\boldsymbol{u},\boldsymbol{p}) = (\boldsymbol{1}-\boldsymbol{p})[\boldsymbol{L}(\boldsymbol{u_0}) - \boldsymbol{L}(\boldsymbol{v_0})] + [\boldsymbol{A}(\boldsymbol{u}) - \boldsymbol{f}(\boldsymbol{r})] = \boldsymbol{0} \qquad (\boldsymbol{3})$$

where $\boldsymbol{p}$ is an embedding parameter that lies in the unit interval $[\boldsymbol{0},\boldsymbol{1}]$ and $\boldsymbol{v_0}$ is an initial guess of the solution to the equation. Setting the value of our small parameter to 0, we have the initial guess while setting its value to 1 gives us the original equation. This process of changing p from 1 to 0 is called a deformation.

$$\boldsymbol{H}(\boldsymbol{u},\boldsymbol{0}) = \boldsymbol{L}(\boldsymbol{u}) - \boldsymbol{L}(\boldsymbol{v_0}) = \boldsymbol{0} \qquad (\boldsymbol{4})$$

$$\boldsymbol{H}(\boldsymbol{u},\boldsymbol{1}) = \boldsymbol{A}(\boldsymbol{u}) - \boldsymbol{f}(\boldsymbol{r}) = \boldsymbol{0} \qquad (\boldsymbol{5})$$

According to the HPM, we assume our solution is in form of a series

$$\boldsymbol{u} = \boldsymbol{u_0} + \boldsymbol{p}\boldsymbol{u_1} + \boldsymbol{p^2}\boldsymbol{u_2} + \cdots$$

We solve for $\boldsymbol{u_n}$ iteratively and setting $\boldsymbol{p} = \boldsymbol{1}$, we have

$$\boldsymbol{u} = \boldsymbol{u_0} + \boldsymbol{u_1} + \boldsymbol{u_2}$$

This is the approximate solution to Eq. (1). We have the freedom of choice for the operator L. However great care must be taken to choose an operator which simplifies the solution process as the solution depends entirely on the choice of the L and the initial guess $\boldsymbol{v_0}$. Ayati and Biazar (2015) showed that in most cases, the HPM solution is convergent.

NOMENCLATURE
a = Constant
g = Acceleration due to gravity
k = Thermal Conductivity
P_r = Prandtl Number
T = Fluid Temperature
T_w = Surface Temperature
T_∞ = Free Stream Temperature
u,v = Velocity Components
x,y = Cartesian Coordinates
f(x) = Dimensionless Stream Function
G_r = Grashof Number
q_r = Heat Flux Radiation
B_o = Magnetic Field of Constant Strength
R = Radiation Parameter
K_s = Rosseland Mean Absorption Coefficient
K = Thermal Conductivity Coefficient
GREEK SYMBOLS
β = Thermal Expansion Coefficient
μ = Dynamic Coefficient of Viscosity
θ (η) = Dimensionless Temperature
η = Similarity Variable
ρ = Fluid Density
ψ = Stream Function
σ' = Stefan-Bottzman Constant

2. MATHEMATICAL FORMULATION

Consider a steady, two-dimensional flow of an incompressible viscous nanofluid past a linearly semi-infinite stretching sheet. Magnetic field of strength B_0 is applied perpendicularly to the sheet. The nanofluid under consideration is water-based and contains Copper, Silver, Aluminum oxide and Titanium Dioxide. The nanofluid is assumed to be in thermal equilibrium. Following Oahimire *et al.* (2016), the governing equations are:

$$\frac{\partial \boldsymbol{u'}}{\partial \boldsymbol{x'}} + \frac{\partial \boldsymbol{v'}}{\partial \boldsymbol{y'}} = \boldsymbol{0} \qquad (\boldsymbol{6})$$

$$\boldsymbol{\rho_{nf}}\left[\boldsymbol{u'}\frac{\partial \boldsymbol{u'}}{\partial \boldsymbol{x'}} + \boldsymbol{v'}\frac{\partial \boldsymbol{v'}}{\partial \boldsymbol{y'}}\right] = \boldsymbol{\mu_{nf}}\frac{\partial^2 \boldsymbol{u'}}{\partial \boldsymbol{y'^2}} - \boldsymbol{\sigma B_0 u'} + \boldsymbol{g\beta_t}(\boldsymbol{T'} - \boldsymbol{T'_\infty}) \qquad (7)$$

$$(\boldsymbol{\rho c_p})_{\boldsymbol{nf}}\left[\boldsymbol{u'}\frac{\partial \boldsymbol{T'}}{\partial \boldsymbol{x'}} + \boldsymbol{v'}\frac{\partial \boldsymbol{T'}}{\partial \boldsymbol{y'}}\right] = \boldsymbol{K_{nf}}\frac{\partial^2 \boldsymbol{T'}}{\partial \boldsymbol{y'^2}} - \frac{\partial \boldsymbol{q_r}}{\partial \boldsymbol{y'}} \qquad (\boldsymbol{8})$$

The boundary conditions of the equations are

$$\boldsymbol{u' = u'_w(x') = ax', v' = 0,\ T' = T'_w\ at\ y' = 0}$$

$$\boldsymbol{u' \to 0, T' \to T'_\infty, y' \to \infty} \quad (9)$$

Where q_r is the radiative heat flux, $\boldsymbol{T'}$ is the temperature of the fluid, $\boldsymbol{x' and y'}$ are the coordinates along and perpendicular to the sheet while $\boldsymbol{u' and\ v'}$ are the velocity components in the $\boldsymbol{x' and\ y'}$ directions respectively and a is a constant. The effective density (ρ_{nf}), effective dynamic viscosity (μ_{nf}), heat capacitance $(\rho C_p)_{nf}$ and the effective thermal conductivity (k_{nf}) of the nanofluid, in that order, are given as

$$\begin{gathered}\boldsymbol{\rho_{nf} = (1-A)\rho_f + A\rho_s}\\ \boldsymbol{\mu_{nf} = \frac{\mu_f}{(1-A)^{2.5}}}\\ \boldsymbol{(\rho C_p)_{nf} = (1-A)(\rho C_p)_f + A(\rho C_p)_s}\\ \boldsymbol{k_{nf} = k_f\left(\frac{k_s + 2k_f - 2A(k_f - k_s)}{k_s + 2k_f + 2A(k_f - k_s)}\right)}\end{gathered} \quad (10)$$

Where A is the solid volume fraction ($A \neq 1$), μ_f is the dynamic viscosity of the base fluid, while ρ_f and ρ_s are the densities of the pure fluid and the nanoparticle respectively. The constants k_f and k_s are the thermal conductivities of the base fluid and the nanoparticle respectively. Using Rosseland approximation given by $\boldsymbol{q_r = \frac{4\sigma'}{3k'}\frac{\partial T'^4}{\partial y'}}$ with Taylor's series expansion and differentiation, Eq. (8) becomes

$$\boldsymbol{(\rho c_p)_{nf}\left[u'\frac{\partial T'}{\partial x'} + v'\frac{\partial T'}{\partial y'}\right] = K_{nf}\frac{\partial^2 T'}{\partial y'^2} + \frac{16T_\infty^3\sigma'}{3k'}\frac{\partial^2 T'}{\partial y'^2}} \quad (11)$$

The following variables are used for transformation

$$\boldsymbol{u = \frac{u'}{\sqrt{av_f}}\ v = \frac{v'}{\sqrt{av_f}},\ \theta = \frac{T' - T'_\infty}{T'_w - T'_\infty},\ x = \frac{x'}{\sqrt{\frac{v_f}{a}}}.\ y = \frac{y'}{\sqrt{\frac{v_f}{a}}}} \quad (12)$$

Eq. (12) transforms Eq. (6), (7) and (11) into the following

$$\boldsymbol{\frac{\partial u}{\partial x} + \frac{\partial v}{\partial y} = 0} \quad (13)$$

$$\boldsymbol{u\frac{\partial u}{\partial x} + v\frac{\partial v}{\partial y} = \frac{1}{(1-A)\rho_f + \rho_s}\left[\frac{1}{(1-A)^{2.5}}\frac{\partial^2 u}{\partial y^2} - Mu + Gr\theta\right]} \quad (14)$$

$$\boldsymbol{u\frac{\partial \theta}{\partial x} + v\frac{\partial \theta}{\partial y} = \frac{1}{Pr}\frac{1}{(1-A)(\rho c_p)_f + A(\rho c_p)_s}\left[\frac{k_{nf}}{k_f} + R_d\right]\frac{\partial^2 \theta}{\partial y^2}} \quad (15)$$

Where $\boldsymbol{M = \frac{\sigma\beta_0}{a}}$ is the magnetic field parameter, $\boldsymbol{p_r = \frac{v_f}{\mu_{nf}}}$ is the Prandtl number, $\boldsymbol{R_d = \frac{16\sigma' T_\infty'^3}{3K^*\mu_{nf}}}$ is the radiation parameter, $\boldsymbol{G_r = \frac{g\beta_t(T'_w - T'_\infty)x}{a}}$ is the Grashof number and the corresponding boundary conditions are

$$\boldsymbol{u = x, v = 0, \theta = 1\ at\ y = 0} \quad (16)$$

$$\boldsymbol{u \to 0, \theta \to 0\ as\ y \to \infty}$$

To satisfy Eq. (7) we apply the stream function $\boldsymbol{u = \frac{\partial \psi}{\partial y}, v = -\frac{\partial \psi}{\partial x}, \eta = y, \psi = xf(\eta).\ \theta = \theta(\eta)}$ our equations reduce to

$$\boldsymbol{f''' + (1-A)^{2.5}[ff'' - (f')^2]\left[(1-A)(\rho_f + \rho_s) - (Mf' + Gr\theta)\right] = 0} \quad (17)$$

$$\boldsymbol{\frac{1}{Pr}\frac{1}{(1-A)(\rho C_p)_s}\left[\frac{k_{nf}}{k_f} + R_d\right]\theta''(\eta) + f(\eta)\theta'(\eta) = 0} \quad (18)$$

$$\boldsymbol{f(0) = 0, f'(0) = 1,\ \theta(0) = 0\ at\ \eta = 0}$$
$$\boldsymbol{f \to 0, \theta \to 0\ as\ \eta \to 0} \quad (19)$$

3. METHOD OF SOLUTION

The transformed non-linear equations can be written as

$$\boldsymbol{f''' + \alpha\left(\beta\left(ff'' - (f')^2\right)\right) - kf' + Gr\theta = 0}$$
$$\boldsymbol{f\theta' + H\theta'' = 0}$$

Where $\boldsymbol{\alpha = (1-A)^{2.5}, k = M, \beta = (1-A)\rho_f + \rho_s, H = \frac{1}{Pr}\frac{1}{(1-A)(\rho c_p)_f + A(\rho c_p)_s}\left(\frac{k_{nf}}{k_f} + R\right)}$

We construct the homotopy of the transformed equations as follows

$$\boldsymbol{(1-p)(f''' - f'''u_0) + p\left(f''' + \alpha\left(\beta\left(ff'' - (f')^2\right)\right) - kf' + Gr\theta\right) = 0}$$

And

$$\boldsymbol{(1-p)(\theta'' - \theta''t_0) + p(f\theta' + H\theta'') = 0}$$

We assume $\boldsymbol{f}$ and $\boldsymbol{\theta}$ in the following form

$$\boldsymbol{f = f_0 + pf_1 + p^2 f_2}$$
$$\boldsymbol{\theta = \theta_0 + p\theta_1 + p^2\theta_2}$$

and group the terms according to the order: For order zero, we have

$$\boldsymbol{\frac{d^3 f_0}{d\eta^3} - \frac{d^3 v_0}{d\eta^3} = 0}$$
$$\boldsymbol{\frac{d^2\theta_0}{d\eta^2} - \frac{d^2 t_0}{d\eta^2} = 0}$$

With boundary conditions

$$\boldsymbol{f_0(0) = 0, f_0'(0) = 0, f_0'(\infty) = 1, \theta_0(0) = 1, \theta_0(\infty) = 0}$$

For order one, we have

$$\boldsymbol{\frac{d^3 f_1}{d\eta^3} - \frac{d^3 v_0}{d\eta^3} + \alpha\left(Gr\theta_0 - k\frac{df_0}{d\eta} + \beta\left(f_0\frac{d^2 f_0}{d\eta^2} - \left(\frac{df_0}{d\eta}\right)^2\right)\right) = 0}$$

$$\frac{d^2\theta_1}{d\eta^2} + f_0\frac{d\theta_0}{d\eta} + (H-1)\frac{d^2\theta_0}{d\eta^2} + \frac{d^2t_0}{d\eta^2} = 0$$

With boundary conditions

$$f_1(0) = 0, f_1{}'(0) = 0, f_1{}'(\infty) = 0, \theta_1(0) = 1, \theta_1(\infty) = 0$$

For order two, we have

$$\frac{d^3f_2}{d\eta^3} + \alpha\left(Gr\theta - k\frac{df_1}{d\eta} + \beta\left(f_1\frac{d^2f_1}{d\eta^2} - \left(\frac{df_1}{d\eta}\right)^2\right)\right) = 0$$

$$\frac{d^2\theta_2}{d\eta^2} + f_1\frac{d\theta_1}{d\eta} + (H-1)\frac{d^2\theta_1}{d\eta^2} = 0$$

With boundary conditions

$$f_2(0) = 0, f_2{}'(0) = 0, f_2{}'(\infty) = 0, \theta_2(0) = 1, \theta_2(\infty) = 0$$

Solving the equations with their respective boundary conditions, we have the following solutions

$$f_0 = \frac{\eta^2}{12}$$
$$f_1 = \frac{c_1\eta^2}{2} - \alpha Gr\frac{\eta^3}{6} + \alpha(Gr+k)\frac{\eta^4}{144} + \alpha\beta\frac{\eta^5}{4320}$$
$$f_2 = c_3\frac{\eta^2}{2} + g_8\frac{\eta^4}{24} + g_9\frac{\eta^5}{60} + g_{10}\frac{\eta^6}{120} + g_{11}\frac{\eta^7}{210} + g_{12}\frac{\eta^8}{336} + g_{13}\frac{\eta^9}{504} + g_{14}\frac{\eta^{10}}{720} + g_{15}\frac{\eta^{11}}{990}$$
$$\theta_0 = 1 - \frac{\eta}{6}$$
$$\theta_1 = \frac{\eta^4}{864} - \frac{\eta}{4}$$
$$\theta_2 = c_2\eta + \frac{g_1}{4}\eta^4 - \frac{g_2}{5}\eta^5 + \frac{g_3}{6}\eta^6 + \frac{g_4}{7}\eta^7 + \frac{g_5}{8}\eta^8 - \frac{g_6}{9}\eta^9 - \frac{g_7}{10}\eta^{10}$$

Where

$$c_1 = 2\alpha Gr - \alpha k - \frac{\alpha\beta}{4}$$
$$c_2 = -\frac{216}{4}g_1 + \frac{1296}{5}g_2 - 1296g_3 - \frac{46656}{7}g_4 - \frac{279936}{8}g_5 + \frac{1679616}{9}g_6 + \frac{10077696}{10}g_7$$
$$c_3 = -(6g_8 + 18g_9 + \frac{1296}{20}g_{10} + \frac{7776}{30}g_{11} + \frac{46656}{42}g_{12} + \frac{279936}{56}g_{13} + \frac{1679616}{72}g_{14} + \frac{10077696}{90}g_{15})$$
$$g_1 = \frac{c_1}{4} - \frac{(H-1)}{72}$$
$$g_2 = \frac{\alpha Gr}{24}$$
$$g_3 = \frac{\alpha(Gr+k)}{576}$$
$$g_4 = \frac{\alpha\beta}{17280} - \frac{c_1}{432}$$
$$g_5 = \frac{\alpha Gr}{1296}$$
$$g_6 = \frac{\alpha(Gr+k)}{144}$$
$$g_7 = \frac{\alpha\beta}{933120}$$
$$g_8 = c_1\alpha k + \frac{\alpha Gr}{4}$$
$$g_9 = c_1\alpha\beta - \frac{\alpha^2 GrK}{2} - \frac{\alpha\beta\, C_1{}^2}{2}$$
$$g_{10} = \frac{\alpha^2K(Gr+K)}{36} - \frac{\alpha^2C_1\beta\, Gr}{3}$$
$$g_{11} = \frac{\alpha^2K\,\beta - \alpha Gr}{864} + \alpha\beta\left(\frac{c_1\alpha(Gr+k) + 12\alpha^2Gr^2}{144}\right)$$
$$g_{12} = \alpha\beta\left(\frac{4C_1\alpha\beta}{2160} - \frac{\alpha^2Gr(Gr+K)}{144}\right)$$
$$g_{13} = \alpha\beta\left(\frac{\alpha^2(Gr+K)^2}{5184} + \frac{\alpha^2Gr\beta}{270}\right)$$
$$g_{14} = \alpha\beta\left(\frac{\alpha^2\beta(Gr+K)}{77760}\right)$$
$$g_{15} = \frac{\alpha^3\beta^3}{746496}$$

We can calculate the value of the constant coefficients using the boundary conditions. Following standard practice, we replace the boundary condition $\eta = \infty$ with $\eta = 6$.

4. DISCUSSION AND RESULTS

Numerical evaluation of the solutions was performed with mathematical software "Matlab" and the results are presented in tabular form. This was done to illustrate effect of some governing parameters involved. The rate of heat transfer for different value of volume fraction (A), magnetic parameter(M) and Grashof number(Gr) are obtained as shown in table 2. We notice that an increase in the values of A, M and Gr led to an increase in the values of the heat transfer coefficient –θ(0).

The therrmophysical properties of nanoparticles used in the evaluation as given by Hamad (2011) are shown below.

Table 1. Thermo physical properties of water and nanoparticles. Hamad (2011)

Compound	ρ (kg/m^3)	C_p (J/kgK)	k (W/mK)
Pure water	997.1	4179	0.613
Copper (Cu)	8933	385	401
Alumina (Al_2O_3)	3970	765	40
Silver (Ag)	10500	235	429
Titanium Oxide (TiO_2)	4250	686.2	8.9538

These values where used together with the solutions to obtain the following table showing the effects of varying different flow parameters on the heat transfer of the nanofluid.

Table 2. Effects of variation of A, Gr and M on the rate of heat transfer

			$-\theta(0)$	$-\theta(0)$	$-\theta(0)$	$-\theta(0)$
A	M	Gr	Cu	Al_2o_3	Ag	T_iO_2
0.2	0.5	0.2	-6.3599×10^3	-2.8533×10^3	-7.4671×10^3	-3.0511×10^3
0.3	0.5	0.2	-4.5049×10^3	-1.9933×10^3	-5.2976×10^3	-2.1350×10^3
0.4	0.5	0.2	-3.0301×10^3	-1.3219×10^3	-3.5695×10^3	-1.4183×10^3
0.5	0.5	0.2	-1.8996×10^3	-8.1678×10^3	-2.2415×10^3	-8.7778×10^3
0.6	0.5	0.2	-1.0754×10^3	-4.5554×10^3	-1.2711×10^3	-4.9051×10^3
0.1	0.6	0.2	-8.5324×10^3	-3.8252×10^3	-1.0019×10^4	-4.0908×10^3
0.1	0.7	0.2	-8.4332×10^3	-3.7259×10^3	-9.9194×10^3	-3.9915×10^3
0.1	0.8	0.2	-8.3339×10^3	-3.6266×10^3	-9.8201×10^3	-3.8922×10^3
0.1	0.9	0.2	-8.2346×10^3	-3.5274×10^3	-9.7209×10^3	-3.7929×10^3
0.1	1.0	0.2	-8.1353×10^3	-3.4281×10^3	-9.6216×10^3	-3.6937×10^3
0.1	0.5	0.3	-8.5332×10^3	-3.8260×10^3	-1.0019×10^4	-4.0916×10^3
0.1	0.5	0.4	-8.4348×10^3	-3.7275×10^3	-9.9210×10^3	-3.9931×10^3
0.1	0.5	0.5	-8.3363×10^3	-3.6290×10^3	-9.8225×10^3	-3.8946×10^3
0.1	0.5	0.6	-8.2378×10^3	-3.5306×10^3	-9.7241×10^3	-3.7961×10^3
0.1	0.5	0.7	-8.1393×10^3	-3.4321×10^3	-9.6256×10^3	-3.6977×10^3

5. CONCLUSION

In this work, the dimensionless equations of the governing equations were solved with HPM and the effects of M, Gr and A on heat transfer are presented in Table 2. And we notice that increasing the values of M, Gr and A leads to a corresponding increase in the rate of heat transfer in all of the nanoparticles considered. This is in agreement with the solutions gotten using the Runge-Kutta-Fehlberg method by Oahimire *et al.* (2016). This shows that He's Homotopy Pertubation method is an effective method for solving similar flow problems.

REFERENCES

Ayati, Z. and Biazar, J. (2015). "On the Convergence of the Homotopy Perturbation Method." *Journal of the Egyptian Mathematical Society,* Issue 23. pp. 424-428

Do, K. H. and Jang S. (2010). "Effect of nanofluids on the thermal performance of a flat micro heat pipe with a rectangular grooved wick." *International Journal of Heat and Mass Transfer,* 53, pp 2183 – 2192

Hamad M.A.A. (2011). "Analytical solution of natural convection flow of a nanofluid over a linearly stretching sheet in the presence of magnetic field." *International Communications in Heat and Mass Transfer,* Vol. 38, Issue 4, pp 487 – 492.

Oahimire J.I, Bazuaye F.E and Harry T. H (2016). "Numerical method for the analysis of thermal radiation on heat transfer in nanofluid." *Journal of Nanoscience and Technology*, Vol.3, Issue 1, pp 1-4

Uddin M.J., Kahn W. A., and Ismail A.I. (2012). "MHD Free Convective Boundary Layer flow of a Nanofluid past a Flat Vertical Plate with Newtonian Heating Boundary condition." *PLoS ONE 7(11): e49499 doi:10.1371/journal.pone.49499*

Wang X., Xu X. and Choi S.U.S. (1999). "Thermal conductivity of nanoparticle - fluid mixture." *Journal of Thermophysics and Heat Transfer*, Vol. 13, No. 4, pp 474 – 80.

Turkish Journal of Engineering

Turkish Journal of Engineering (TUJE)
Vol. 2, Issue 2, pp. 79-87 May 2018
ISSN 2587-1366, Turkey
DOI: 10.31127/tuje.345351
Research Article

APPROACHES TO THE DESIGN OF A PLANAR PARALLEL MANIPULATOR

Hüseyin Mutlu *[1] and İskender Özkul [2]

[1] Mersin University, Engineering Faculty, Mechanical Engineering Department, Mersin, Turkey
ORCID ID 0000-0002-4770-2873
huseyinmutlu@yahoo.com

[2] Mersin University, Engineering Faculty, Department of Mechanical Engineering, Mersin, Turkey
ORCID ID 0000-0003-4255-0564
iskender@mersin.edu.tr

* Corresponding Author

Received: 20/10/2017 Accepted: 20/12/2017

ABSTRACT
Manipulator is an important part of a whole robot assembly, forming the mechanical infrastructure of a mechatronic system. Selection of the manipulator affects a broad area extending from modelling to design, from control to operation and furthermore from accuracy to its economy. This study aimed methods of design and operation of a parallel planar robotic assembly have been demonstrated. Modules of the assembly with two degrees of freedom have been designed on a two-point, two-velocity and three point-position bases. Ways of actuating and controlling the motion of the assembly have been shown. Efficiency and effectiveness of the approaches have been illustrated numerically.

Keywords: *Mechanism, Manipulator, Robotic*

1. INTRODUCTION

Manipulator is an important part of a whole robot assembly, forming the mechanical infrastructure of a mechatronic system. Selection of the manipulator affects a broad area extending from modelling to design, from control to operation and furthermore from accuracy to its economy. Manipulator can be constructed by bringing together rotary and/or sliding elements or a combination of these in a suitable manner. Within this context, open or closed kinematic chains formed as such will result in the so-called serial or parallel robotic structures, (Duffy, 1996).

The most fundamental manipulator types like cartesian, cylindrical, spherical, articulated arm and scara are the most widespread examples of serial manipulator. Most classical works rely upon the serial manipulator, which is based on the open chain, (Koren, 1987; Stadler, 1995; Fu *et al.*, 1987, Groover *et al.*, 1986). Although serial manipulators have a high maneuverability within a large workspace, they are subject to significant limitations. First of all, they have limited load carrying capacities due to their highly deformable structures, which are prone to vibrations under large velocities. Additionally, it is probable that the fact that an actuator is needed at each joint, for a serial manipulator having many joints in an open chain, might lead to a rise in the initial and operating costs of the robotic assembly. On the other hand, most of the issues mentioned above are solved by using parallel manipulators facing only the limitation of having small workspaces. Thus, such advantages have invited the research attention on parallel manipulators in recent years, (Innocenti and Castelli, 1990; Bernier *et al.*, 1995, Harris, 1995; Liu, 1995).

Since the workspace of a parallel manipulator is limited, the problem of overlapping the actual space in which the physical tasks like welding, cutting conveying etc. Are to be fulfilled with that of the manipulator becomes significant. The solution of the problem passes through the accurate positioning of the manipulator. Thus, determining optimum values of all the adjustable parameters in a robot assembly constitutes a design task.

Here in this work, approaches to the design of a parallel planar manipulator with two degrees of freedom have been shown. The design of the manipulator has been reduced to the design of modules which considerably dissolve the complexity of the original assembly, mathematically and physically, thus always assuring closed-form solution. Then how actuators may be utilized to operate the assembly and to form an analog robot have been demonstrated.

2. THEORY

The kinematic scheme of the parallel manipulator in consideration is drawn in Fig. 1.

It can be seen that the parallel manipulator in question can be constituted by bringing together two of the basic module shown in Fig. 2.

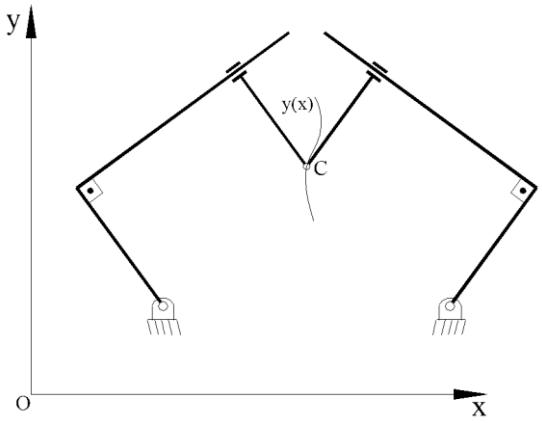

Fig. 1. Kinematic scheme

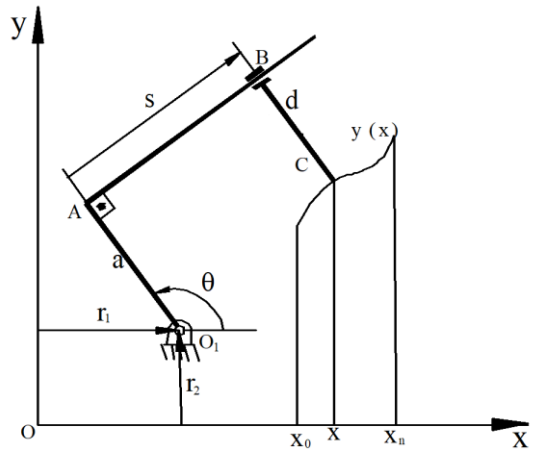

Fig. 2. Module parameters

The fundamental problem here is to determine the most appropriate values of the module parameters involved such that the end point C of the module follow a desired trajectory y (x) within [x_0, x_n] domain. To this end, the following can be written from Fig. 2:

$$x = r_1 + (a-d)\cos\theta + s\sin\theta \quad (1)$$

$$y = r_2 + (a-d)\sin\theta - s\cos\theta \quad (2)$$

If (a-d) is designated by b and s is eliminated from the above equations, then a displacement function G(x, y, θ) characterizing the motion of the module on the trajectory is obtained:

$$G(x,y,\theta) = y\sin\theta + x\cos\theta - r_1\cos\theta - r_2\sin\theta - b = 0 \quad (3)$$

Considering that the robot arm will rotate about O according to the θ' motion variable starting from an initial position θ_0, the following relationships can be written to meet the motion co-ordination requirements:

$$\theta = \theta_0 + \theta' \quad (4)$$

$$\theta' = r_x(x - x_0) \quad (5)$$

$$r_x = \Delta\theta / \Delta x,\ \Delta\theta = \theta_n - \theta_0,\ \Delta x = x_n - x_0 \tag{6}$$

where θ_n is the final position of the robot arm corresponding to the point (x_n) of the given trajectory. Evaluating the above relationships together with the trigonometric identities and rearranging will yield the following expression:

$$G(x, y, r_1, r_2, b, \theta_0, \theta') = \sin\theta_0 (y\cos\theta' - x\sin\theta')$$

$$+ \cos\theta_o (y\sin\theta' + x\cos\theta') + r_1(\sin\theta_o \sin\sin\theta' - \cos\theta_o \cos\theta')$$

$$- r_2(\sin\theta_o \cos\theta' + \cos\theta_o \sin\theta') - b = 0 \tag{7}$$

Now, it is possible to obtain velocity relationships by taking the first derivative of the displacement function G with respect to time:

$$\frac{dG}{dt} = \frac{dG}{d\theta}.\frac{d\theta}{dt} \tag{8}$$

If the velocities of the end point of the manipulator in the x and y directions are represented by V_x and V_y, respectively, and the angular speed of the rotating arm is designated by ω, then the following will come out of (8):

$$\frac{1}{\omega}.\frac{dG}{dt} = \sin\theta_0 (\frac{V_y}{\omega}\cos\theta' - \frac{V_x}{\omega}\sin\theta' - y\sin\theta' - x\cos\theta')$$
$$+ \cos\theta_0 (\frac{V_y}{\omega}\sin\theta' + \frac{V_x}{\omega}\cos\theta' + y\cos\theta' - x\sin\theta')$$
$$+ r_1(\cos\theta_0 \sin\theta' + \sin\theta_0 \cos\theta')$$
$$+ r_2(\sin\theta_0 \sin\theta' - \cos\theta_0 \cos\theta') = 0 \tag{9}$$

where

$$\omega = \frac{d\theta}{dt} = \frac{d\theta'}{dt};\ V_y = \frac{dy}{dt};\ V_x = \frac{dx}{dt} \tag{10}$$

Examination of the basic displacement and velocity functions (7) and (9) will reveal that there are four available parameters (r_1, r_2, θ_0, b) for formulating a design. One approach for a formulation of manipulator design is to require that the end point of the manipulator fit to specified two-position and two-velocity values. In such a context, if Precision-Point or Accuracy-Point (Hartenberg and Denavit, 1964) Subdomain (Akçalı and Dittrich, 1989a) and Galerkin (Akçalı and Dittrich, 1989b) methods are applied to displacement and velocity functions, then the following will result as the basic design equations:

$$P_i(\theta_0) + r_1 R_i(\theta_0) - r_2 Q_i(\theta_0) - bE_i. = 0 \quad i = 1,2 \tag{11}$$

$$H_i(\theta_0) + r_1 Q_i(\theta_0) + r_2 R_i(\theta_0) = 0 \ \ i = 1,2 \tag{12}$$

where:

$$Q_i(\theta_0) = D_i \sin\theta_0 + C_i \cos\theta_0 \quad ;$$
$$R_i(\theta_0) = C_i \sin\theta_0 - D_i \cos\theta_0$$

$$H_i(\theta_0) = K_i \sin\theta_0 + L_i \cos\theta_0 \quad ;$$
$$P_i(\theta_0) = A_i \sin\theta_0 + B_i \cos\theta_0 \quad i = 1,2 \tag{13}$$

The coefficients contained in (13) are defined is accordance with each method as follows: Accuracy-Point method takes into account points x_i i =1,2:

$$A_i = y_i \cos_i^{'} - x_i \sin\theta_i^{'};\ B_i = y_i \sin\theta_i^{'} + x_i \cos\theta_i^{'}$$

$$C_i = \sin\theta_i^{'}\ ;\ D_i = \cos\theta_i^{'};$$
$$E_i = 1.0 \quad \Big\} \quad \text{i = 1,2} \tag{14}$$
$$K_i = (\frac{V_y}{\omega})_i D_i - (\frac{V_x}{\omega})_i C_i - B_i \quad ;$$
$$L_i = (\frac{V_y}{\omega})_i C_i + (\frac{V_x}{\omega}) D_i + A_i$$

Subdomain Method considers subintervals $[x_{i-1}, x_i]$ i = 1,2:

$$A_i = \int_{\theta_{i-1}^{'}}^{\theta_i^{'}} (y\cos\theta' - x\sin\theta')d\theta' \quad ;$$
$$B_i = \int_{\theta_{i-1}^{'}}^{\theta_i} (y\sin\theta' + c\cos\theta')d\theta'$$
$$\Big\} \quad \text{i = 1,2}$$
$$C_i = \int_{\theta_{i-1}^{'}}^{\theta_i^{'}} \sin\theta' d\theta' = \cos\theta_{i-1}^{'} - \cos\theta_i^{'} \quad ;$$
$$D_i = \int_{\theta_{i-1}^{'}}^{\theta_i^{'}} \cos\theta' d\theta' = \sin\theta_i^{'} - \sin\theta_{i-1}^{'}$$

$$E_i = \int_{\theta_{i-1}^{'}}^{\theta_i^{'}} d\theta' = \theta_i^{'} - \theta_{i-1}^{'} \quad ;$$
$$K_i = \int_{\theta_{i-1}^{'}}^{\theta_i^{'}} \Big[\frac{1}{\omega}\frac{d}{dt}(y\cos\theta' - x\sin\theta')\Big] d\theta' \quad \text{i = 1,2} \tag{15}$$

$$L_i = \int_{\theta_{i-1}^{'}}^{\theta_i^{'}} \Big[\frac{1}{\omega}\frac{d}{dt}(y\sin\theta' + x\cos\theta')\Big] d\theta'$$

The coefficients appearing in (13) are evaluated by Galerkin method, with reference to selected weighting functions w_i i = 1,2 as shown below:

$$A_i = \int_{\theta_0^{'}}^{\theta_n^{'}} (y\cos\theta' - x\sin\theta')w_i d\theta' \quad ;$$
$$B_i = \int_{\theta_0^{'}}^{\theta_n^{'}} (y\sin\theta' + x\cos')w_i d\theta'$$
$$C_i = \int_{\theta_0^{'}}^{\theta_n^{'}} \sin\theta' w_i d\theta' \quad ; \quad D_i = \int_{\theta_0^{'}}^{\theta_n^{'}} \cos\theta' w_i d\theta'$$
$$E_i = \int_{\theta_0^{'}}^{\theta_n^{'}} w_i d\theta' \quad \Big\} \ \text{i = 1,2} \tag{16}$$

$$K_i = \int_{\theta_n'}^{\theta_0'} \left[(\frac{V_y}{w})\cos\theta' - (\frac{V_x}{w})\sin\theta' - y\sin\theta' - x\cos\theta' \right] w_i d\theta'$$

$$L_i = \int_{\theta_0'}^{\theta'n} \left[(\frac{V_y}{\omega})\sin\theta' + (\frac{V_x}{\omega})\cos\theta' + y\cos\theta' - x\sin\theta' \right] w_i d\theta'$$

In the solution phase of design formulation, which consists of four non-linear equations, b, r_2 and r_1 are eliminated, reducing the set (11)-(12) to the following:

$$P_{ss}\sin^2\theta_0 + P_{sc}\sin\theta_0\cos\theta_0 + P_{cc}\cos^2\theta_0 = 0 \quad (17)$$

In the general case, there are two solutions given by:

$$\theta_{0_+^-} = \tan^{-1}\left(\frac{-P_{sc+}^{-}(P_{sc}^2 - 4P_{ss}P_{cc})^{1/2}}{2P_{ss}}\right) \quad (18)$$

where:

$$P_{ss} = P_{1ss}R_2'' - P_{2ss}R_1'' \quad ; \quad P_{sc} = P_{1sc}R_2'' - P_{2sc}R_1'' \quad ; \quad P_{cc} = P_{1cc}R_2'' - P_{2sc}R_1'' \quad (19)$$

$$\left.\begin{aligned} A_1' &= A_1E_2 - A_2E_1 \;;\; B_1' = B_1E_2 - B_2E_1 \\ C_1' &= C_1E_2 - C_2E_1 \;;\; D_1' = D_1E_2 - D_2E_1 \end{aligned}\right\} \quad (20)$$

$$\left.\begin{aligned} R_j'' &= C_1'C_j + D_1'D_j \;;\; P_{jss} = A_1'C_j + D_1'K_j \\ P_{jsc} &= B_1' - C_j - A_1'D_j + C_1'K_j + D_1'L_j \;;\; P_{jcc} = C_1'L_j - B_1'D_j' \end{aligned}\right\} j = 1,2 \quad (21)$$

Since for a given tangent value, there exist two angles separated by 180°, four possible angles might satisfy equation (17). Thus, in order to decide on the technically meaningful ones as well as on the quality of outcome, a motion analysis should be carried out.

If the actuation of the manipulator is based upon (θ , s) which are computed by (4)-(6) and (22) given below, then position error e is evaluated by means of (1), (2), (22) and (23), where $x_{th}, y_{th}, x_{ac}, y_{ac}$ are theoretical and actual co-ordinates, respectively,

$$s = \left[(x_{th} - r_1)^2 + (y_{th} - r_2)^2 - b^2 \right]^{1/2} \quad (22)$$

$$e = \left[(x_{th} - x_{ac})^2 + (y_{th} - y_{ac})^2 \right]^{1/2} \quad (23)$$

In order to determine error in velocity, first theoretical velocities V_{xth}, V_{yth} and V_{th}, then actual velocities V_{xac}, V_{yac} and V_{ac} are calculated with reference to (24)-(26), finally ending in (27).

$$\frac{V_{xth}}{\omega} = \frac{1}{r_x};\frac{V_{yth}}{\omega} = (\frac{dy}{dx}).\frac{1}{r_x};\frac{V_{th}}{\omega} = \left[(\frac{V_{xth}}{\omega})^2 + (\frac{V_{yth}}{\omega})^2 \right]^{1/2} \quad (24)$$

$$\frac{1}{\omega} \qquad \frac{ds}{dt} = \frac{1}{s}\left[(x_{th} - r_1)\frac{V_{xth}}{\omega} + (y_{th} - r_2)\frac{V_{yth}}{\omega} \right] \quad (25)$$

$$\frac{V_{xac}}{\omega} = -b\sin\theta + \frac{1}{\omega}(\frac{ds}{dt})\sin\theta + s\cos\theta$$

$$\frac{V_{yac}}{\omega} = b\cos\theta - (\frac{ds}{dt})\frac{1}{\omega}\cos\theta + s\sin\theta \quad ;$$

$$\frac{V_{ac}}{\omega} = (V_{xac}^2 + V_{yac})^{1/2} \quad (26)$$

$$\frac{e_v}{\omega} = \left[(V_{xth} - V_{xac})^2 + (V_{yth} - V_{yac})^2 \right]^{1/2} \quad (27)$$

3. SIMPLIFIED APPROACH

By letting a = d or b = 0 in Fig. 2, and by requiring that three point-positions on the specified trajectory be satisfied in the sense of Accuracy-Point, Subdomain and Galerkin methods, by the end point of the robot arm, a simplified approach can be made to the problem. In that case, the displacement function G becomes:

$$G(x, y, \theta) = y - r_2 - (x - r_1)\tan\theta = 0 \quad (28)$$

Then the design equations take the form of a set of three linear equations as shown below:

$$A_i - B_i t_0 + C_i t_1 + D_i t_2 = 0 \quad \text{i} = 1,2 \quad (29)$$

where:

$$t_0 = \tan\theta_0;\; t_1 = a_1 + a_2 t_0;\; t_2 = a_1 t_0 - a_2 \quad (30)$$

Coefficients in Accuracy-Point Method are as follows:

$$A_i = y_i - x_i\tan\theta_i' \quad ; \quad B_i = x_i + y_i\tan\theta_i' \quad ; \quad C_i = \tan\theta_i' \quad ; \quad D_i = 1 \quad (31)$$

These in Subdomain Method are:

$$\left.\begin{aligned} A_i &= \int_{\theta i-1}^{\theta_{1i}'}(y - x\tan\theta')d\theta' \;;\; B_i = \int_{\theta i-1}^{\theta_{1i}'}(x + y\tan\theta')d\theta' \;; \\ C_i &= \int_{\theta i-1}^{\theta_{1i}'}\tan\theta' d\theta' \;;\; D_i = \int_{\theta i-1}^{\theta_i'} d\theta' \end{aligned}\right\} \quad (32)$$

In Galerkin Method, the coefficients are defined as such:

$$A_i = \int_{\theta i-1}^{\theta_i'} (y - x\tan\theta')w_i d\theta';$$

$$B_i = \int_{\theta i-1}^{\theta_i'} (x + y\tan\theta')w_i d\theta';$$

$$C_i = \int_{\theta i-1}^{\theta_i'} \tan\theta' w_i d\theta';\ D_i = \int_{\theta i-1}^{\theta_i'} w_i d\theta' \qquad (33)$$

Solution of the design equations yields the sought set (r_1, r_2, θ_0) as given below:

$$\theta_0 = \tan^{-1}(t_0) \quad ; \quad r_2 = (t_1 t_0 - t_2)/(1 + t_0^2) \quad ; \quad r_1 = t_1 - r_2 t_0 \qquad (34)$$

where:

$$t_0 = -A''/B'' \quad ; \quad t_1 = (B_2' t_0 - A_2')/C_i \quad ;$$
$$t_2 = \left[-A_1 + B_1 t_0 - C_1(B_2' - A_2')/C_2' \right]/D_1 \quad \} \qquad (35)$$

$$A_j' = D_k A_1 - D_1 A_k \quad ; \quad B_j' = D_k B_1 - D_1 B_k \quad ;$$
$$C_j' = D_k C_1 - D_1 C_k \quad \text{j = 1,2}$$
$$\text{k = j + 1} \qquad (36)$$

$$A'' = C_2' A_1' - C_1' A_2' \ ; \ B'' = B_2' C_1' - B_1' C_2' \qquad (37)$$

To secure a pair of solutions needed in the manipulator, the solution process is implemented twice by a change in method or some input parameters like the amount of arm rotation or the sense of rotation, if necessary.

4. ACTUATION POSSIBILITIES

The basic module is, in fact, a serial manipulator, Fig. 2, while the manipulator constructed out of two or possibly more basic modules will be of parallel type, securing more stiffness by its mechanical structure. One disadvantage of the serial manipulator is that one actuator should be available at each joint to the loss of payload capacities of the robot assembly. Thus, the advantageous feature of the parallel robot, namely having less actuators than the number of joints, offers possibilities of using analogously programmable actuators attached to the ground. Since actuation of the manipulator under consideration depends on slider displacement (s) and arm rotation (θ), possible analogously programmable actuators are either a function generating four-bar or an inverted slider-crank mechanism, the dimensions of which are continuously adjustable according to the design of the generator, which changes by trajectory (y), Fig. 3 (a), (b).

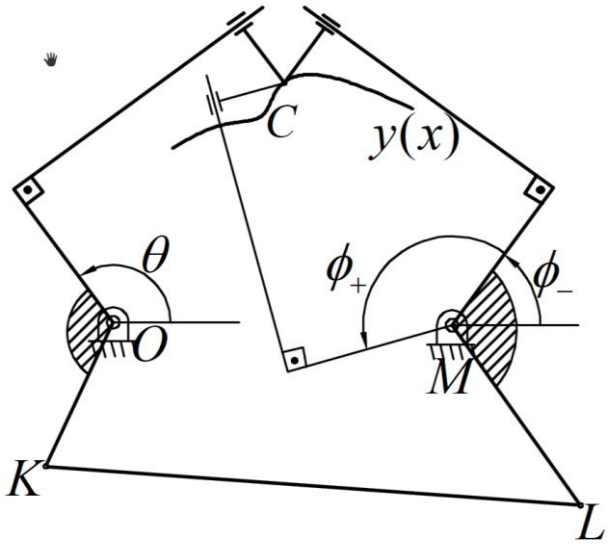

(a)

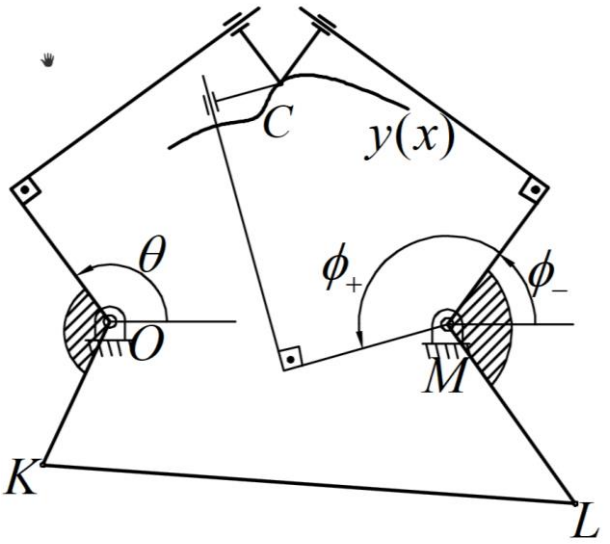

(b)

Fig. 3. Actuators of a parallel manipulator

The functions of the 4-bar OKML in Fig. 3(a) and the inverted slider-crank QOD in Fig. 3(b) are to provide the necessary rotation ϕ required about M and the needed slider displacement (s) along AB at the right time for the fulfilment and control of the trajectory task, just like the supply of right voltages at the right time in the case of electrical drive. In other words, two-degree –of-freedom manipulator receives one rotary actuation (θ) from the motor at ground pivot O, and the other actuation either at ground pivot M through OKML 4-bar (ϕ) angle generator, instead of a motor, Fig. 3(a), or along motion direction AB through QOD slider-crank (s) displacement generator instead of a hydraulic or pneumatic drive on the moving arm, Fig. 3(b). In this manner, the dimensions of the 4-bar or the slider-crank function generators can be viewed as an information storage medium transforming

input data like trajectory, manipulator design values and motor rotation into new actuation variables like ϕ or s in accordance with the following mathematical relationships

$$s = \frac{r_2 + b\sin\theta - y}{\cos\theta} \tag{38}$$

$$\tan\frac{\phi}{2} = \frac{A_+^- \sqrt{A^2 + B^2 - C^2}}{B + C} \tag{39}$$

with $A = (r_4 - y)\cos\theta$; $C = -h\cos\theta$;
$B = (y - r_2)\sin\theta + (r_3 - r_1)\cos\theta - b$ (40)

where (r_3, r_4, h) are the parameters of the second serial manipulator like (r_1, r_2, b) in the first serial manipulator.

From the discussion above, it is to be understood that next to the rotary actuator at O, if the two-degree-of-freedom robot assembly is to be brought into motion to follow a trajectory y by means of a programmed motion of the slider, then the slider-crank is designed with a suitable method like (Akçalı, 1987) such that functional relationship (38) is generated between the reverse rotations (-θ) of the motor at O and slider translation (s). If two-rotary actuators are to be used for the same purpose, in that case a 4-bar is designed by means of (Akçalı and Dittrich, 1989b) to generate (39) function between θ and ϕ in place of a motor at M in addition to the one located at O. Of course, in construction of the 4-bar or the inverted slider-crank, adjustability of dimensions is foreseen.

One advantage of these analogous designs is that the sense of actuation (θ, ϕ) will be kept same within long intervals as opposed to possibly frequent changes in the sign of actuation in digital applications. In the direct kinematic analysis, corresponding to (θ, ϕ) actuation, the following (x,y) trajectory co-ordinates will be generated:

$$x = r_1 + b\cos\theta + \frac{\sin\theta}{\sin(\theta - \phi)}[(r_3 - r_1)\cos\phi + (r_4 - r_2)\sin\phi + h - b\cos(\theta - \phi)] \tag{41}$$

$$y = r_2 + b\sin\theta - \frac{\cos\theta}{\sin(\theta - \phi)}[(r_3 - r_1)\cos\phi + (r_4 - r_2)\sin\phi + h - b\cos(\theta - \phi)] \tag{42}$$

5. ON APPLICATIONS

The design and operation of the manipulators proposed here are primarily based on analogous variables. As is well known, analogous variables are continuous in contrast with the discrete nature of digital variables, (raven 1987). Hence there are no zigzags in the functioning of actuators in driving the manipulators considered here. This aspect is consistently taken into considerations when applying the techniques presented here. Take, for instance, the problem of transporting an article from the point with (x_0, y_0) co-ordinates on a conveyor moving with velocity V_0 to the point with (x_n, y_n) co-ordinates on another conveyor with a linear velocity of V_n . In order to associate this problem with both general theory and simplified approach, it is sufficient to find a trajectory function $y(x)$ satisfying the velocity and the given end points. For instance, the cubic polynomial

$$y = ax^3 + bx^2 + cx + d \tag{43}$$

with the following computed coefficients (a, b, c, d) will be an answer to the requirements.

$$m_0 = \sqrt{(\frac{V_0 r_x}{\omega})^2 - 1}\,; m_n = \sqrt{(\frac{V_n r_x}{\omega})^2 - 1} \tag{44}$$

$$c_0 = \frac{y_n - y_0}{x_n - x_0}\,; c_1 = x_n^2 + x_n x_0 + x_0^2;\ c_2 = x_n + x_0 \tag{45}$$

$$k_1 = 3x_0^2 - c_1 \quad ; \quad k_2 = 2x_0 - c_2 \quad ; \quad l_1 = 3x_n^2 - c_1 \quad ; \quad l_2 = 2x_n - c_2 \tag{46}$$

$$a = \frac{l_2(m_0 - c_0) - k_2(m_n - c_0)}{k_1 l_2 - k_2 l_1} \quad ;$$
$$b = \frac{l_1(m_0 - c_0) - k_1(m_n - c_0)}{k_2 l_1 - k_1 l_2} \tag{47}$$

$$c = c_0 - ac_1 - bc_2 \quad ; \quad d = y_n - ax_n^3 - bx_n^2 - cx_n \tag{48}$$

where r_x, ω are selected as required in the techniques.

6. NUMERICAL RESULTS AND DISCUSSION

Analytical thoughts developed have been transformed into computer programs under Fortran 77 coding. Utilizing these programs, comprehensive illustrations are presented here to review the numerical results and to discuss their significance.

Example 1 A trajectory described by y = 0.5 x+ 0.5 0≤ x ≤ 1 is to be followed under a uniform velocity requirement matching a 10s. travel on the part of a two-arm manipulator with the sliding directions passing through the fixed revolute joints.

The solution lies in the implementation of the simplified approach twice. Data for the first implementation are in case of Precision-Point Method x_i, i=1,2,3 being [0.2;0.6;1.0] in case of Subdomain Method subintervals being $[x_{i-1}, x_i]$ i = 1,2,3 [0.0;0.40],[0.40;0.75], [0.75;1.00] and finally for Galerkin Method weighting functions w_i i =1,2,3 being $[x, x^2, x^3]$. The amount of arm rotation $\Delta\theta$ is taken to be 45°, for every method. The numerical results are displayed in Table 1, indicating also max absolute error, e_{max}.

Table 1. First Robot Arm for Trajectory y = 0.5 x+ 0.5 $0 \le x \le 1$

Method	r_1	r_2	$\theta_0(^o)$	E_{max}
Precision-Point	-0.0155	2.0311	-90.44	0.0035
Subdomain	-0.0768	2.0064	-87.74	0.0060
Galerkin	-0.0414	2.0306	-89.47	0.0042

Input for the second implementation are in Precision-Point Method x_i = 1, 2, 3 being [0.03;0.40;0.62] in Subdomain Method subintervals being [0.00;0.35], [0.35; 0.40], [0.40; 1.00]; in Galerkin Method weighting functions w_i = 1, 2, 3 being [x, x^2, x^3]. Arm rotation angle ($\Delta\theta$) has been taken as 45° in Precision-Point and Subdomain Methods but in Galerkin Method as 42°. The outcome has been presented in Table 2. When the two arms are put together to form the parallel manipulator in question, then the maximum absolute (e_{max}) error turns out to be 0.0034 in Precision-Point, 0.0056 in Subdomain and 0.0489 in Galerkin methods. Theoretical velocity on the trajectory is supposed to be 0.1118, constant throughout the motion. Maximum velocity errors in Precision-Point, Subdomain and Galerkin designs become 0.0152; 0.0183 and 0.0165, respectively.

Table 2. Second Robot Arm for Trajectory y = 0.5 x+ 0.5 0≤x≤1

Method	r_3	r_4	$\phi_0(^o)$	e_{max}
Precision-Point	-0.3934	1.8573	-74.90	0.0681
Subdomain	-0.1794	1.9583	-83.66	0.0163
Galerkin	-0.0891	2.1232	-87.82	0.0036

Example 2 Requirements of Example 1 are to be met by the general parallel manipulator of Fig. 1.

General theory is applied once, here. When data for precision points x_i, i=1,2, [0.4,0.7], for subdomains, [x_{i-1},x_i], [0.2;0.6],[0.6;0.9] for weighting functions w_i,i=1,2;[sin x,cos x] and $\Delta\theta$=45° are taken into account, the results shown in Table 3 are obtained.

Table 3. Modules For Trajectory y = 0.5 x+ 0.5 0≤x≤1

Method	r_1	r_2	$\theta_0(^o)$	b	e_{max}
Precision-Point	-0.7203	3.3156	-88.18	2.8405	0.0035
	-0.8205	2.0423	-24.75	1.3698	0.0653
Subdomain	-0.7082	3.3087	-88.49	2.8290	0.0026
	-0.8216	2.0405	-25.50	1.3870	0.0514
Galerkin	-0.7529	3.2559	-85.94	2.8022	0.0006
	-0.5659	1.9826	-22.50	1.0708	0.2228

Two significantly different module designs are brought together for the construction of the parallel manipulator. After this process, b values are slightly affected, leading to 1.4439, 1.3496 and 1.0902, in Precision-Point, Subdomain and Galerkin methods, respectively, leaving all others same. Maximum errors in the resulting parallel manipulators become 0.0026, 0.0026, 0.0007 in the aforementioned methods, respectively. Maximum deviations from the constant 0.1118 velocity value in Precision-Point, Subdomain and Galerkin methods turn out to be 0.0023, 0.0024, 0.0013, respectively.

If the results of two examples above are compared, it will be seen that the chances of getting more refined designs are always much more in the general theory against simplified approach. While more than one application is needed in the simplified approach for the formation of a parallel manipulator, only one implementation of general theory is sufficient. Another advantage of the general theory is that the mirror-image manipulator (with ϕ_+) is a good alternative when space for the manipulator (with ϕ_-) is not appropriate, since they both produce the same trajectories with the same end velocities.

The robotic assembly designed in this work differs from the classical constrained-motion mechanisms in that it has a flexible structure. While a classical one-degree of frecdom mechanism generates only one and constant curve, the robotic assembly under consideration can produce as many curves as the intervals of adjustability of parameters permit. If a change in the positions of fixed pivots of the two manipulators is not seen practical, then following the design of manipulators, the dimensions of the function-generating four-bar relating θ'_c rotations of the first manipulator to the ϕ'_c rotations of the second one can easily be made adjustable. In that case, the design of the function-generating 4-bar is realised with respect to a transformed function (θ'_c, ϕ'_c) corresponding to trajectory y_c (x_c) in a co-ordinate system $x_c - y_c$ located at the ground pivot (O) of the first manipulator in the following way : First, $\theta_M = \tan^{-1}[r_4 - r_2)/(r_3 - r_1)]$ is computed, then co-ordinate transformations x_c=(x-r_1)cosθ_M+(y-r_2)sinθ_M, y_c= -(x-r_1)sinθ_M+(y-r_2)cosθ_M $\theta'_c = \theta_c - \theta^0_c$, $\phi'_c = \phi_c - \phi^0_c$,where $\theta^0_c = \theta_0 - \theta_M$, $\phi^0_c = \phi_0 - \theta_M$ and $\theta_c = \tan^{-1}\frac{y_c}{x_c} + \cos^{-1}\frac{b}{\sqrt{x_c^2 + y_c^2}}$, $\phi_c = \pi - \tan^{-1}\frac{y_c}{OM - x_c} + \cos^{-1}\frac{h}{\sqrt{y_c^2 + (OM - y_c)^2}}$

$OM = [(r_3 - r_1)^2 + (r_4 - r_2)^2]^{1/2}$ are carried out. To demonstrate the practical nature of the proposition, an experimental model based on the simplified approach has been constructed, Fig. 4. A synchronous motor with 1 rpm located at O and controlled by a timer is used together with light aluminium arms. The pen attached to the generating-point (C) draws desirable curves with insignificant, unnoticeable errors always remaining inside the thickness of the line. By the presence of a mechanical drive, 4-bar, a motor is saved from the second manipulator. Hence, the assembly is suitably termed as analog robot. Two illustrations are shown in Fig. 5, in which straight lines between points having co-ordinates (10, 30) and (24.5, 18) in the first one and between (10, 24) and (24, 28.5) co-ordinates in the second one are traced. Relevant adjustable parameters (x_1, x_2, x_3, x_6) turn out to be (8.5161, 29.9633, 16.0945, 35.0000) in the first design and (33.1220, 11.3563, 14.9201, 35.0000) in the second one.

Conclusively, all numerical results and experimental work indicate that methods of design for a parallel robotic assembly work very well, leading to optimum results.

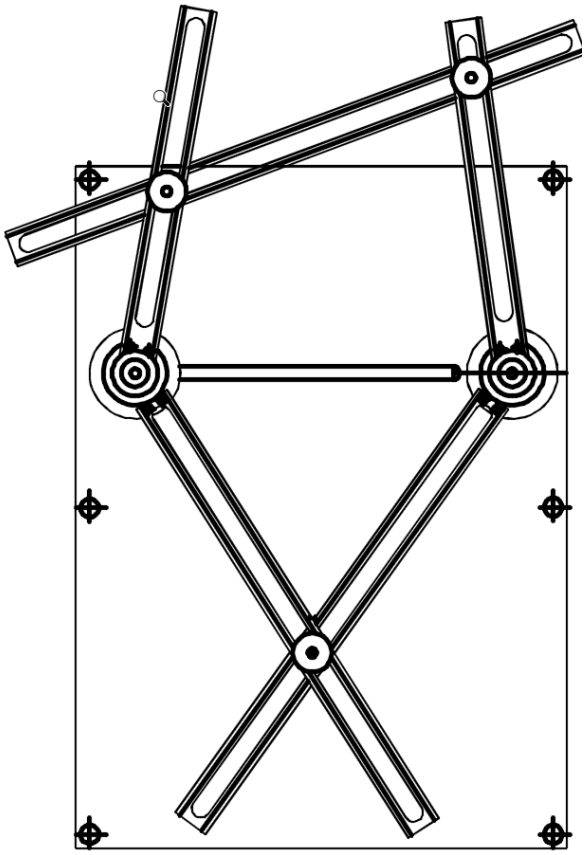

Fig. 4. Experimental model

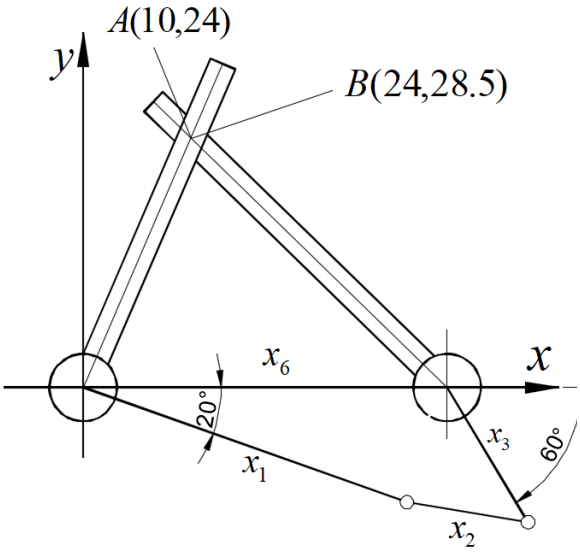

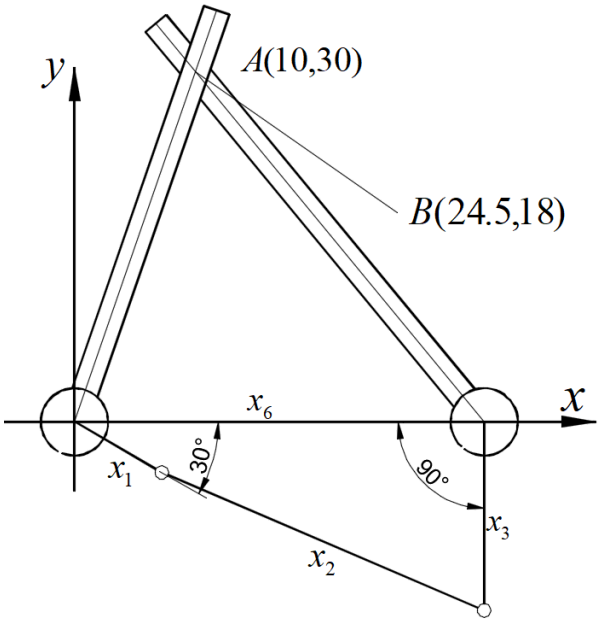

Fig. 5. Two illustrations

REFERENCES

Akçalı, İ. D. and Dittrich, G. (1989a) "Path Generation by Subdomain Method", *Mech. Mach. Theory*, Vol. 24, No.1, pp.45-52,

Akçali, İ. D. and Dittrich, G. (1989b) "Function Generation by Galerkin's Method" M*ech. mach. theory*, Vol. 24, No.1, pp. 39-43

Akçalı, İ. D. (1987) "Design of Slider-Crank Mechanism for Function Generation" *Proc. 7 World Congress on Theory of Machines and Mechanism*, Sevilla, pp. 119-124.

Bernier, D., Castelian, V. and Li, X. (1995) "A New Parallel Structure with 6 Degrees of Freedom" *9 World Congress on the Theory of Machines and Mechanisms, Proc.* Milano, pp. 8-12.

Duffy, J. (1996) *Statics and Kinematics with Applications to Robotics*, Cambridge University Press, UK.

Fu, K. S., Gonzales, R.C. and Lee, C. S. G. (1987) *Robotics, Control*, Sensing, *Vision and Intelligence*, McGraw-Hill Book Co., USA.

Hartenberg, R. S. and Denavit, J. (1964) *Kinematic Synthesis of Linkages*, McGraw-Hill Book Co, USA.

Harris, D. M. J. (1965). "Parallel-Linkage Robot Coordinate Transformation through Screw Theory" *9th World Congress on the theory of Machines and Mechanisms*, Milano, pp. 1565-1568.

Groover, M. P., Weiss, Nagel, R. N. and Odrey, N. G. (1986). *Industrial Robotics Technology Programming and Applications*, McGraw-Hill, Singapore.

Koren, Y. (1987) *Robotics for Engineers*, McGraw-Hill, Singapore.

Liu, A. (1995) "Configuration Analysis of a Class of Parallel Structures Using Improved Continuation", *9th World Congress on the Theory of Machines and Mechanisms*, Milano, pp. 155-158.

Innocenti, C. and Parenti-Castelli, V. (1990). "Direct Position Analysis of the Stewart Platform Mechanism" *Mech. Mach. Theory*, Vol. 25, No. 6, pp. 611- 621.

Stadler, W. (1995). *Analytical Robotics and Mechatronics*, McGraw-Hill Inc., Usa.

Raven, (1987). *Automatic Control Engineering*, 4th Ed., Mc Graw-Hill Book Co., Usa.

Turkish Journal of Engineering

Turkish Journal of Engineering (TUJE)
Vol. 2, Issue 2, pp. 88-93, May 2018
ISSN 2587-1366, Turkey
DOI: 10.31127/tuje.329295
Research Article

STUDY OF THE OSCILLATING WATER COLOUMN (OWC) WHICH IS ONE OF THE MOST USED SYSTEMS IN CONVERTING WAVE ENERGY INTO ELECTRICAL ENERGY

Abdi Kükner *[1]

[1] Istanbul Technical University, Faculty of Naval Architecture and Ocean Engineering, İstanbul, Turkey
ORCID ID 0000-0002-3746-4445
kukner@itu.edu.tr

* Corresponding Author
Received: 18/07/2017 Accepted: 20/12/2017

ABSTRACT
The Oscillating Water Column (OWC) system converting wave energy to electrical power have been investigated. The theoretical analysis of the power generated by the wave energy system is presented. The system is considered as two-dimensional, linear boundary value problem. The system is simulated for the Marmara Sea where the significant wave height is 3.3 meters and the significant wave period is 7 seconds. Results of the theoretical analysis of the wave energy conversion system for Marmara Sea is presented.

Keywords: *Oscillating Water Column, Wave Energy, Wave Energy Conversion, Water Wave Generator, Marmara Sea, Wave Period*

1. INTRODUCTION

Nowadays electrical energy is one of the most required and not dispensed with a basic energy which is necessary to do routine works in our life. Unfortunately, during the conversion of most energies into the electrical power poisoned gases have been produced and other ecological damages have been occurred. These problems have been waiting for the scientists to be solved. Therefore, it is important to think about clean and economical conversation systems which do not damage the nature. Outgoing from this point, we are able to say that wave energy is one of the cleanest, renewable and unbounded energy source to convert into the electrical power. Hence it must be thought about wave energy as one of the alternative energy for the future.

Given the massive energy resources carried in the waves of Oceans, breakthroughs in marine energy technology are expected to enable this energy source to become a major renewable energy supply in the long term. With many contending marine energy devices under development in many countries, the race to prove the fundamental technology type is on. Meanwhile, assessment and mapping of wave energy resources is also underway in many countries to identify sites for deployment of the successful products.

There are a variety of different concepts for wave energy conversion. The devices are generally categorized by the method used to capture the energy of the waves, but can also be categorized by location and by the power take-off system. Method types are point absorber or buoy, surfacing following or attenuator oriented parallel to the direction of wave propagation, oscillating water column, oscillating wave surge converter, terminator (or possibly the new unestablished term quasi point absorber) oriented perpendicular to the direction of wave propagation, overtopping, submerged pressure differential.

Oscillating water column (OWC) systems are one of the most popular technologies for wave energy conversion (Şentürk and Özdamar, 2012; Zhang *et al*., 2012; Heath, 2012). OWC generates energy from the rise and fall of water caused by waves in the ocean. This system uses a large volume of moving water as a piston in a cylinder. Air is forced out of the column as a wave rises and fresh air is drawn in as the wave falls. This movement of air forcing the air upwards through the air turbine. This pressure forces the turbine to spin, which is how the energy is harnessed by the waves. As the waves retreat, air enters back into the air chamber from the other side of the turbine. Several prototype scale OWCs have been constructed and operated with varying degrees of success over the last two decades. There are examples of shoreline, near-shore and breakwater devices in a number of countries.

Converting the energy from ocean waves into useable energy forms is not a new concept as the first related patent was filed in 1799 by Girard and Son and the first operating system, an oscillating water column (OWC), supplied a house with 1 kW in 1910 (Clement *et al.*, 2002; Morris-Thomas, 2007). However, the first serious studies into wave energy took place after the oil crisis in the 1970s and early1980s, where it started being considered as a possible source of power supply (Salter, 1974). Since then, the development of wave energy has gone through a cyclic process of phases of enthusiasm, disappointment and reconsideration. Although budgets have been cut and increased at various occasions, the research and development has persisted, resulting in a constant gain in experience and improved performance, which has brought commercial exploitation of wave energy closer than ever before (Clement *et al*., 2002). Early theories for wave-energy devices related to the rigid-body models had been investigated by Evans (1976), Mei (1976), Newman (1976) and Budal and Falnes (1977). They provided useful and interesting theoretical results for such problems, both in two and three dimensions. An application of the rigid-body theory to a simple OWC model was provided by Evans (1978) and McCormick (1974) Despite the great variety of wave energy converters proposed since the pioneering works of Masuda, McCormick, Budal and Falnes and others, only very few devices have been deployed in real seas.

It is worth noting that, in most of the studies carried out so far, OWC converter can be considered into two parts. These are namely as the air turbine and the column that are investigated separately. In spite of the fact that the coupling between both plays a fundamental role in the performance of the system (Curran *et al*., 1997). In effect, the turbine should ideally provide the pneumatic damping (pressure drop through the turbine) for the chamber to work at, or near, resonant conditions, and the chamber, in turn, should provide the amount of pneumatic power that maximizes the turbine output.

2. ANALYSIS OF THE SYSTEM

It is well known that the wave energy for a unit wide is given by:

$$E = \frac{1}{2}\rho g \zeta_a \lambda$$

where g is gravitational acceleration (m/sec^2), ρ is the density of water (kg/m^3), ζ_a is the half of the wave height (m) and λ is the wave length in meter.

In this study, our aim is to convert this wave energy as much as possible into the electrical energy. Naturally, there will be some energy lost during conversion because of the transportation, storing and friction. In order to keep this lost as low as possible, different kind of devices and theories related with these systems have been developed. One of these is the oscillating water column (OWC) system which is shown in Fig. 1. Theoretical analysis of the system has been studied by many scientists and researchers such as McCormick (1974). It is possible to determine this system by the linear theory, which is solutions are nearly to the nature.

The following given theoretical analysis for the wave energy conversion buoy consists of a circular floatation body which contains a vertical center column that has free communication with the sea. Hence, the water surface in the center of the column rises and falls with the same period as that of the external wave.

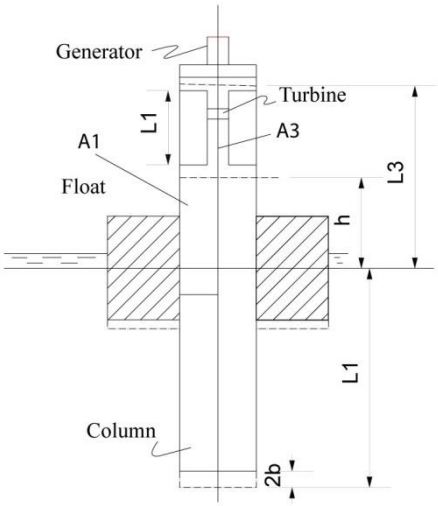

Fig. 1. Oscillating Water Column (OWC)

As is shown in Fig. 1., there is a circular ring around the column which keeps the system on the free surface. When the system moves up and down the air inside the column is compressed or decompressed by the motion of the wave. During the compression or decompression of the air it rotates the turbine propellers which are located on the top of the vertical column. Rotating direction of the propellers will be the same in either compression or decompression case. The air turbine, in turn, drives an electrical generator that produces an energy to be used directly or storage in collecting systems.

In this study, the linear theory presented by Mc Cormick (1974) was used to design a water wave generator for the Marmara Sea. Simulating wave energy for the Marmara Sea, the specific data is needed. It gives us the certain limits and the energy in Joule which was obtained from the paper given by Atkins (1996). By applying the unsteady energy equation between the internal free surface and the exhaust one obtains:

$$\frac{P_1}{\gamma_a}+\frac{\bar{V}_1^2}{2g}=\frac{\bar{V}_3^2}{2g}+\sum h_i+\frac{1}{g}\int_{\xi_1}^{\xi_3}\frac{\partial \bar{V}}{\partial t}\delta\xi+\frac{dW}{dw_a} \quad (1)$$

In this equation, the subscripts 1 and 3 show positions. Position 1 is the internal part of the column right over the water. Position 3 stands for the exhaust on the top of the column. Where P is pressure (kg/m^2), V is velocity (m/s), h is height (m), γ_a is specific weight of air (kg/m^3), t is time given in seconds, ξ is curvilinear coordinate system, W is energy (Joule), w_a is weight of air (kg).

After making some assumptions, details are shown in references (McCormick, 1974) and Bak (1999), one obtains the chamber pressureP_1 in the following form:

$$P_1=-\rho_w(L_1+\zeta)\frac{d^2\zeta}{dt^2} \quad (2)$$

where L_1 stands for the part of the column inside the water (m). ζ means the height of the water from its equilibrium position (m) and ρ_w mass density of the water (kg/m^3). Because of the specific geometry of the system, the added mass excited by the heaving circular floatation body can be written as

$$m_w=C\rho_w\pi(R-r_1)^3 \quad (3)$$

In which C stands for the added mass coefficient. R is the radius of the floatation and r_1 is the radius of the column. The natural circular frequency of the system is obtained by the following equation

$$w_N=\sqrt{\frac{c}{m+m_w-\rho_w\pi r_1^2 L_1}} \quad (4)$$

where c represents the hydrostatic restoring force (kg/s^2), which is given by

$$c=\rho_w g\pi(R^2-r_1^2) \quad (5)$$

Finally using this equation in order to get energy expression and take its derivative by time, the unit power for a second (known as Watt) is obtained. Thus, the final equation is found as

$$\frac{dW}{dt}=\rho_a\zeta\pi r_1^2 g\frac{dW}{dw_a}$$

$$=\rho_a\zeta\pi r_1^2 g\left\{\frac{P_1}{\gamma_a}-\left(\frac{1}{2g}\right)\left[\left(\frac{A_1}{A_3}\right)^2-1\right]\zeta^2-\sum_i\delta_i\frac{d\zeta}{dt}\left|\frac{d\zeta}{dt}\right|\left[-\frac{1}{g}\right]\left[h+L_t\frac{A_1}{A_3}-\zeta\right]\frac{d^2\zeta}{dt^2}\right\} \quad (6)$$

where, A means the area (m^2), δ_i is the damping coefficient (s^2/kg), ρ_a is mass density of air (kg/m^3), L_t and h are lengths (m) as shown in Fig.1.

3. APPLICATION OF THE OSCILLATING WATER COLUMN SYSTEM TO THE MARMARA SEA

For the Marmara Sea, the significant wave height ($H_{1/3}$) can be taken as 3.3 meters and the significant wave period (Ts) as 7.0 seconds (Atkins, 1996). The following results are obtained by using these values and the water mass density of 1025 kg/m^3 for a system having the mass m=1200 kg and the added mass m_w=975 kg (taken from experimental result of buoy used by Masuda (1971). It should be noted that the added mass and the mass of a system depend on the size and the materials used on a system. The power variation as a function of wave period for a wave height at H=3.3 m is shown in Fig. 2.

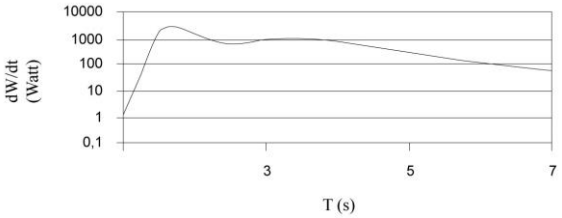

Fig. 2. Power variation as function of the wave period at a wave height H=3.3 m

As can be seen from Fig. 2, the maximum power appears at the wave period T=1.7 seconds. The most effective length of the underwater column is obtained by using this wave period. The result is shown in Fig. 3.

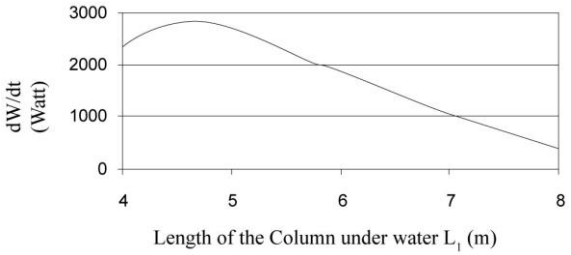

Fig. 3. Power variation of the underwater column-length at a wave period T=1.7 second

This graph can be put into a normalized peak average power variation curve by dividing power with the maximum value of the power variation for the underwater column-length at wave period T=1.7 seconds. The normalized power variation is shown inFig.4.

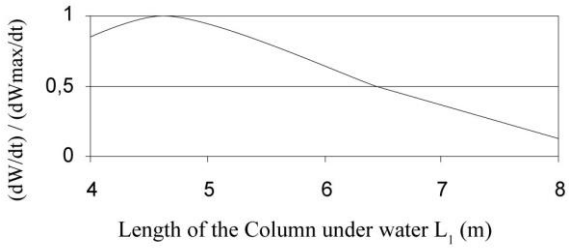

Fig. 4. Normalized average power variation underwater column length

The ideal under water column-length, L_1, can be found from Fig. 3 and Fig. 4 as 4.572 meters. The values of chamber Pressure (P), power (dW/dT), and amplitude at a wave period T=7.0 seconds are obtained by using L_1=4.572 m for the Marmara Sea. The results are presented in Fig.5.

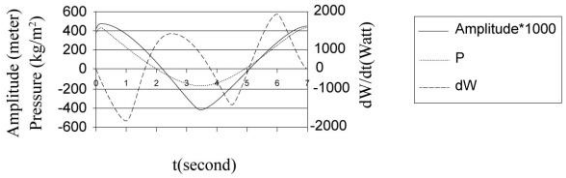

Fig. 5. Power, Pressure and Amplitude variations at a wave period of T=7.0 seconds for a system with water column-length of L_1=4.572 m

The radius of the float, which keeps the system above the water surface, is not necessarily needed for the computations. Therefore, it could be kept as it is. On the other hand, the variation of the radius of the column will change the volume of the internal water and will affect the results. In order to see the result of this, one can assume the radius of the float as R=1 m and change the radius of the column as r=0.1 m, r=0.2 m and r=0.3 m respectively (if r is assumed to be as $r \geq 0.3$, then some of our assumptions cause a non-imaginary result. This makes some troubles for the explanation of the results). When this operation is performed, the following results is obtained.

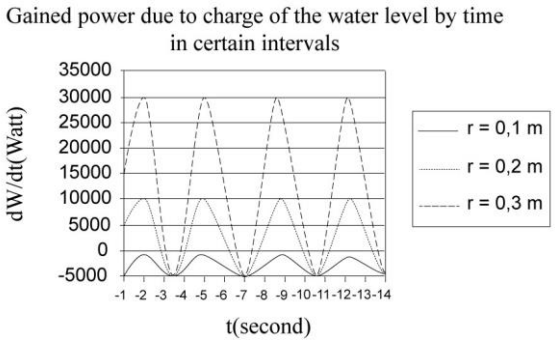

Fig. 6. Power change due to change of the radius of the column

As mentioned before, the wave period for the Marmara Sea is 7 seconds. In Fig. 6, the time interval is taken as 14 seconds in order to cover two wave periods and show that the power changes are periodic. This figure shows that the maximum value of power is produced when the wave is at the top and the lower position of the inside column. In case of the equilibrium wave condition, the system does produce any power. Another important point is that the value of the power increases at the highest value of column radius. This means, the volume of the internal column is directly proportional to the radius of the column. If this approach is correct, the length of the column must also directly proportional to the radius of the column and to the volume of the water inside the column since a longer system would cause a greater amount of water to keep in. In order to see this difference, it has to be used a certain time, in which one gets the maximum power, for example t=5 seconds, that is shown in Fig. 7.

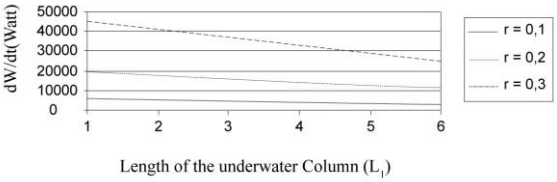

Fig. 7. Power variation at different column radii with changing the underwater column length L_1

As can be seen in Fig. 7, the power decreases with increasing the underwater column length (L_1). There is only one explanation for this result that is: in a deep water, the velocity of the water particles is assumed to be zero at the depth of the half water length and are maximum on the water surface. This means the length of the column under water (L_1) is of second order, this would be contrary to our work, since we work with the linearized equations. This occurs when the underwater column length is very short. Unfortunately, this length cannot be made zero, because of the stabilization of our system.

Keeping the underwater column-length (L_1) very short, could cause the system to flip over. At the same time makes the systems-life very short since the turbine contacts to the salty water during oscillating of the column. The most advantage of our system is that keeps the turbine and the generator out of the salty water which is highly corrosive for every kind of metal. On the other hand, if we talk about a systems-life, we can also

talk about different building materials, which would mean the change of mass and the added mass of our system. The power variation according to changing in underwater column length for the radius of r=0.3 m, having different mass and added mass, is given in Fig. 7. It would be sufficiently enough, if the proportion of the original system between the mass and the added mass is kept constant.

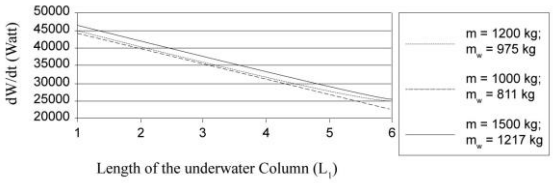

Fig. 8. Power variation by changing the underwater column length (L_1) for the radius r=0.3 m with different mass and added mass system.

As shown in Fig. 8, the power varies with the systems mass and added mass. This means, we have to use high density column materials and should be cheaper. The concrete will be a suitable material for selection.

Until now, we only have looked at the variation of the underwater column-length. But what is going to happen if we change the duct-length or the column-length over water?

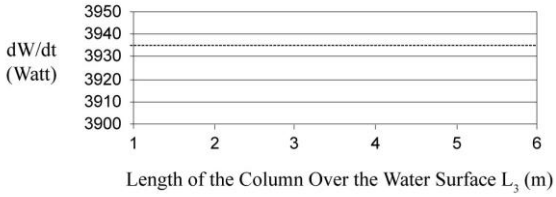

Fig. 9. Power variation while changing the column length over water

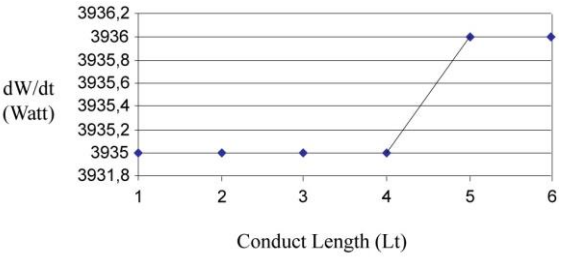

Fig. 10. Power variation while changing the conduct length

From Fig. 9 and Fig. 10, it can be seen that the power will not be affected by the variation of the column-length over water and the conduct-length. Hence it can be said that this parameter will be of second order. There are many waves higher than H=7 meters in Marmara Sea since the significant wave height $H_{1/3}$ is 3.3 meter. Thus, the system must have column-length over water at least L=3-3.5 meters for the Marmara Sea. As a result, the selection of the conduct-length will depend on size of the underwater column length and higher waves, and on the type of the turbine to be used.

4. CONCLUSIONS

As a result of this study the following conclusions can be drawn.

1. The most effective area of the system is when the systems resonance period is the nearest to the wave period of the place (see eq.(4)) For the Marmara Sea this value approximately will be $\omega \cong 0.897$ rad/s for the underwater column length L_1=4.572 m.

2. The optimum oscillating water column design is when the mass of the internal water in the column is 2/3 of the sum of the mass and added mass of the system. This statement has to be considered in the assumption of the linear theory to get more optimum design.

3. The power for the Marmara Sea, produced by the system is directly proportional to the third power of the wave height and can be seen in Fig. 2, 3, 4, 5 and 6.

4. The produced energy will increase by increasing the radius of the column (in certain limits).

5. The short the column-length under water, the much power will be produced. But here, it should be noted that the column-length under water must have a certain size, in order to manage its work for the stability of the system.

6. As the power produced with this system will increase, by increasing the mass of the system, it is necessary to use cheap and high mass density materials such as concrete can be recommended.

Generally speaking, OWC devices present two main advantages over other wave energy converters. First, their simplicity; they consist exclusively of the two aforementioned elements, the chamber and the air turbine. Second, their low maintenance cost relative to other wave energy converters, which are a result of both their simplicity and the absence of mechanical elements in direct contact with seawater.

If OWCs are to have a long-term future, rate of progress must be improved. For future work well-considered proposals for reducing cost/improving performance were to be made and justified. Estimates of cost of-energy benefits. Economic models were established for shoreline and near shore devices to investigate the likely p/kWh power output cost, and to test the sensitivity of this cost to the main design elements of an OWC development. Improvements with the biggest impact on the power production cost, requiring the least effort to implement, were then identified.

Attention was then focused on the improvements of OWC system that might be made on near-shore devices by incorporating the lessons learnt from previous projects and by assessing, through analysis and related experience, the effectiveness of a range of improvements in design, fabrication and installation of OWCs. Such improvements would reap greater reward in view of the larger near-shore resource that can be realized. The key elements of improved economics are reduced structural quantities and survival loading combined with the maximum possible wave energy capture.

The basic working principle of wave energy concepts have gone in all directions with no significant

convergence that has been identified yet. Many concepts have been tank tested, but only few managed to undertake sea trials. This is the result from the various types of difficulties involved in making wave energy converters cost-effective.

REFERENCES

Atkins, W. S. (1996). "*Assessment of Design Environmental Data,* TPAO, Ankara, Türkiye.

Bak U. (1999). Dalga Enerjisinden Elektrik Enerjisi Elde Edilmesi, Bitirme Çalışması (Graduation Project), İ.T.Ü.

Budal, K. and Falnes, J. (1977). "Optimum operation of improved wave-power converters." *Marine Sciences Comm*. No.3, pp 133-150.

Clement, A., McCullen, P., Falcão, A., Fiorentino, A., Gardner, F., Hammarlund, K., Lemonis, G., Lewis, T., Nielsen, K., Petroncini, S., Pontes, M. T., Schild Phillipe, B,-O. Sjöström, O., Sørensen, H. C. and Thorpe, T. (2002). "Wave energy in Europe: current status and perspectives." *Renewable and Sustainable Energy Reviews*, Vol. 6, pp. 405–431.

Curran, R., T. Stewart and Whittaker, T. J. T. (1997). "Design synthesis of oscillating water column wave energy converters: performance matching." *Proceedings of the Institution of Mechanical Engineers - Part A: Journal of Power and Energy*, No.211, pp. 489–505.

Evans, D. V. (1976). "A theory for wave power absorption by oscillating bodies." *J. Fluid Mech.*, No. 77, pp. 1-25.

Evans, D.V. (1978). "The Oscillating Water Column wave energy device." *J. Inst. Maths Applics.*, No.22, pp. 423-33.

Masuda, Y. (1971). "Wave Activated Generators." Paper presented at the International Collocium on the Exposition of the Oceans, Bordo, France.

McCormick, M. E. (1974). "Analysis of a Wave Energy Conversion Buoy." *Journal of Hydronautics*, No.8 (3), pp. 77-82.

McCormick, M. E. (1976) "A modified linear analysis of a wave-energy conversion buoy." *Ocean Engineering*, No.3, pp.133–144.

Mei, C. C. (1976). "Power extraction from water waves." *J. Ship Research*, Vol. 20, pp. 63-66.

Morris-Thomas, M. T., Irvin, R. J. and Thiagarajan, K. P. (2007). "An Investigation into the Hydrodynamic Efficiency of an Oscillating Water Column." *Journal of Offshore Mechanics and Arctic Engineering*, Vol. 129, No. 4, pp. 273.

Newman, J. N. (1976). "The interaction of stationary vessels with regular waves." *Proc. 11th Symposium Naval Hydrodynamics*, pp. 451-501.

Salter, S. H. (1974). "Wave Power." *Nature*, Vol. 249, No. 5459, pp. 720–724.

Şentürk, U. and Özdamar, A. (2012). "Wave energy extraction by an oscillating water column with a gap on the fully submerged front wall." *Applied Ocean Research*, No.37, pp. 174–182.

TV Heath, T., V. (2012). "A review of oscillating water columns." *Philosophical Transactions of the Royal Society A: Mathematical Physical and Engineering*, No. 370, pp. 235–245.

Zhang, Y., Zou, Q. and Greaves, D. (2012). "Air-water two-phase flow modelling of hydrodynamic performance of an oscillating water column device." *Renewable Energy*, No.41, pp. 159–170.

CONTENTS

ISSN 2587-1366

TURKISH JOURNAL OF ENGINEERING

VOLUME 2 ISSUE 2 MAY 2018